Article 7 *Ann. Glaciol.*, **28**, 1-8, 1999

Deglaciation of the Northern Hemisphere at the onset of the Eemian and Holocene

Ralf Greve[†], Karl-Heinz Wyrwoll[‡] and Anton Eisenhauer[♯]

[†]Institut für Mechanik, Technische Universität Darmstadt, D-64289 Darmstadt, Germany

[‡]Department of Geography, The University of Western Australia, Nedlands, Perth, WA 6907, Australia

[♯]Geochemisches Institut, Universität Göttingen, D-37077 Göttingen, Germany

Abstract

High resolution (TIMS) U-series dating of sea level events obtained from coral reef complexes has suggested that the global deglaciation from the Saale (penultimate) glacial to the Eem interglacial (marine δ^{18}O stages 6/5) may have occured earlier in relation to Milankovitch insolation forcing than that from the Wisconsin glacial to the Holocene interglacial (marine δ^{18}O stages 2/1). However, the interpretation of these data have been problematic because of the possibility of isotope exchange. In order to investigate whether these different lead/lag relations between Milankovitch forcing and ice volume are feasible from the point of view of large-scale ice-sheet dynamics and thermodynamics, the 3-d polythermal ice-sheet model SICOPOLIS is applied to the entire northern hemisphere (which gives the major contribution to global ice volume changes due to the relative stability of the Antarctic ice sheet), and simulations through the two last climatic cycles are conducted. The simulations cover the time interval from 250 ka BP until today and are driven by surface-temperature reconstructions of deep ice cores (GRIP, Vostok) and simple parameterizations for the change of precipitation with time. Discussion of the results is focussed on the Saale/Eem and the Wisconsin/Holocene transitions. The amount and rate of deglaciation are in good agreement with the SPECMAP record for both cases, and the data evidence for an early start of the Eem interglacial is supported.

1 Introduction

This paper addresses the question of whether there is a significant difference in the deglaciation histories during Termination II (marine δ^{18}O stages 6/5, in the following simply referred to as "stages") and Termination I (stages 2/1). Deglaciation and the associated ocean volume changes of Termination I can be easily and accurately dated

by standard radiometric techniques. With the development of thermal ionisation mass spectrometric uranium series (TIMS U-series) dating (Edwards et al., 1987a) the prospect of establishing the timing of the Eem interglacial (substage 5e) events with errors of as little as ±2-3 ka (at the 2σ level) was encouraging. However, after a brief period of confidence in both the resolution and accuracy of this dating technique, it has become apparent that the reliability of TIMS U-series dating results is open to doubt because of problems of diagenesis and associated isotope exchange processes commonly undergone by corals of Eem interglacial age (Hamelin et al., 1991; Henderson et al., 1993). Consequently, the suggestion that significant differences exist in the lead-lag relationships between Milankovitch insolation forcing and sea level response between stages 6/5 and 2/1 (Chen et al., 1991; Zhu et al., 1993), can no longer be proposed with confidence. Therefore, we attempt to resolve the issue of a possible early sea level high during substage 5e from a totally different and independent perspective, namely by placing it into the context of ice-sheet modelling. In this we use the SICOPOLIS model (Greve, 1995, 1997b) to establish whether the claim of differences in the ice response to insolation between Terminations I and II can be independently reproduced through dynamic/thermodynamic ice-sheet modelling.

2 Eem interglacial sea level events – the wider context of the problem

The possible existence of a high sea level stand during the early part of the Eem interglacial (substage 5e) has been a long-standing issue (Bloom et al., 1974; Kaufman, 1986). The importance of this question lies in the fact that an early sea level high at that time may question the traditional role ascribed to Milankovitch insolation variations as the direct driving force of glacial/interglacial transitions. More recently, results from a number of TIMS U-series-dated corals became available which suggested that during the Eem interglacial, sea level was close to its present height by at least as early as 132000 years ago (Chen et al., 1991; Zhu et al., 1993; Szabo et al., 1994). However, problems of diagenesis and associated isotope exchange may invalidate some of the dates obtained. (Henderson et al., 1993; Stirling et al., 1995). The discussion of an early sea level gains further support by the Devil's Hole isotope record (Winograd et al., 1992; Edwards et al., 1997) which also suggests an early onset of interglacial climate during substage 5e.

The analytical procedures for U and Th separation, TIMS isotopic measurements and age calculations are now standard and well established (Edwards et al., 1987b; Chen et al., 1991). First, samples are screened for indications of recrystallization/exchange. A check on the validity of the dates obtained is given by a comparison

of the calculated initial $^{234}U/^{238}U$ ratio of the samples dated with the known isotopic composition of seawater [for details of different requirements/interpretations see Chen et al. (1991), Zhu et al. (1993), Gallup et al. (1994), Szabo et al. (1994) and Stirling et al. (1995)]. This check is a necessary prerequisite for the evaluation of dates, but it is not sufficient to demonstrate their accuracy. The problems have been brought into focus through the use of TIMS ^{231}Pa dating of carbonates (Edwards et al., 1997). The application of this technique has the potential to provide an independent test on the claims of an early sea level high during substage 5e, by making it possible (in conjuction with Th dating) to obtain both primary and diagenetic ages as well as constraints on the nature of the diagenetic processes (Edwards et al., 1997).

A general limitation of most Eem interglacial coral reef studies is that the samples dated have been obtained from scattered outcrop. Usually what has been dated is the 'peak' (and its persistence) of the Eem interglacial sea level high. Consequently, the dates cannot be placed within a firm stratigraphic context, which would provide an additional check of their validity. In our work we have obtained stratigraphically-secured TIMS U-series dates (for the details see Eisenhauer et al., 1996) which not only allow us to date the sea level 'peak' but also the events leading up to it. The dates come from the upper part of a core obtained from the Houtman Abrolhos reef complex, which is a series of shelf edge coral reefs located some 70 km off the coast of the central western margin of Australia. The samples which were dated were screened for diagenetic changes using methods and selection criteria developed in an earlier stage of the project (Zhu et al., 1993). Because of their stratigraphic context we have sufficient confidence in the results to consider it worthwhile to explore the possibility whether our claims could be independently tested through ice-sheet modelling.

The sea-level scenario which results from the TIMS U-series dates (Fig. 1) shows a sea level close to its present height by circa 130 ka BP (calendar years before present) – much earlier than the commonly claimed date of 124 ka BP. If these results are valid they imply that the insolation-sea level lead/lag relationship of stages 6 to 5 (Termination II) was fundamentally different from that associated with the glacial/interglacial switch of stages 2 to 1 (Termination I). During Termination I insolation levels at 65°N (traditionally taken to be the "forcing" latitude) peaked as early as 11000 years ago, while sea levels at the western margin of Australia did not peak until circa 6500 years ago (Eisenhauer et al., 1993; Wyrwoll et al., 1995). If during Termination II sea level in the western Australian region was already close to its present height by circa 130000 years ago, this would have occurred some 2000 years before the occurrence of the 65°N insolation maximum. If correct, such a conclusion would open the question as to how Milankovitch insolation and ice volumes interactions may have differed between Termination I and II, as well as having implications for the veracity of the SPECMAP chronology (Imbrie et al., 1984).

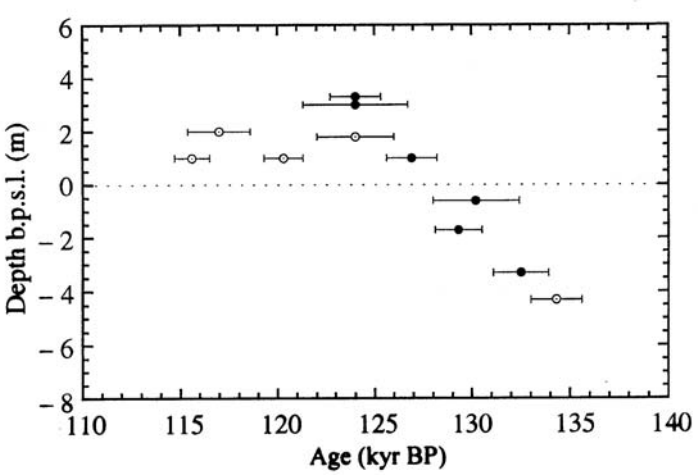

Figure 1: Eem interglacial sea level curve (U-series ages against depth below present sea level, b.p.s.l.) based on the Houtman Abrolhos U-series dates of Zhu et al. (1993) (open circles) and Eisenhauer et al. (1996) (full circles).

3 Ice-sheet model SICOPOLIS

SICOPOLIS is a 3-d dynamic/thermodynamic ice-sheet model based on the continuum-mechanical theory of polythermal ice masses (Fowler and Larson, 1978; Hutter, 1982, 1993; Calov and Hutter, 1997; Greve, 1997a). It simulates the time-dependent extent, thickness, velocity, temperature, water-content and age for grounded ice sheets in response to external forcing. Further, possible basal layers of temperate ice (at the pressure melting point) can be monitored computationally with high vertical resolution by fulfilling the Stefan-type conditions at the cold-temperate-transition surface (this procedure is referred to as the "polythermal mode", where the term polythermal means the simultaneous existence of cold and temperate ice within an ice body). External forcing is specified by (i) mean annual air temperature above the ice, (ii) surface mass balance (accumulation, surface melting), (iii) sea level surrounding the ice sheet and (iv) geothermal heat flux from below. The particular dynamics of possible adjacent ice shelves is not accounted for. The model is discussed in greater detail by Greve (1995, 1997b).

Because of the extremely large RAM space and CPU time requirements of the polythermal mode when applied to a model domain as large as the entire northern hemisphere with reasonably fine horizontal resolution ($\leq 100\,\mathrm{km}$), we switched it off ("cold-ice mode": the Stefan-type conditions at the cold-temperate-transition surface are ignored, computed temperatures above pressure melting are artificially reset to pressure melting instead) in the simulations conducted for this study. Greve (1997b) demonstrates that application of the cold-ice mode instead of the polythermal mode has only a relatively small effect on the large-scale properties of the simulated ice sheet

and also on the *basal area* of temperate ice. The volume and thickness of overlying *layers* of temperate ice cannot be predicted accurately in the cold-ice mode. This loss of fine-structure information is accepted here.

In this study, SICOPOLIS is applied to the entire northern hemisphere prone to extended glaciation, projected to a polar stereographic map with standard parallel at 71°N. The results of transient palaeoclimatic simulations which cover two entire glacial/interglacial cycles are discussed, with focussing on the deglaciation and the associated sea-level rise at the onset of the Eemian and of the Holocene. Horizontal grid spacing is 80 km, which corresponds to 157×157 grid points in the stereographic plane. The distortions due to the projection from the hemisphere to the plane are accounted for in the computations. The vertical resolution is 21 grid points in the ice region and 11 grid points in the lithosphere.

4 Parameterization of the northern hemisphere climate

The model SICOPOLIS requires the mean annual air temperature above the ice, T_{ma}, the snow accumulation, S, and the surface melting, M, as space- and time-dependent boundary conditions. These quantities are fairly well determined for the present; however, for past climate conditions some simplifying assumptions must be made as only sparse information is at hand.

4.1 Present conditions

The present topography of the bedrock is constructed based on the ETOPO5 (1988) land and sea-floor elevations, which are gridded with a resolution of 5' in latitude and longitude. In the area of the present Greenland ice sheet where this data set gives the ice surface instead of the bedrock, the bedrock data of Letréguilly et al. (1991a) with 20 km resolution in the stereographic plane are applied.

For the present distribution of the surface air temperature, ECMWF (European Centre for Medium-Range Weather Forecast) data of the years 1986-1989 and 1991-1994 are used. These data are available as monthly means for midnight and midday and are averaged to seasonal means, T_{mam} (spring: March, April, May), T_{jja} (summer: June, July, August), T_{son} (autumn: September, October, November) and T_{djf} (winter: December, January, February).

Similarly, the present precipitation is based on mean monthly precipitation data by Jaeger (1976), from which the seasonal means P_{mam}, P_{jja}, P_{son} and P_{djf} are computed. As only solid precipitation contributes to the formation of ice sheets, these mean seasonal precipitations are transformed to mean seasonal snowfall rates, S, by the

empirical relation (Marsiat, 1994)

$$S_{\text{mam}} = P_{\text{mam}} \times \begin{cases} 0, & T_{\text{mam}} \geq 7^\circ\text{C}, \\ (7^\circ\text{C} - T_{\text{mam}})/17^\circ\text{C}, & -10^\circ\text{C} \leq T_{\text{mam}} \leq 7^\circ\text{C}, \\ 1, & T_{\text{mam}} \leq -10^\circ\text{C}, \end{cases} \tag{4.1}$$

and accordingly for S_{jja}, S_{son}, S_{djf}.

Surface melting, M, is parameterized by the degree-day method (Braithwaite and Olesen, 1989; Reeh, 1991), with different degree-day factors for the melting of snow, β_{snow}, and for the melting of ice, β_{ice}. The air temperature is hereby assumed to follow a sinusoidal annual cycle with amplitude $T_{\text{jja}} - T_{\text{ma}}$, and additional variations due to the diurnal cycle and changing weather conditions are treated as normally-distributed statistical variations with standard deviation σ_{stat}. Instead of the conventional purely-numerical evaluation of the integrals for the resulting positive degree days (Reeh, 1991; Huybrechts, 1993), Calov's (pers. comm. 1997) semi-analytical solution is employed, which is more precise and saves a considerable amount of CPU time.

4.2 Past conditions

The surface air temperature of the northern hemisphere at any time in the past can differ from the present one for two reasons: (a) the climate is generally colder or warmer, and (b) the surface elevation has changed. The former is described by a purely time-dependent offset $\Delta T_{\text{air}}(t)$, the latter by a lapse rate γ_{t}:

$$T_{\text{mam}} = T_{\text{mam}}^{\text{present}} \exp\Big(\gamma_{\text{t}} \left(h - h_{\text{ref}}\right)\Big) + \Delta T_{\text{air}}(t); \tag{4.2}$$

correspondingly for T_{jja}, T_{son}, T_{djf}. Hereby, h_{ref} is the reference elevation for the present temperature and precipitation data, which corresponds to the present land and sea surface, respectively.

The past precipitation at the reference elevation h_{ref} is assumed to be linearly coupled to the air-temperature deviation ΔT_{air}:

$$P(h_{\text{ref}}) = P_{\text{present}} \Big(1 + \gamma_{\text{s}}\, \Delta T_{\text{air}}(t)\Big). \tag{4.3}$$

Further, elevation desertification due to the decreasing amount of water vapour in the air is accounted for by prescribing a 50% precipitation reduction per km elevation above $h_0 = 2\,\text{km}$ (Budd and Smith, 1979):

$$P = P(h_{\text{ref}}) \times \begin{cases} \exp\Big(\gamma_{\text{p}} \left[\max(h,\, h_0) - h_0\right]\Big), & h_{\text{ref}} \leq h_0, \\ \exp\Big(\gamma_{\text{p}} \left[\max(h,\, h_0) - h_{\text{ref}}\right]\Big), & h_{\text{ref}} \geq h_0, \end{cases} \tag{4.4}$$

with $\gamma_{\text{p}} = -0.6931\,\text{km}^{-1}$. Again, eqs. (4.3) and (4.4) are evaluated separately for the four seasons, and conversion to the seasonal accumulations, S, is done by eq. (4.1). Also, the parameterization of surface melting is the same as for present conditions.

5 Simulation set-up

Two simulations of transient northern hemisphere glaciation which cover the two last climate cycles have been set up:

Simulation nt012:

- Model time: from $t = -250\,\mathrm{ka}$ (250 ka BP) until $t = 0$ (today).
- Degree-day model: $\beta_{\mathrm{snow}} = 3\,\mathrm{mm\,w.e.} \times (\mathrm{d}\,^\circ\mathrm{C})^{-1}$, $\beta_{\mathrm{ice}} = 12\,\mathrm{mm\,w.e.} \times (\mathrm{d}\,^\circ\mathrm{C})^{-1}$ (w.e.: water equivalent), $\sigma_{\mathrm{stat}} = 5^\circ\mathrm{C}$.
- Geothermal heat flux: $Q^{\perp}_{\mathrm{geoth}} = 55\,\mathrm{mW\,m^{-2}}$.
- Isostatic bedrock adjustment: Local-lithosphere-relaxing-asthenosphere model (Le Meur and Huybrechts, 1996) with asthenospheric time lag $\tau_{\mathrm{V}} = 3000\,\mathrm{a}$.
- Air-temperature forcing: Reconstruction derived from the $\delta^{18}\mathrm{O}$ profile of the central Greenland GRIP core (Dansgaard et al., 1993) and the conversion formula (Johnsen et al., 1995)

$$T^{\mathrm{GRIP}}_{\mathrm{ma}}(t) = \alpha + \beta\,\delta^{18}\mathrm{O}(t) + \gamma\,(\delta^{18}\mathrm{O})^2(t), \tag{5.1}$$

  where $T^{\mathrm{GRIP}}_{\mathrm{ma}}$ is the mean annual air temperature at the GRIP position, and $\alpha = -211.4^\circ\mathrm{C}$, $\beta = -11.88^\circ\mathrm{C} \times ‰^{-1}$, $\gamma = -0.1925^\circ\mathrm{C} \times ‰^{-2}$. From eq. (5.1),

$$\Delta T_{\mathrm{air}}(t) = f_{\mathrm{GRIP}} \times \left(T^{\mathrm{GRIP}}_{\mathrm{ma}}(t) - T^{\mathrm{GRIP}}_{\mathrm{ma}}(0)\right); \tag{5.2}$$

  the factor $f_{\mathrm{GRIP}} = 0.875$ is chosen such that the simulated ice volume at the Last Glacial Maximum (LGM) fits the sea-level (z_{sl}) low derived from the SPECMAP $\delta^{18}\mathrm{O}$ record via $z_{\mathrm{sl}}\,[\mathrm{m}] = -34.83\,(\delta^{18}\mathrm{O}\,[‰] + 1.93)$ (Imbrie et al., 1984).
- Lapse rate: $\gamma_{\mathrm{t}} = -6.5^\circ\mathrm{C\,km^{-1}}$.
- Precipitation-temperature coupling: $\gamma_{\mathrm{s}} = 0.0429^\circ\mathrm{C}^{-1}$, corresponding to a 75% reduction of P for the mean LGM temperature $\Delta T_{\mathrm{air}} = -17.5^\circ\mathrm{C}$ resulting from eq. (5.2).
- Sea level z_{sl}: Computed under the assumption that global sea level is mainly determined by changes of northern hemisphere glaciation. This is justified due to the relative stability of the Antarctic ice sheet through glacial/interglacial cycles (Huybrechts, 1992; Budd et al., 1998). With the sea-level equivalent of the simulated northern hemisphere glaciation, H_{sle}, and its present value, $H^{\mathrm{present}}_{\mathrm{sle}} = 7\,\mathrm{m}$ (Greenland plus small ice caps and glaciers),

$$z_{\mathrm{sl}}(t) = H^{\mathrm{present}}_{\mathrm{sle}} - H_{\mathrm{sle}}(t), \tag{5.3}$$

where $z_{\mathrm{sl}} = 0$ corresponds to the present sea level and positive (negative) values denote higher (lower) stands.

Simulation nt016:

- Air-temperature forcing: Vostok air-temperature history $T_{\mathrm{ma}}^{\mathrm{Vostok}}(t)$ derived from the δD profile of the east Antarctic Vostok core (Jouzel et al., 1993, 1996), then

$$\Delta T_{\mathrm{air}}(t) = f_{\mathrm{Vostok}} \times \left(T_{\mathrm{ma}}^{\mathrm{Vostok}}(t) - T_{\mathrm{ma}}^{\mathrm{Vostok}}(0) \right) . \tag{5.4}$$

  Again, the factor f_{Vostok} serves to provide agreement between simulated LGM ice volume and SPECMAP sea-level low. Because the Vostok signal is much weaker than the GRIP signal and apparently underestimates the northern hemispheric temperature variations, the value $f_{\mathrm{Vostok}} = 2$ is applied here.

- Further settings see simulation nt012.

6 Results and discussion

Fig. 2 depicts the sea-level history resulting from simulations nt012 and nt016 versus the SPECMAP record. When comparing the GRIP-driven simulation nt012 with SPECMAP, we see first a good agreement for the main glacial lows and interglacial highs, which confirms the realistic choice of the factor f_{GRIP} in eq. (5.2). The rates of sea-level rise during Termination II (stages 6/5) and Termination I (stages 2/1) are in good agreement as well (Table 1). However, the simulated deglaciation of Termination II occurs approximately 5000 years earlier than the one of the SPECMAP data, whereas there is an almost perfect coincidence for Termination I. This is further demonstrated by the times at which the respective sea level reaches the close-to-interglacial value $z_{\mathrm{sl}} = -10\,\mathrm{m}$ (Table 2): for Termination II, the times of nt012 and SPECMAP differ by 4400 years, for Termination I only by 200 years. This finding supports the result of our coral reef data, even though the difference for Termination II is somewhat smaller than the $\sim$6000 years according to the data (see section 2).

Deglaciation event	nt012	nt016	SPECMAP
Termination II	$11.3\,\mathrm{m\,ka^{-1}}$	$25.6\,\mathrm{m\,ka^{-1}}$	$11.0\,\mathrm{m\,ka^{-1}}$
Termination I	$11.8\,\mathrm{m\,ka^{-1}}$	$13.4\,\mathrm{m\,ka^{-1}}$	$10.8\,\mathrm{m\,ka^{-1}}$

Table 1: Rates of sea-level rise (interval $z_{\mathrm{sl}} = -110\,\mathrm{m} \ldots -10\,\mathrm{m}$) for the deglaciation events of Termination II and Termination I, respectively. Simulations nt012, nt016 versus SPECMAP record.

Deglaciation event	nt012	nt016	SPECMAP
Termination II	129.1 ka BP	126.8 ka BP	124.7 ka BP
Termination I	5.2 ka BP	4.8 ka BP	5.4 ka BP

Table 2: Time at which the sea level reaches the close-to-interglacial value $z_{\rm sl} = -10$ m during Termination II and Termination I, respectively. Simulations nt012, nt016 versus SPECMAP record.

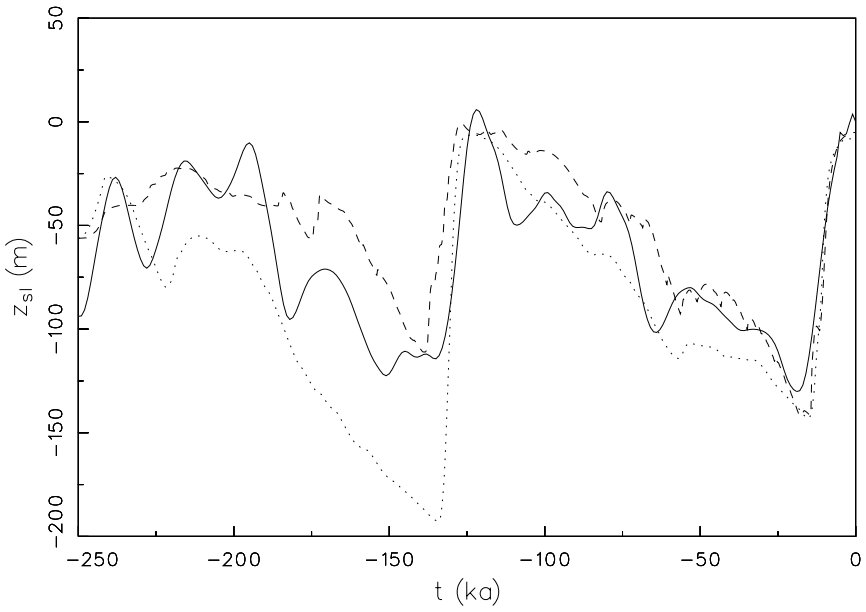

Figure 2: Global sea level $z_{\rm sl}$ resulting from computed (simulations nt012, dashed, and nt016, dotted) changes of northern hemisphere glaciation versus the SPECMAP record converted to sea level via $z_{\rm sl}\,[\mathrm{m}] = -34.83\,(\delta^{18}\mathrm{O}\,[‰] + 1.93)$ (Imbrie et al., 1984; solid).

It is further conspicuous that the simulated and SPECMAP stadials and interstadials fall together rather well for the Wisconsin ice age, whereas there are large discrepancies for the Saale glacial. This may be so because of flow irregularities in the near-bottom ice of central Greenland which affect the stratigraphy of the δ^{18}O record of the GRIP core and/or the breakdown of the δ^{18}O-temperature relation (5.1) so far in the past (Johnsen, 1995; Thorsteinsson, 1996).

The present glaciation of the northern hemisphere, which consists mainly of the Greenland ice sheet, is reproduced well by simulation nt012. The simulated present sea level is 5.1 m lower than the actual one due to some ice remnants in Tibet and the Russian Arctic which do not exist in reality (Fig. 3).

The correspondence between the Vostok-driven simulation nt016 and SPECMAP is generally worse than the one between nt012 and SPECMAP, which is no surprise

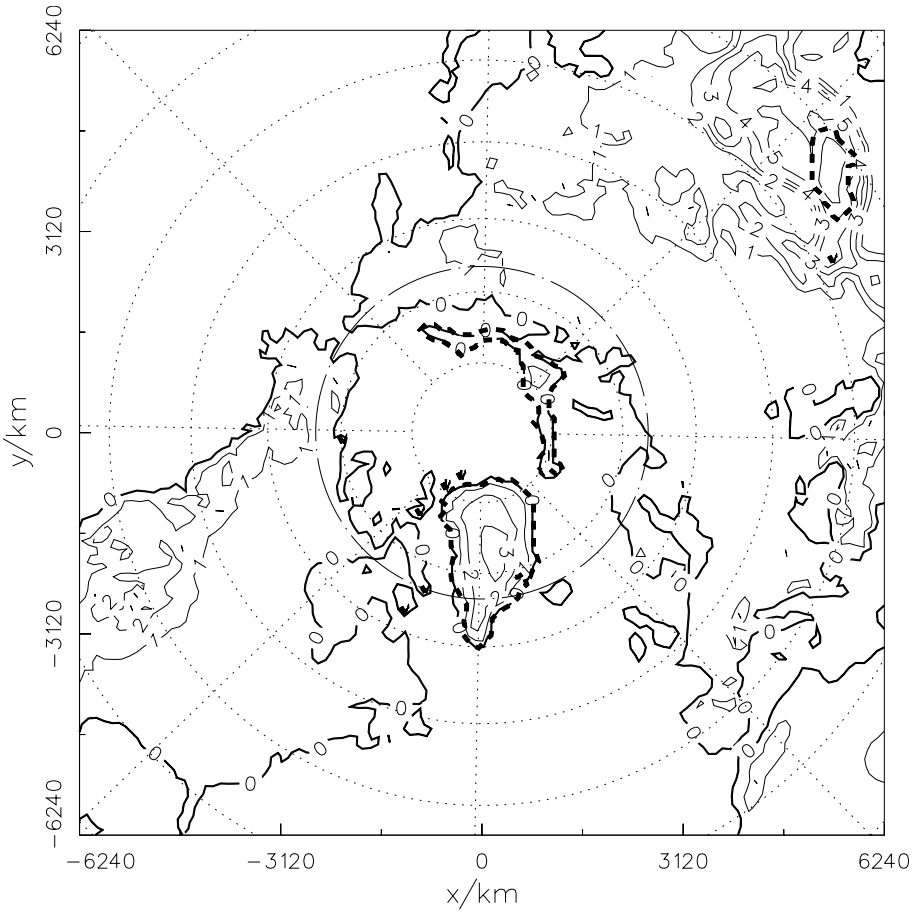

Figure 3: Simulation nt012: Present surface topography, in km above mean present sea level. Contour spacing is 1 km, latitude circles are spaced by 10°. The dashed heavy lines indicate the ice margins.

because an Antarctic record is used to force a simulation of the northern hemisphere. The choice of the factor f_{Vostok} in eq. (5.4) assures good agreement for the LGM sea-level low; this holds also for the Eemian and Holocene highs. However, the simulated sea levels in the course of the Wisconsin and even more pronounced in the course of the Saale glacial are distinctly lower than the SPECMAP sea levels (Fig. 2). Correspondingly, the rate of sea-level rise during Termination II is more than twice the SPECMAP value, whereas it is only moderately larger for Termination I (Table 1).

As for the dating of Terminations I and II, we find essentially the same behaviour as between nt012 and SPECMAP. The close-to-interglacial sea level $z_{\mathrm{sl}} = -10\,\mathrm{m}$ of nt016 is reached 2100 years earlier than the one of the SPECMAP data for Termination II, whereas the difference is much smaller (600 years) for Termination I (Table 2). Evidently, an early sea-level high during substage 5e is also predicted by simulation nt016, even though the finding is less significant than for simulation nt012.

Again, due to some artificial ice remnants in Tibet and the Russian Arctic the simulated present sea level does not entirely reach the real one. The discrepancy

amounts to 8.2 m, somewhat more than for simulation nt012.

Figs. 4 and 5 show for the GRIP-driven simulation nt012 the surface topography for the deglaciations during Terminations II and I, respectively, in 2-ka intervals. Evidently, both deglaciation events proceed very similarly. The initial state consists of a strongly glaciated northern hemisphere with a Laurentide ice sheet reaching down to approximately 45°N and connected to the Greenland ice sheet, a Fennoscandian ice sheet connected to a large Siberian ice sheet, a Tibetean ice sheet between 30°N and 40°N, a glaciated Bering Strait and a Cordillerian ice sheet down to 50°N, with generally slightly more ice at the onset of Termination I. Comparison of the simulated glaciation at 16 ka BP with current reconstructions of the LGM (Denton and Hughes, 1981; Peltier, 1994) shows that the ice covers of east Siberia and the Bering Strait are probably unrealistic, whereas the Laurentide ice sheet is somewhat too small. This is a common problem of ice-sheet models (e.g., Huybrechts and T'siobbel, 1995; Budd et al., 1998) which may be due to topography-induced changes of the atmospheric circulation not accounted for by simple climate parameterizations like Eqs. (4.2)-(4.4). For both deglaciation events, 6000 years after the onset, the Fennoscandian and Cordillerian ice sheets have disappeared completely, whereas the Laurentide, Siberean and Tibetean ice sheets are more stable, and Greenland remains essentially unchanged apart from a slight reduction in area. After 10000 years of deglaciation, only the Greenland ice sheet and the already mentioned ice remnants in the Russian Arctic and Tibet remain, the latter being less pronounced in the very warm Eemian than in the slightly colder Holocene. This timescale for deglaciation following a glacial/interglacial climate switch was already obtained by the simulations of Huybrechts and T'siobbel (1995).

As stated above, the simulation results support an early Eemian sea-level high. If this is indeed true, the traditional idea of a direct cause-and-effect relation between Milankovitch forcing at 65°N and global sea level response must be abandoned. This conclusion has been anticipated by the results of a recent two-dimensional global energy balance model simulation (Crowley, 1994; Crowley and Kim, 1994), for which the 65°N insolation forcing was replaced by a latitude-dependent approach. The model results suggest that, given global insolation values at that time, an early deglaciation during Termination II can be expected. Model output shows that zonally averaged July temperatures over critical northern hemisphere latitudes with ice cover (50-70°N) were about 2.5°C warmer than at present by about 130 ka BP, and warming in the highest latitudes exceeds the present by 1-1.5°C as early as 134 ka BP. It can therefore be argued that an early sea-level high during substage 5e is entirely consistent with Milankovitch forcing provided the meridional variation of the insolation is accounted for.

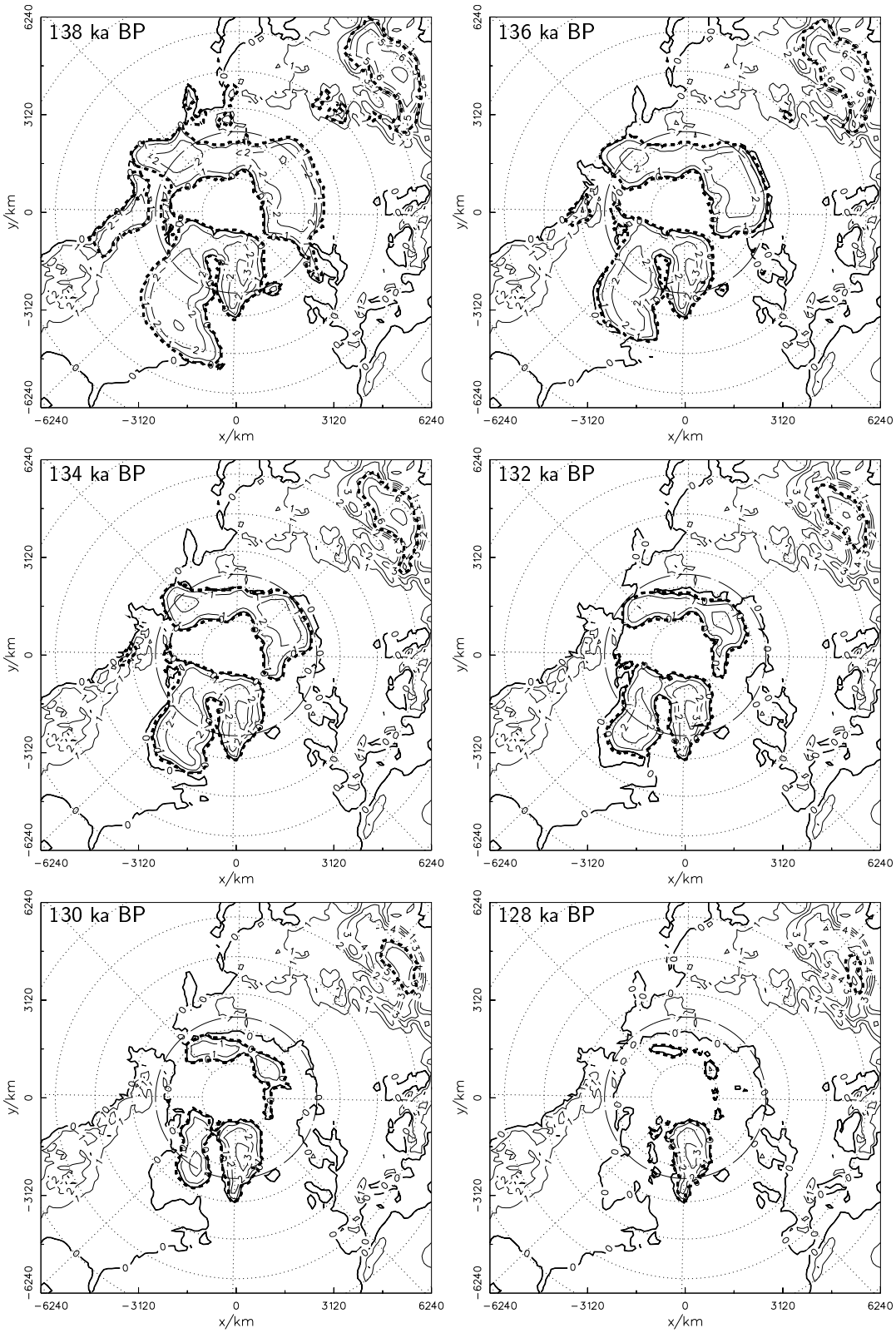

Figure 4: Simulation nt012: Surface topography for the deglaciation during Termination II (t = 138, 136, 134, 132, 130, 128 ka BP), in km above mean present sea level. Contour spacing is 1 km, latitude circles are spaced by 10°. The dashed heavy lines indicate the ice margins.

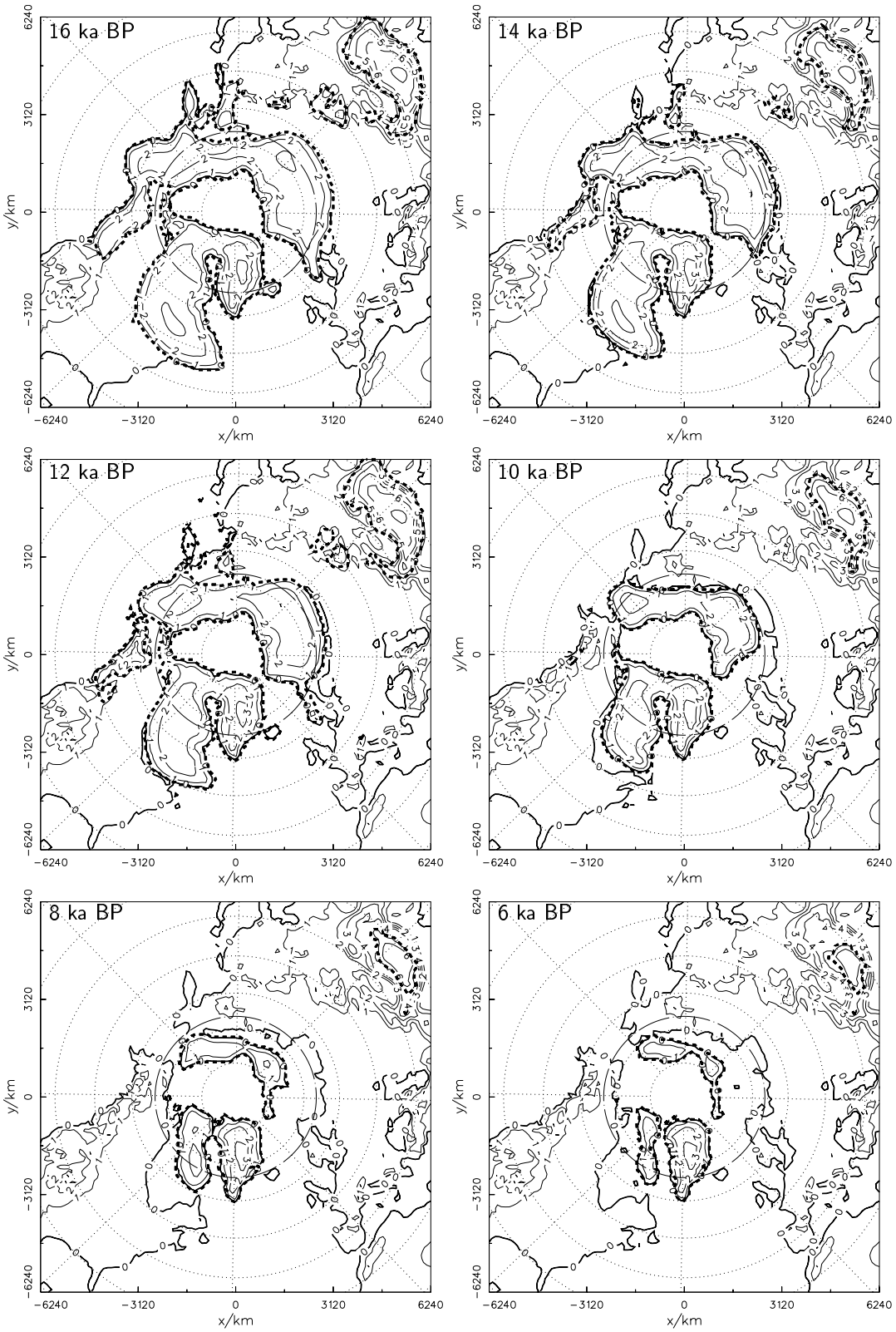

Figure 5: Same as Fig. 4, but for deglaciation during Termination I (t = 16, 14, 12, 10, 8, 6 ka BP).

7 Conclusion

The results of the simulations of northern hemisphere glaciation, in particular the GRIP-driven one, provide good agreement for the rates and total amounts of the deglaciations during Terminations I and II when compared to the SPECMAP record. Further, they support the evidence from the Houtman Abrolhos coral reef data of different deglaciation histories in relation to Milankovitch forcing at 65°N during these events. While the timing details between the simulation results and the sea-level history inferred from the data differ, the insolation lead/lag relationships are the same, which makes it more difficult to reject the high-resolution TIMS U-series dates as diagenetic artefacts.

If our views are correct, some adjustment may have to be made to the SPECMAP chronology, which is tuned to insolation at this latitude. More important, however, is the insight that there is no straightforward causality relation between 65°N insolation and northern hemisphere deglaciation. Of course, this immediately raises the question what, if not Milankovitch forcing, is the reason for global sea level changes. A promising way out of this dilemma is the idea to replace the single forcing latitude by a latitude-dependent insolation forcing in order to meet the complexity of the climate system more adequately.

Acknowledgements

The adaption of the ice-sheet model SICOPOLIS to the entire northern hemisphere was performed during a visit of R. Greve at the Antarctic CRC, Hobart, Tasmania. I wish to thank K. Hutter for his impetus to arrange this visit, the ice-sheet-modelling group of the Antarctic CRC, in particular W. F. Budd, B. Coutts, T. H. Jacka and R. Warner for their help and hospitality during this time, and the Adolf-Messer-Stiftung for generous financial support. The comments of M. Prentice and an anonymous reviewer on an earlier version of the manuscript have helped considerably to improve the writing and clarity of this paper.

Article 8 *Ann. Glaciol.*, **27**, 201-206, 1998

Simulation of the Antarctic ice sheet with a three-dimensional polythermal ice sheet model, in support of the EPICA project

Reinhard Calov[†], Alexej Savvin[†], Ralf Greve[†], Imke Hansen[‡] and Kolumban Hutter[†]

[†]Institut für Mechanik, Technische Universität Darmstadt, D-64289 Darmstadt, Germany

[‡]Universität Bremen, FB5 – Geowissenschaften, D-28334 Bremen, Germany

Abstract

The 3-d polythermal ice-sheet model SICOPOLIS is applied to the entire Antarctic ice sheet in order to support the European Project for Ice Coring in Antartica (EPICA). In this study, we focus on the deep ice core to be drilled in Dronning Maud Land (Atlantic sector of east Antarctica) as part of EPICA. It has not yet been decided where the exact drillsite will be situated. Our objective is to support EPICA during its planning phase as well as during the actual drilling process.

We discuss a transient simulation with a climate forcing derived from the Vostok ice core and the SPECMAP sea-level record. This simulation shows the range of accumulation, basal temperature, age and shear deformation to be expected in the region of Dronning Maud Land. Based on these results, a possible coring position is proposed, and the distribution of temperature, age, horizontal velocity and shear deformation is shown for this column.

1 Introduction

The recently drilled deep ice cores GRIP ("Greenland Ice Core Project"), GISP2 ("Greenland Ice Sheet Project") and Vostok (in east Antarctica), which reach back more than 200 kyr and thus cover two full glacial/interglacial cycles, have considerably improved our knowledge about the palaeoclimate. In order to complement the information from these ice cores by further data and find answers to still open questions (such as the occurrence of rapid climate variations in the Eemian and the coupling of climate changes between the northern and the southern hemisphere), several further ice-core projects in Antarctica are planned, an international effort coordinated by the Scientific Committee on Antarctic Research (SCAR). Europe's contribution

to this campaign is the European Project for Ice Coring in Antarctica (EPICA), an outcome of the European Committee on Ocean and Polar Sciences (ECOPS). Within this programme, it is planned to drill two deep ice cores in Antarctica, one at Dome Concordia (central east Antarctica) and one in Dronning Maud Land (Atlantic sector of east Antarctica, see Fig. 1). The former is expected to provide an archive which covers more than 500 kyr of climate history, whereas the latter, to be drilled in a region influenced by precipitation sources from the south Atlantic and with relatively large accumulation rates, concentrates on rapid climate changes in the most recent glacial/interglacial cycle (Jouzel et al., 1994).

In this study, we present a preliminary simulation with the 3-d polythermal ice-sheet model SICOPOLIS ("SImulation COde for POLythermal Ice Sheets") for the Antarctic ice sheet in order to offer model support for the ice core in Dronning Maud Land. During the planning phase, the simulation results are helpful in determining the optimum drillsite. Besides a large accumulation rate necessary to obtain the desired high temporal resolution of the climate archive, criteria for this are (i) the thermal conditions at the bedrock (avoiding basal ice at pressure melting), (ii) the age of near-basal ice and, from an engineering point of view, (iii) the shear rate in the borehole. During the actual drilling process, the age-depth profile of the ice core must be computed by flow modelling in the deeper regions where stratigraphic techniques are not feasible. Further, flow modelling is required to find the geographic origin of the ice in the core. This must be done with the highest sophistication possible to obtain optimum results, and should therefore not be done by simple steady-state flowline modelling.

2 Ice-sheet model SICOPOLIS

SICOPOLIS is a 3-d dynamic/thermodynamic ice-sheet model based on the continuum-mechanical theory of polythermal ice masses (Fowler and Larson, 1978; Hutter, 1982, 1993; Calov and Hutter, 1997; Greve, 1997a). It simulates the time-dependent extent, thickness, velocity, temperature, water-content and age for a grounded ice sheet in response to external forcing. Further, possible basal layers of temperate ice are detected with high vertical resolution by fulfilling the Stefan-type conditions at the cold-temperate-transition surface. External forcing is specified by (i) mean annual air temperature above the ice, (ii) surface mass balance (accumulation, surface melting), (iii) sea level surrounding the ice sheet and (iv) geothermal heat flux from below. The dynamics of the adjacent ice shelves is not accounted for. The model is discussed in greater detail by Greve (1995, 1997b), Hansen and Greve (1996).

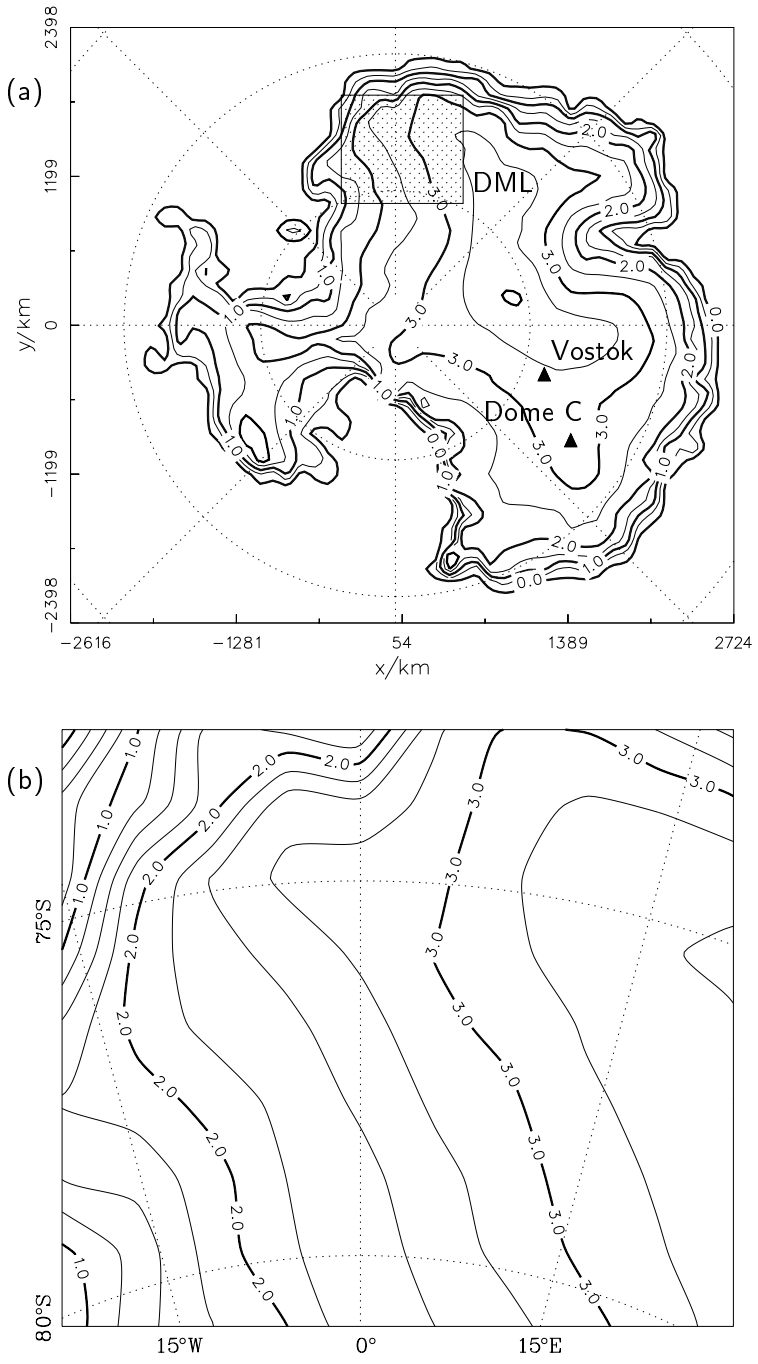

Figure 1: (a) Measured surface topography of the present Antarctic ice sheet, by Drewry (1983). Ice shelves are ignored. The shaded area marks the region in Dronning Maud Land (DML) where the EPICA core will be drilled (Jouzel et al., 1994). Surface elevations in km a.s.l. (contour spacing 500 m). (b) Close-up of the coring region in Dronning Maud Land (contour spacing 250 m).

In this study, SICOPOLIS is applied to the Antarctic ice sheet. The results of the transient palaeoclimatic simulation epc46 which covers two entire glacial/interglacial cycles are presented, with special emphasis on the region of Dronning Maud Land. Horizontal grid spacing is 109 km. The vertical resolution is 51 grid points in the cold-ice region (temperature below pressure melting), 11 grid points in the temperate-ice region (temperature at pressure melting) if existing, and 11 grid points in the lithosphere.

3 Simulated present state of Dronning Maud Land

3.1 Model set-up

In order to provide an optimum present state of the Antarctic ice sheet and to avoid prescribing lateral boundary conditions, the transient palaeoclimatic simulation epc46 was carried out for the ice sheet *as a whole*. This simulation covers 242200 years of climate history (two climatic cycles), parameterized by the temperature reconstruction $\Delta T_{\mathrm{ma}}(t)$ of the Vostok ice core (Jouzel et al., 1993, 1996) and the SPECMAP sea-level record $z_{\mathrm{sl}}(t)$ (Imbrie et al., 1984). It was initialized by a previous 100000 year steady-state run forced by the climate conditions at 242200 years before present. In this initialization run the lithosphere temperature was assumed to be in equilibrium with the geothermal heat flux from below and the temperature at the ice base at any time in order to reach the steady state within 100000 years.

It is assumed that the spatial distributions of the mean annual and summer air temperature above the ice, T_{ma} and T_{su}, respectively, remain unchanged through time, so that

$$\begin{aligned} T_{\mathrm{ma}}(x,y,z,t) &= T_{\mathrm{ma}}^{\mathrm{today}}(x,y,z) + \Delta T_{\mathrm{ma}}(t), \\ T_{\mathrm{su}}(x,y,z,t) &= T_{\mathrm{su}}^{\mathrm{today}}(x,y,z) + \Delta T_{\mathrm{ma}}(t). \end{aligned} \tag{3.1}$$

Here, $T_{\mathrm{ma}}^{\mathrm{today}}$ and $T_{\mathrm{su}}^{\mathrm{today}}$ are the *present* distributions of the mean annual and summer air temperature above the ice, respectively, for which the parameterizations by Huybrechts (1993) are applied. x, y, z are Cartesian coordinates: x, y span the horizontal plane, z points upward.

For the present accumulation rate, S^{today}, we made up a new map, which is based on 45 data points by Neethling (1970), Picciotto et al. (1970), Isaksson and Karlén (1994), Mulvaney and Wolff (1994), Paterson (1994) and Isaksson et al. (1996) in the surrounding of the coring region in Dronning Maud Land (see Figs. 2, 3). Under climatic conditions different from those of today a linear relationship between the accumulation rate S and the temperature deviation ΔT_{ma} is assumed:

$$S(x,y,t) = S^{\mathrm{today}}(x,y) \times (1 + \gamma_{\mathrm{s}} \Delta T_{\mathrm{ma}}), \quad \text{with } \gamma_{\mathrm{s}} = 0.08286^{\circ}\mathrm{C}^{-1}. \tag{3.2}$$

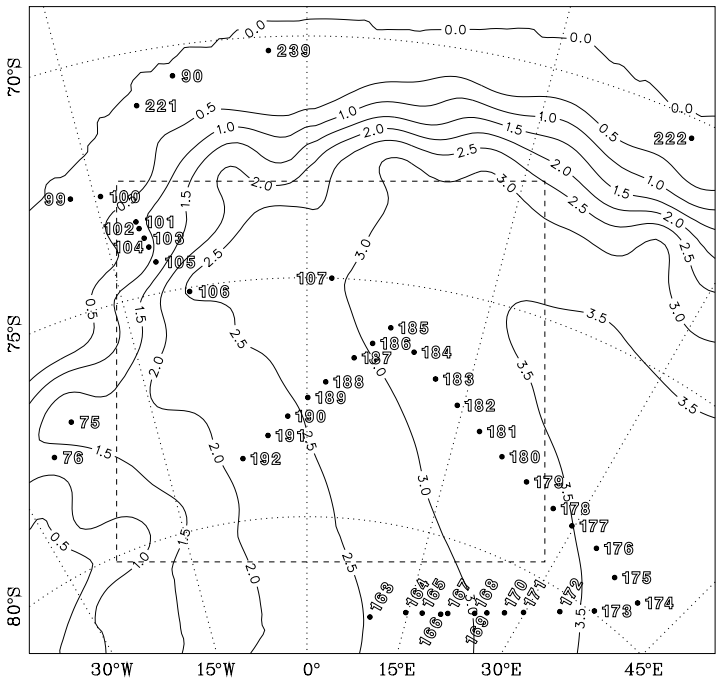

Figure 2: Positions of accumulation measurements in the vicinity of the coring region in Dronning Maud Land (the latter is situated within the dashed rectangle), on which the accumulation map used for the simulation is based. Nos. 75-90 by Mulvaney and Wolff (1994), nos. 99-106 by Isaksson and Karlén (1994), no. 107 by Isaksson et al. (1996), nos. 163-192 by Picciotto et al. (1970), nos. 221-222 by Paterson (1994), no. 239 by Neethling (1970). Contours are surface elevations in km a.s.l.

The parameter γ_{s} is chosen such that the accumulation rate is reduced by 50% for the lowest temperature of the Vostok reconstruction, $\Delta T_{\mathrm{ma}} = -6.04°\mathrm{C}$.

Surface melting is parameterized by the degree-day approach with the degree day factors $\beta_{\mathrm{snow}} = 3\,\frac{\mathrm{mm\,WE}}{\mathrm{d}\cdot°\mathrm{C}}$ and $\beta_{\mathrm{ice}} = 8\,\frac{\mathrm{mm\,WE}}{\mathrm{d}\cdot°\mathrm{C}}$, the firn saturation rate $P_{\mathrm{max}} = 60\%$ and the standard deviation $\sigma_{\mathrm{stat}} = 5°\mathrm{C}$ for statistical air-temperature fluctuations (Reeh, 1991). The geothermal heat flux is $Q^{\perp}_{\mathrm{geoth}} = 54.6\,\mathrm{mW/m^2}$ (Huybrechts, 1993). The bedrock topography is by Drewry (1983). Further physical parameters are the same as those applied by Greve et al. (1998), except for the enhancement factor in Glen's flow law, for which the spatially and temporally uniform value $E = 5$ is used here.

3.2 Results

We discuss now the results of the simulation described above for the present state of the coring region in Dronning Maud Land (Fig. 1). In Figs. 4-7 are depicted the computed surface elevation, h, homologous basal temperature, T'_{b} (that is, corrected for the pressure melting point), age at 85% depth, A_{85}, and basal shear deformation, S_{h}, respectively.

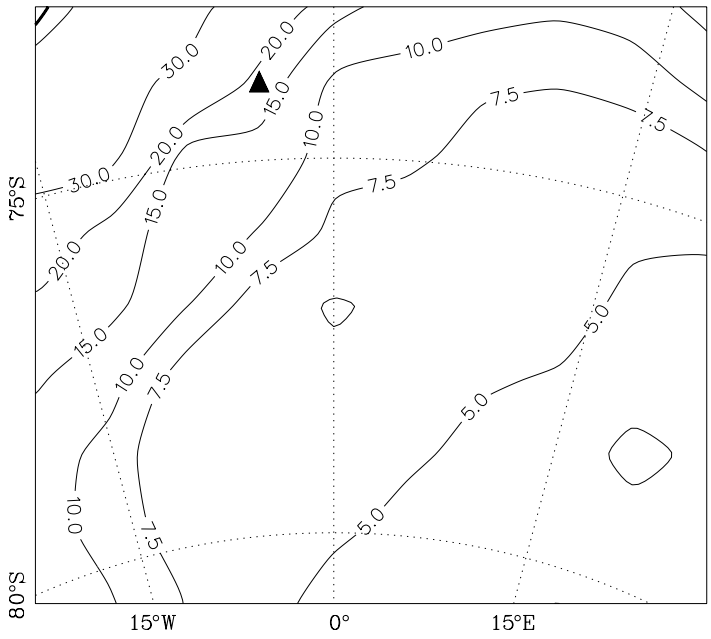

Figure 3: Interpolated accumulation pattern resulting from the measurements of Fig. 2 for the coring region in Dronning Maud Land (in cm IE/yr). The proposed drillsite is marked by the full triangle.

Comparison of Figs. 1b and 4 shows that the simulated surface topography is in reasonable agreement with the measured one. The most conspicuous discrepancy concerns the surface gradient (and therefore the flow direction) in the south-east part of the depicted region where the modelled and measured directions differ by 55°. This demonstrates the preliminary nature of the presented results, which is on the one side due to still insufficient information about the bedrock topography and the accumulation pattern, and on the other side due to the coarse horizontal resolution and perhaps the neglection of the effect of normal stress gradients on the ice flow (see below).

The basal temperature shown in Fig. 5 reveals a rather large variety, covering a range from below −20°C to pressure melting. For five grid points in the western part even a basal *layer* of temperate ice is predicted. Since the water flow in temperate ice disturbs the stratigraphy of a potential ice core, the vicinity of these points must be avoided as coring positions.

The age at 85% depth (Fig. 6) increases distinctly from north-west to south-east due to the decreasing accumulation (Fig. 3) and the increasing thickness. The objective of the EPICA ice core in Dronning Maud Land is not to provide basal ice as old as possible, but to provide a climate archive with high temporal resolution for the most recent climate cycle. The latter is certainly covered by the condition

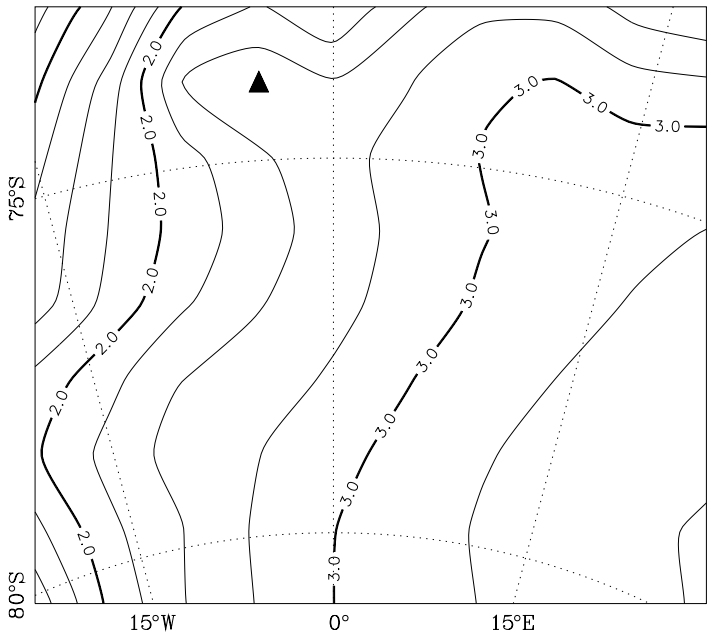

Figure 4: Simulated (epc46) surface topography of the coring region in Dronning Maud Land. Surface elevations in km a.s.l. (contour spacing 250 m). The proposed drillsite is marked by the full triangle.

$A_{85} \geq 100\,\mathrm{kyr}$, which excludes as possible drillsites only positions in the north-western corner of the considered region.

Numerical diffusion introduced in the age computation and currently unavoidable to keep the numerical integration stable affects the computed age values most conspicuously in a near-basal boundary layer which was found to be 15% of the ice thickness for similar simulations of the Greenland ice sheet (Greve et al., 1998). In the rest of the ice sheet the influence of the artificial diffusion is virtually negligible because its associated time scale is much larger than the time scale for the physical process of advection which governs the evolution of the age field (Greve, 1997c). As a result, we are not yet able to give a reasonable prediction for the *basal* age of the ice, even though the computed and depicted values for A_{85} should be reliable from a numerical point of view (see also Appendix A, where this is demonstrated with analytical solutions of the 1-d steady-state age equation with and without diffusion). Future work must consequently aim at avoiding the numerical diffusion by either adopting a more stable discretization scheme for the purely advective age equation, or by applying a direct particle-tracing algorithm. Such studies are on the way.

The basal shear deformation, defined by

$$S_\mathrm{h} = \left\{ \left(\frac{\partial v_x}{\partial z} \right)^2 + \left(\frac{\partial v_y}{\partial z} \right)^2 \right\}^{1/2} \tag{3.3}$$

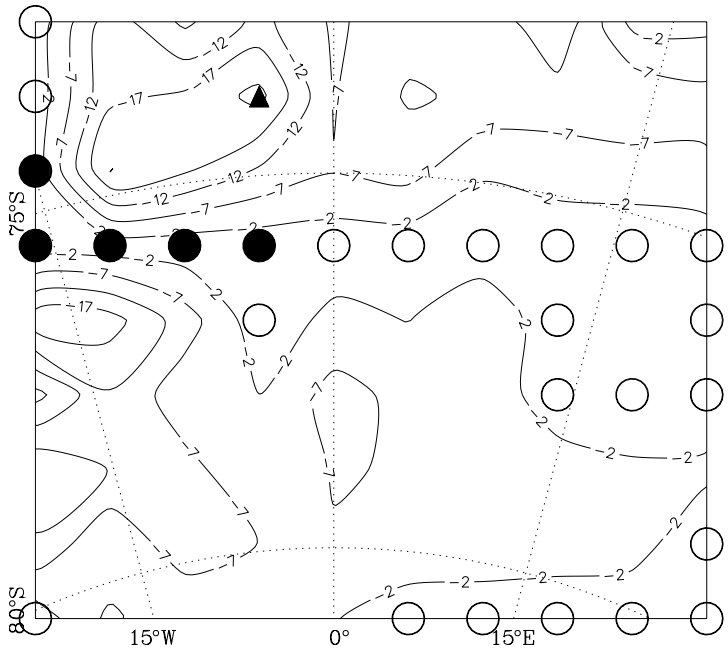

Figure 5: Simulated (epc46) basal temperatures for the coring region in Dronning Maud Land, corrected for pressure melting (in °C, spacing 5°C). Open circles (full circles) indicate grid points where the basal ice is at pressure melting without (with) an overlain layer of temperate ice. The proposed drillsite is marked by the full triangle.

(where v_x and v_y are the velocities in x- and y-direction, respectively), should be as small as possible at the drillsite to minimize the strain on the drill stem. Fig. 7 demonstrates that S_h varies by more than a factor of 30 in the considered coring region, namely from below $0.01\,\mathrm{yr}^{-1}$ to above $0.3\,\mathrm{yr}^{-1}$. One may restrict the tolerable shear deformation to a maximum of $0.03\,\mathrm{yr}^{-1}$, which leaves slightly less than half of the region as possible drillsites.

3.3 Preliminary proposal of a drillsite

With the findings of the simulation discussed above, a preliminary proposal for the position of the EPICA ice core to be drilled in Dronning Maud Land can be made. It is the grid point with the coordinates 73° 57′ S, 03° 35′ W, situated on a saddle in the north-west of the region considered for coring. This position is marked by the full triangles in Figs. 3-7, and it is characterized by the following simulated values:

surface elevation	2684 m a.s.l.,
bedrock elevation	1492 m a.s.l.,
accumulation rate	18.1 cm IE/yr,
basal temperature	−24.7°C,
age at 85% depth	111 kyr,

basal age (uncertain!)	262 kyr,
basal shear deformation	$0.0187\,\mathrm{yr}^{-1}$.

Evidently, the criteria for the choice of the drillsite are fulfilled very satisfactorily. The accumulation rate is sufficiently large to ensure a high temporal resolution, the basal temperature is far below melting, the most recent climate cycle is captured entirely (even though the value for the basal age is not reliable due to the disturbing effect of numerical diffusion, see above), and the basal shear deformation is small.

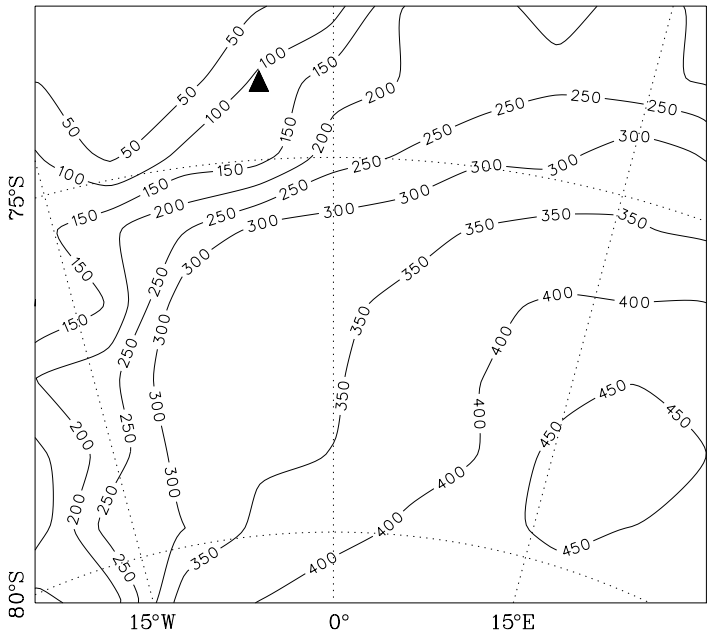

Figure 6: Simulated (epc46) age at 85% depth for the coring region in Dronning Maud Land (in kyr, spacing 50 kyr). The proposed drillsite is marked by the full triangle.

For further illustration, the depth profiles of the temperature, T, the age, A, the horizontal velocity, v_h, and the basal shear deformation, S_h, are depicted in Fig. 8 for this position. As is typical for age-depth profiles of ice columns, the gradient is very small in the upper part where the accumulated ice layers remain essentially unchanged. By contrast, layer thinning due to ice spreading causes a distinctly larger gradient in the lower part, which explains also the big difference between the age at 85% depth and the basal age. Owing to the increase of shear stress with depth and the nonlinearity of Glen's flow law, the main shear deformation takes place in the lowermost quarter of the column. Consequently, the strain on the drill stem is very small above this near-basal part.

However, the above results must be regarded as preliminary. The still poorly known bedrock topography and the lack of accumulation measurements in large parts of the coring region may lead to inaccuracies of the simulation results. Further measurements will be carried out in Dronning Maud Land within the EPICA project, so

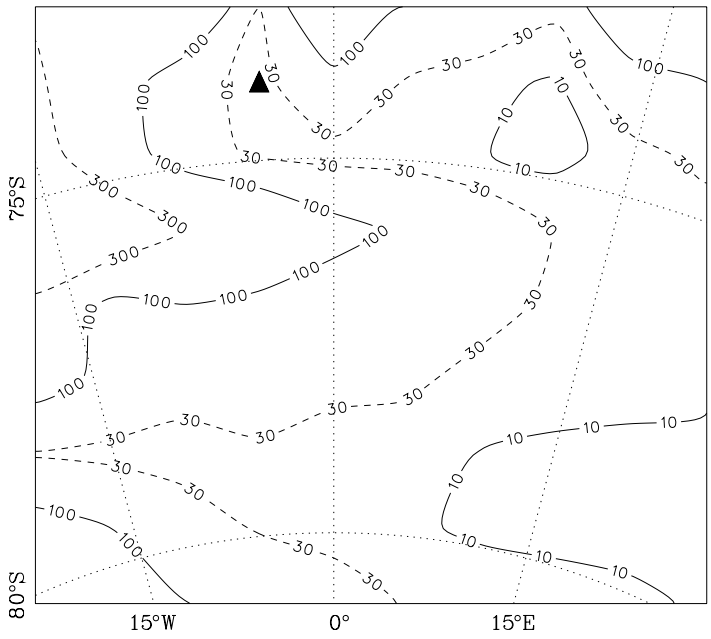

Figure 7: Simulated (epc46) basal shear deformation for the coring region in Dronning Maud Land (in $10^{-3}\,\mathrm{yr}^{-1}$). The proposed drillsite is marked by the full triangle.

that this shortcoming can be remedied in the future. Parallel to the completion of these input data, a grid refinement for the coring region in Dronning Maud Land will be implemented in our model in order to provide simulation results with higher spatial resolution. Owing to the mountain ranges of Maudheimvidda and Fimbulheimen situated downstream of the coring region, normal stress gradients which are neglected in the shallow-ice approximation on which the model is based (Greve, 1997a) may have a noticeable effect on the ice flow. Therefore, the contribution of these stress components will be accounted for in the high-resolution coring region.

4 Conclusion

The 3-d dynamic/thermodynamic ice-sheet model SICOPOLIS was applied to the Antarctic ice sheet, and the computed present state of Dronning Maud Land which results from a palaeoclimatic simulation along two climatic cycles was discussed. The objective is to provide model support for the EPICA ice core which is planned in this region. A possible drillsite is proposed based on suitable values for the accumulation rate, basal temperature, age and basal shear deformation, and a preliminary age-depth profile for this position is given.

Our future aim is to improve the model set-up in close coorporation with the EPICA project members, who will supply new data from observations in Dronning Maud Land. In particular, a more precise bedrock topography, additional accumula-

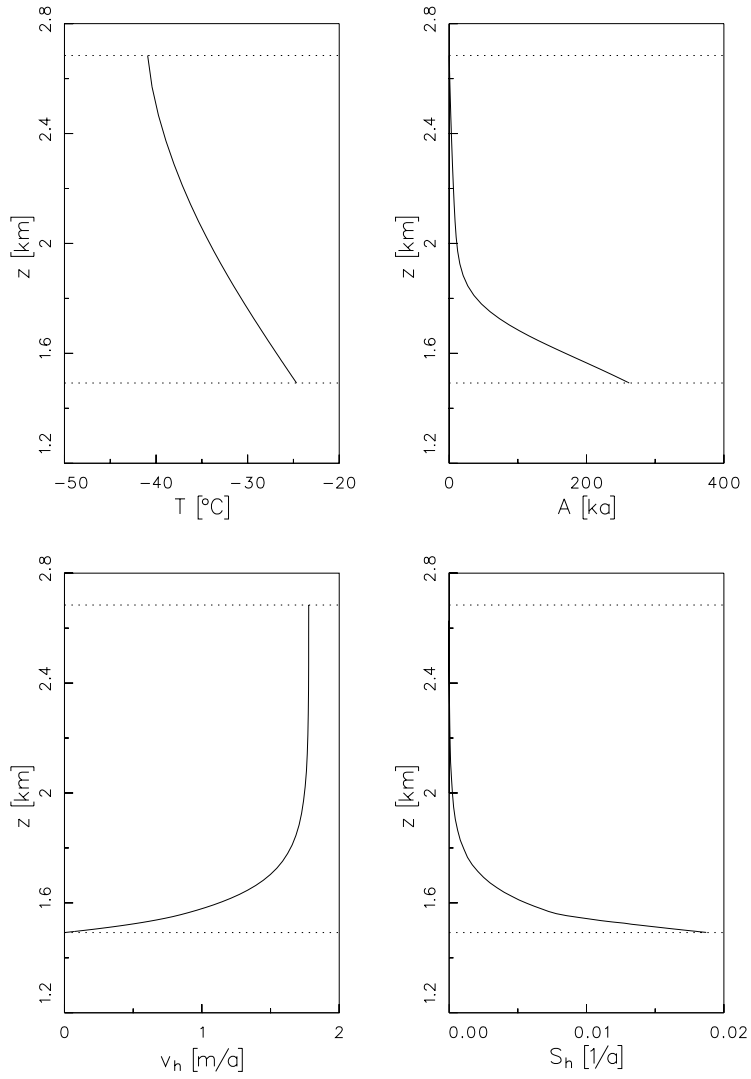

Figure 8: Simulated (epc46) depth profiles of temperature, age, horizontal velocity and shear deformation for the proposed drillsite at 73° 57′ S, 03° 35′ W.

tion data and information on flow properties of the ice will be implemented in order to ensure a proper modelling of this region. Together with the implementation of a grid refinement and the consideration of normal stress gradients, this will lead to more accurate results which can be used to determine the final coring position. Furthermore, the computation of age-depth profiles (dating) will be improved by applying a diffusion-free algorithm for the advective age equation.

Acknowledgements

We wish to thank Prof. Ian Whillans, Mr. Erik Venteris, M. Sc., Dr. Heinz Blatter and Dr. Robert Mulvaney for supplying data on the Antarctic snow accumulation, and Dr. Richard Hindmarsh, Dr. Tómas Jóhannesson and Dr. Andrew Kerr for their

helpful comments of the original draft of this paper. The support by the Deutsche Forschungsgemeinschaft under project no. Hu 412/19-2 is gratefully acknowledged.

A Analytical solution of the 1-d age equation

Consider the one-dimensional steady-state equation for the age A,

$$v_z \frac{dA}{dz} = 1, \qquad A(z=h) = 0, \tag{A.1}$$

the normalized ice-sheet geometry $b = 0$ (ice base), $h = 1$ (ice surface), and the normalized constant downward velocity $v_z = -1$. Under these conditions, the solution of eq. (A.1) is simply

$$A(z) = 1 - z. \tag{A.2}$$

Let us add some numerical diffusion to eq. (A.1):

$$v_z \frac{dA}{dz} = 1 + D_{\mathrm{A}} \frac{d^2A}{dz^2}, \qquad A(z=h) = 0, \tag{A.3}$$

where D_{A} is the numerical diffusivity. The solution of this modified problem is

$$A_{\mathrm{diff}}(z) = 1 - z + C\left(e^{(1-z)/D_{\mathrm{A}}} - 1\right), \tag{A.4}$$

the constant C is undefined due to the parabolic nature of eq. (A.3). With the artificial Neumann-type basal boundary condition

$$\left.\frac{dA}{dz}\right|_{z=0} = -\Gamma_{\mathrm{A}} \tag{A.5}$$

(Γ_{A}: prescribed basal age gradient), its value is

$$C = D_{\mathrm{A}}(\Gamma_{\mathrm{A}} - 1)\, e^{-1/D_{\mathrm{A}}}, \tag{A.6}$$

and thus, from eq. (A.4),

$$A_{\mathrm{diff}}(z) = 1 - z + D_{\mathrm{A}}(\Gamma_{\mathrm{A}} - 1)\left(e^{-z/D_{\mathrm{A}}} - e^{-1/D_{\mathrm{A}}}\right). \tag{A.7}$$

With eqs. (A.2) and (A.7), the influence of the artificial diffusion on the age function can be quantified in terms of the error

$$e(z) = A_{\mathrm{diff}}(z) - A(z) = D_{\mathrm{A}}(\Gamma_{\mathrm{A}} - 1)\left(e^{-z/D_{\mathrm{A}}} - e^{-1/D_{\mathrm{A}}}\right). \tag{A.8}$$

Table 1 shows $e(z)$ for $z = 0$, 0.01, 0.15, 0.5, 1, four different diffusivities D_{A} and the basal gradient $\Gamma_{\mathrm{A}} = 200$, which was used in the actual 3-d simulation discussed in this paper. Evidently, with decreasing diffusivity, the diffusion effect on the computed age concentrates more and more on a near-basal boundary layer as it was claimed

	Surface	50% depth	85% depth	99% depth	Base
$D_A = 1$	0	4.75×10^{1}	9.81×10^{1}	1.24×10^{2}	1.26×10^{2}
$D_A = 0.1$	0	1.33×10^{-1}	4.44×10^{0}	1.80×10^{1}	1.99×10^{1}
$D_A = 0.01$	0	3.84×10^{-22}	6.09×10^{-7}	7.32×10^{-1}	1.99×10^{0}
$D_A = 0.001$	0	$< 1.00\times10^{-40}$	$< 1.00\times10^{-40}$	9.03×10^{-6}	1.99×10^{-1}

Table 1: Error of the age function $A(z)$ due to numerical diffusion. Prescribed basal gradient $\Gamma_A = 200$.

in section 3.2, and, for $D_A \leq 0.01$, the error is indeed negligible at least down to 85% depth. With the thickness scale $[H] = 2000\,\mathrm{m}$, the vertical-velocity scale $[V] = 0.1\,\mathrm{m\,yr^{-1}}$ and the time scale $[T] = [H]/[V]$, the dimensional diffusivity $5\times10^{-8}\,\mathrm{m^2\,s^{-1}}$ used in the simulation corresponds to the normalized value

$$D_A = 5 \times 10^{-8}\,\mathrm{m^2\,s^{-1}} \times \frac{[T]}{[H]^2} = 7.89 \times 10^{-3}. \tag{A.9}$$

The numerical scheme itself is diffusion-free in the vertical because vertical advection is discretized by centered differences (instead of horizontal advection for which an upwind scheme is applied). Therefore, our assertion that the computed ages down to 85% depth are basically unaffected by the numerical diffusion is supported.

Simulation of the Antarctic ice sheet with a 3-d polythermal ice-sheet model, in support of the EPICA project. Part II: Nested high-resolution treatment of Dronning Maud Land

Alexej Savvin[†], Ralf Greve[†], Reinhard Calov[‡], Bernd Mügge[†] and Kolumban Hutter[†]

[†]Institut für Mechanik, Technische Universität Darmstadt, D-64289 Darmstadt, Germany

[‡]Potsdam-Institut für Klimafolgenforschung, Postfach 601203, D-14412 Potsdam, Germany

Abstract

The modern dynamic and thermodynamic state of the entire Antarctic ice sheet is computed as the result of a 242200-year paleoclimatic simulation with the 3-d polythermal ice-sheet model SICOPOLIS. The simulation is driven by a climate history derived from the Vostok ice core and the SPECMAP sea-level record. In a 872×436 km region in western Dronning Maud Land (DML), where a deep ice core is planned within the frame of the European Project for Ice Coring in Antarctica (EPICA), new high-resolution ice-thickness data are implemented (in order to compute an improved bedrock topography) and a locally refined numerical grid is applied, which goes beyond the predecessor of this study (Calov et al., *Ann. Glaciol.*, **27**, 201-206, 1998). The computed fields of basal temperature, age and shear deformation together with the measured accumulation rates give valuable information for the selection of a suitable drill-site in accordance with the objective to obtain a high-resolution climate record for the last glacial cycle. Based on these results, a possible drill-site at 73° 59′ S, 00° 00′ E is discussed, for which the computed depth profiles of temperature, age, velocity and shear deformation are presented. The geographic origin of the ice column at this position extends 320 km upstream and therefore does not leave the DML region.

1 Introduction

The European Project for Ice Coring in Antarctica (EPICA) is a European initiative to drill two deep ice cores in East Antarctica. In the current first five-year phase

(until December 2000) an ice core is drilled at Dome C (central East Antarctica, see Fig. 1), which is characterized by low-shear ice flow and a snow accumulation rate of about 3.5 cm water equivalent (w.e.) per year, and is expected to provide a climate archive which covers five entire glacial-interglacial cycles (500 ka). A further objective is to conduct field studies in the Atlantic sector of East Antarctica as a prerequisite for drilling a core in Dronning Maud Land (DML) in the second phase of EPICA. In contrast to Dome C, the planned DML core is focussed on rapid climate changes within the last glacial-interglacial cycle (100 ka) in a region under the influence of South Atlantic precipitation sources and a much larger accumulation rate.

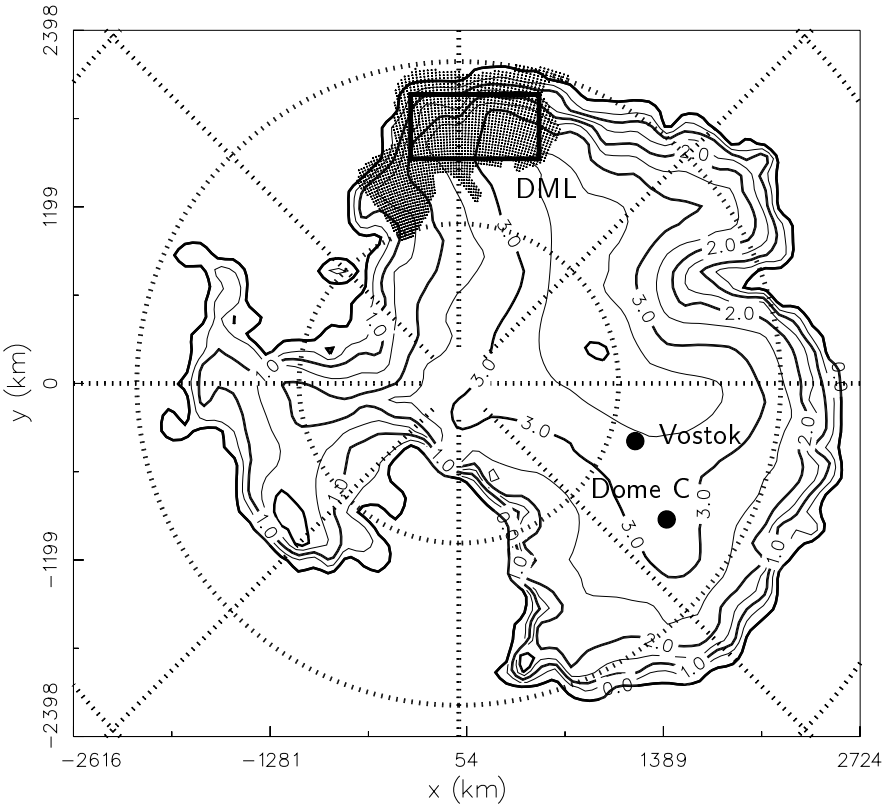

Figure 1: Surface topography of the modern Antarctic ice sheet, by Drewry (1983) (without ice shelves; in km a.s.l., contour spacing 500 m). The dots in DML denote ice-thickness data points of the recent AWI campaign (see section 2.3), the rectangle within this region the nested domain for the ice-sheet model.

The position of the DML drill-site has not yet been established. In accordance with the aims of the coring, criteria which can be assessed by dynamic/thermodynamic ice-sheet modelling are (i) no melt in the entire ice column in order to avoid disturbances to the stratigraphy by meltwater, (ii) a minimum ice age of 130 ka in order to cover the entire recent climate cycle, (iii) a large accumulation rate in order to resolve rapid climate changes on timescales of decades, and (iv), from a technical point of view, a

small shear strain rate in the borehole (cf. Jouzel et al., 1994). In the predecessor of this study (Calov et al., 1998), a first attempt was made to determine an appropriate position for the DML core by modelling the present state of DML as the result of a paleoclimatic simulation of the entire Antarctic ice sheet through two climate cycles, and investigating the model output with respect to these criteria. This led to a *preliminary* proposal of a drill-site at 73° 57′ S, 03° 35′ W. However, due to severe limitations of the input data available at that time and the coarse grid resolution of the model (109 km) this was seen only as the first step toward an appropriate model support for the EPICA DML core. In this paper we now present and discuss a strongly improved simulation based on high-resolution bedrock data in DML, a new accumulation dataset for Antarctica, and, on the modelling side, a high-resolution subgrid for DML coupled to the previous coarse grid for the entire ice sheet. The drill-site proposal is adjusted according to the new results, and the computed distribution of temperature, age, horizontal velocity and shear deformation is shown for the corresponding ice column.

2 Modelling of Dronning Maud Land

2.1 Large-scale ice-sheet model

The large-scale thermomechanical ice-sheet model SICOPOLIS ("SImulation COde for POLythermal Ice Sheets"), here used for the simulations of the entire Antarctic ice sheet, is based on the continuum-mechanical and thermodynamical theory of polythermal ice sheets in the shallow-ice approximation (Fowler and Larson, 1978; Hutter, 1982, 1993; Greve, 1997b). It computes three-dimensionally the temporal evolution of ice extent, thickness, velocity, temperature, water content and age as a response to external forcing, specified by (i) the mean annual air temperature above the ice, (ii) the surface mass balance, which is ice accumulation (snowfall) minus ablation (melting, evaporation), (iii) the mean global sea level and (iv) the geothermal heat flux from below, imposed 5 km below the ice-bedrock interface in order to account for thermal inertia effects in the lithosphere. Isostasy is treated by a simple local-lithosphere-relaxing-asthenosphere model (LeMeur and Huybrechts, 1996), which balances locally the ice load with the buoyancy of the solid lithosphere in the liquid asthenosphere, and accounts for the asthenosphere viscosity by an isostatic time lag τ_{V}. Ice shelves are ignored, and the ice thickness is set to zero where the ice sheet reaches the coastline. Further general model features are described in greater detail by Greve (1997a), Greve et al. (1998).

The model domain for the entire Antarctic ice sheet consists of a 5341×4796 km rectangle in the stereographic plane with standard parallel 71°S, spanned by Cartesian

coordinates x, y (the vertical coordinate is z). Horizontal resolution is 109 km, so that the domain is discretized by 50×45 grid points. Vertical resolution is 51 grid points in the cold-ice column, 11 grid points in the temperate-ice column (if existing) and 11 grid points in the lithosphere column. Time steps are 2.5 a for the dynamic evolution (ice topography, velocity) and 50 a for the thermodynamic evolution (temperature, water content, age).

2.2 Nesting for Dronning Maud Land

Calov et al. (1998) used simulation results computed on the 109-km grid for the assessment of the present conditions of DML in order to determine a suitable drill-site for the EPICA DML core. As this coarse resolution led to merely 10×9 grid points in the investigated part of DML, it is desirable to carry out simulations at a distinctly higher resolution. This may be achieved by increasing the resolution for the entire ice sheet at the cost of extremely long CPU times. For that reason, we pursue the alternative idea of nesting, that is, the Antarctic ice sheet as a whole is still modelled on the 109-km grid, and for DML a refined subgrid is introduced (Savvin, 1999). On this subgrid, the same model equations as on the coarse grid are solved for the entire ice sheet. Dirichlet-type boundary conditions for the subgrid domain are defined by interpolating the computed coarse-grid fields for surface and bedrock topography, temperature, water content and age onto the margin points of the subgrid. In turn, the subgrid gives back the computed topography to the coarse grid at positions where coarse-grid and refined-subgrid points fall together (dynamic feedback). The inclusion of thermodynamic feedbacks from the refined subgrid to the coarse grid was found to be unfavourable for the numerical stability and is therefore not employed (Savvin, 1999).

The nested domain is chosen as a 872×436 km rectangle which is completely covered by the high-resolution ice thickness data discussed in section 2.3 (Fig. 1). Horizontal resolution is 10.9 km (refinement factor 10), so that the region is now discretized by 81×41 grid points. The time steps for the refined DML computations are 0.1 a for the dynamic evolution and 1 a for the thermodynamic evolution.

It is clear that a necessary prerequisite for accurate subgrid computations is the accuracy of the boundary conditions provided by the coarse grid. In this context, the 109-km coarse-grid resolution turned out to be sufficient because the simulated overall ice topography (not shown) agrees well with the Drewry (1983) data. Therefore, and also in order not to increase the required CPU times drastically, no increased coarse-grid resolution was applied.

The horizontal subgrid resolution of 10.9 km is not more than three times the maximum ice thickness in DML. This is on the edge of applicability of the shallow-

ice approximation because normal stress deviators become increasingly important on horizontal scales comparable to the ice thickness. Therefore, in a similar study for the Summit region of the Greenland ice sheet higher-order algorithms are employed for the nested region which include the normal-stress effects (Baral, 1999; Greve et al., 1999). The inclusion of such algorithms for the nested DML domain will be done in the future.

2.3 Bedrock topography

As a part of the DML reconnaissance within the first phase of EPICA, airborne radio-echo-sounding (RES) measurements of the ice thickness at an average resolution of 20 km were conducted and evaluated by a survey campaign of the Alfred-Wegener-Institut für Polar- und Meeresforschung (AWI) (Steinhage et al., 1999; Figs. 1, 2b). This is of particular importance because the classical maps of the Antarctic ice sheet by Drewry (1983) are based on rather sparse data in DML, so that their accuracy does not meet the requirements for the EPICA DML project. With the new high-resolution ice-thickness data, a much more precise bedrock map was constructed by first interpolating them on the numerical 10.9-km grid for DML, and then subtracting them from Drewry's (1983) already gridded surface topography (Fig. 2a). The isostatically relaxed bedrock topography for vanishing ice load, $z = b_0(x, y)$, which is required for the simulations, is finally computed under the assumption that the present bedrock, $z = b(x, y)$, is close to local isostatic equilibrium with its ice load, so that $b_0(x, y) = b(x, y) + (\rho/\rho_a) \times H(x, y)$ (where H is ice thickness, ρ ice density, ρ_a asthenosphere density). The result is shown in Fig. 2c.

2.4 Snow accumulation

Giovinetto, Zwally and Bentley (pers. comm. 1997, publication in preparation) compiled a new accumulation dataset which includes approximately 1700 data points for the entire Antarctic ice sheet. This is a distinct improvement compared to the 550 data points on which the simulation of Calov et al. (1998) was based. For the simulations of this study, the dataset of Giovinetto, Zwally and Bentley is interpolated onto the coarse 109-km numerical grid for the entire Antarctic ice sheet as well as onto the refined 10.9-km DML grid. Fig. 3 depicts the resulting accumulation pattern in DML, which shows a clear increase from the inland toward the coast.

2.5 Simulation set-up

Similar to Calov et al. (1998), the present state of the Antarctic ice sheet and DML in particular is modelled as the result of the paleoclimatic simulation awi18 from 242200

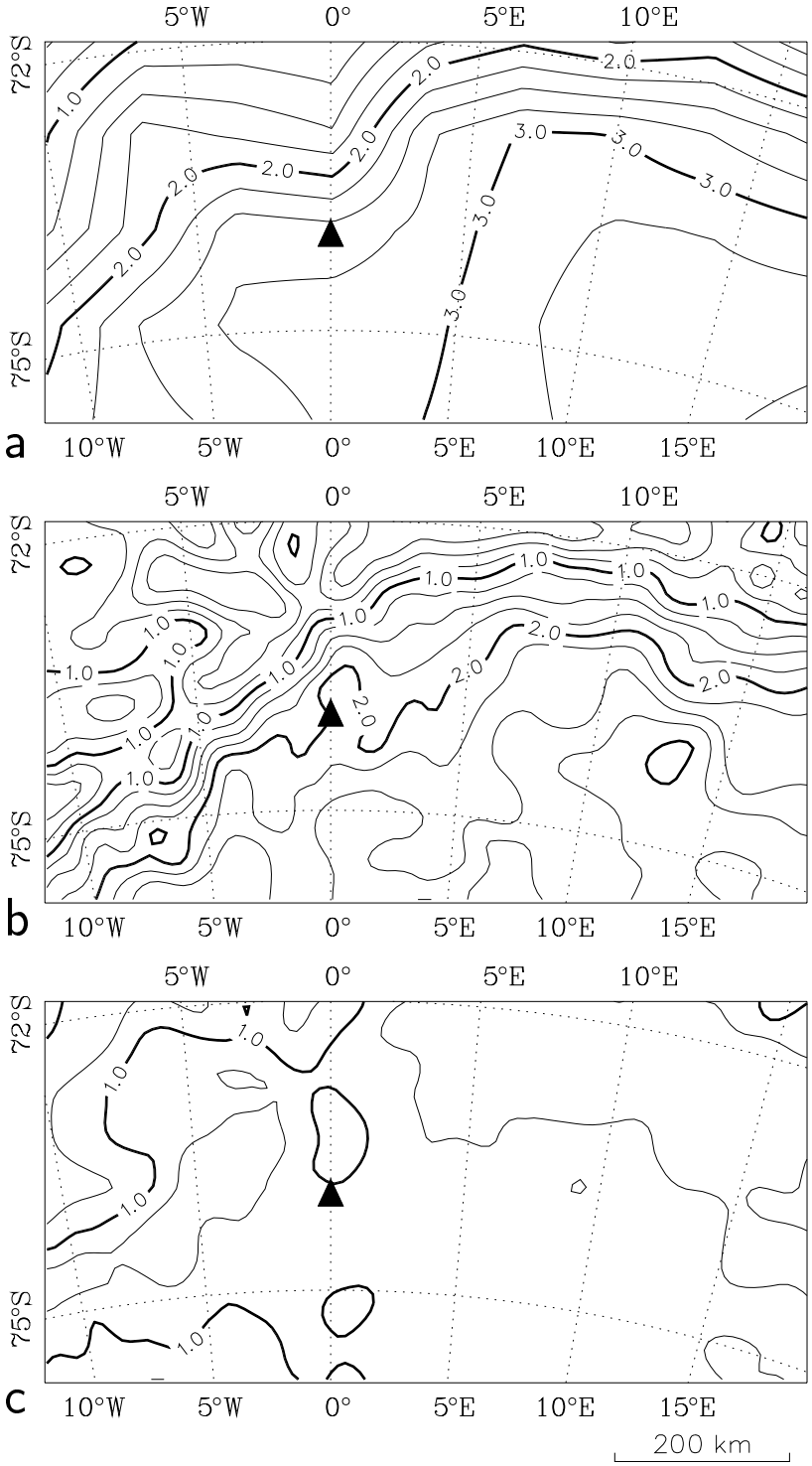

Figure 2: Nested domain in DML. (a) Modern surface topography by Drewry (1983) (in km a.s.l., contour spacing 250 m). (b) Modern ice thickness measured by the AWI campaign (see section 2.3; in km, contour spacing 250 m). (c) Isostatically relaxed bedrock topography for vanishing ice load (in km a.s.l., contour spacing 250 m). The proposed drill-site is marked by the full triangle.

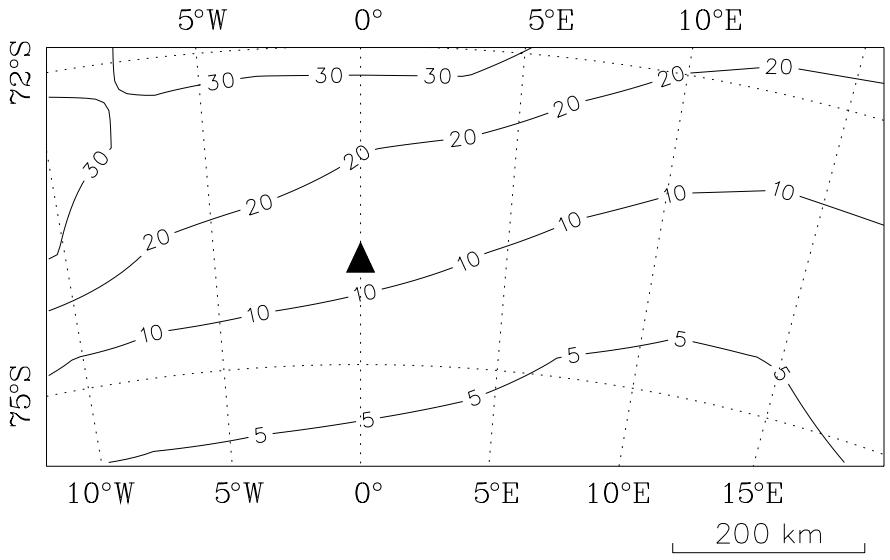

Figure 3: Modern snow accumulation in DML, by Giovinetto, Zwally and Bentley (pers. comm. 1997, publication in preparation) (in cm ice equivalent a^{-1}). The proposed drill-site is marked by the full triangle.

years BP until today, initialized by a previous 100000-year steady-state run for the conditions at 242200 years BP. The simulation is driven by surface-temperature and sea-level histories derived from the Vostok ice core (Jouzel et al., 1993, 1996) and the SPECMAP sea-level record (Imbrie et al., 1984), respectively, and for the present reference state of the surface temperature the parameterizations given by Huybrechts (1993) are used. The accumulation input is based on the modern dataset discussed in section 2.4, modified by a time-dependent factor coupled linearly to the surface-temperature deviation from today (Calov et al., 1998). Surface melting is modelled by a degree-day approach with the parameters $\beta_{\mathrm{snow}} = 3\,\mathrm{mm\,w.e.\,d^{-1}K^{-1}}$ (snow melt), $\beta_{\mathrm{ice}} = 8\,\mathrm{mm\,w.e.\,d^{-1}K^{-1}}$ (ice melt), $P_{\max} = 60\%$ (firn saturation rate) and $\sigma_{\mathrm{stat}} = 5°\mathrm{C}$ (standard deviation for statistical air-temperature fluctuations) (Reeh, 1991). Further model parameters are listed in Table 1.

3 Results and implications for the DML drillsite

The simulated present state of DML is depicted in Figs. 4-8. First, comparison of the simulated ice surface and thickness (Fig. 4) with their data counterpart (Fig. 2) shows a good agreement for the surface and an excellent agreement for the thickness, for which even many of the fine structures are reproduced very well as a consequence of the high-resolution input data in connection with the refined subgrid in DML. The main test for the model performance, however, is the surface topography, the achieved good agreement being an essential prerequisite for the suitability of this study in terms

Quantity	Value
Gravity acceleration, g	$9.81\,\mathrm{m\,s^{-2}}$
Density of ice, ρ	$910\,\mathrm{kg\,m^{-3}}$
Power-law exponent, n	3
Rate factor, $A(T',\omega)$[1]	Cold ice: Arrhenius law[2]
	Temperate ice: linear dependence on ω^2
Flow-enhancement factor, E	5
Heat conductivity of ice, κ	$9.828\,e^{-0.0057T[\mathrm{K}]}\,\mathrm{W\,m^{-1}K^{-1}}$
Specific heat of ice, c	$(146.3 + 7.253\,T[\mathrm{K}])\,\mathrm{J\,kg^{-1}K^{-1}}$
Latent heat of ice, L	$335\,\mathrm{kJ\,kg^{-1}}$
Clausius-Clapeyron gradient, β	$8.7 \cdot 10^{-4}\,\mathrm{K\,m^{-1}}$
Basal sliding velocity, $\boldsymbol{v}_\mathrm{b}$	Cold base: no-slip
	Temperate base: Weertman-type sliding[2]
Geothermal heat flux, q_geo	$54.6\,\mathrm{mW\,m^{-2}}$
Isostatic time lag, τ_V	3000 a
Asthenosphere density, ρ_a	$3300\,\mathrm{kg\,m^{-3}}$
Density $\times$ specific heat of the lithosphere, $\rho_\mathrm{r}c_\mathrm{r}$	$2000\,\mathrm{kJ\,m^{-3}K^{-1}}$
Heat conductivity of the lithosphere, κ_r	$3\,\mathrm{W\,m^{-1}K^{-1}}$

Table 1: Physical parameters used in the simulations. [1]Homologous temperature T' (relative to pressure melting), water content ω (mass fraction). [2]For details see Greve et al. (1998).

of providing model support for the EPICA DML project. A conspicuous discrepancy between the modelled and the measured ice surface occurs in the north-western part of the region where the 2-km-surface contour shows a large bulge toward the coast which is much less pronounced in the data. Further, the divide area in the south-west is not reproduced completely. Nevertheless, these discrepancies are not so large that they may invalidate our further results.

The gross direction of the ice flux (Fig. 5a), which points exactly down the surface slope due to the applied shallow-ice approximation (Hutter, 1983), is from south-east to north-west (coastward), and the mass flux increases in the same direction. The very pronounced northward drainage basin around 0°E is sustained by the presence of the temperate ice base and, further north, even a basal temperate layer (Fig. 6). Apart from this cold ice prevails in the region, the basal temperatures being typically a few degrees below pressure melting. The occurrence of bands of temperature contours

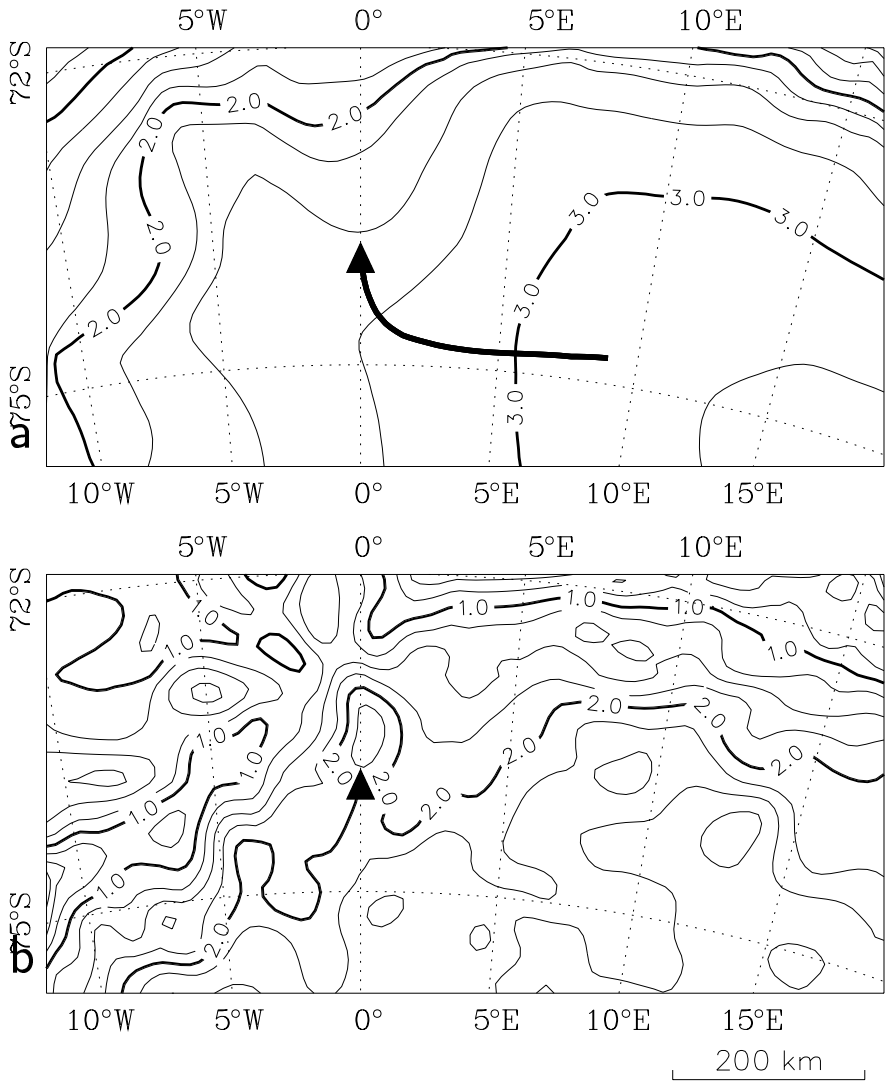

Figure 4: Simulation awi18: Modern surface topography (panel a; in km a.s.l., contour spacing 250 m) and ice thickness (panel b; in km, contour spacing 250 m) in DML. The proposed drill-site is marked by the full triangle, the thick line in panel a indicates the simulated geographical origin of the ice column at the proposed drill-site.

in the plot which run along the grid lines indicates a numerical problem. On the other hand, the solution for the age (see below) which is based on the same type of advection-diffusion-production equation does not show such features, so that the reason for the bands is possibly a combination of a physically real large gradient and a numerical locking of this gradient to the grid lines.

At glacial-maximum conditions (17.7 kyr BP, Fig. 5b), the simulated ice flux shows smaller absolute values due to the lower ice temperatures; however, the general shape of the flow field is the same as for the present. This result is important for the interpretability of any ice core in DML, because strongly varying flow directions in the course of time may induce stratigraphic disturbances such as the observed strongly

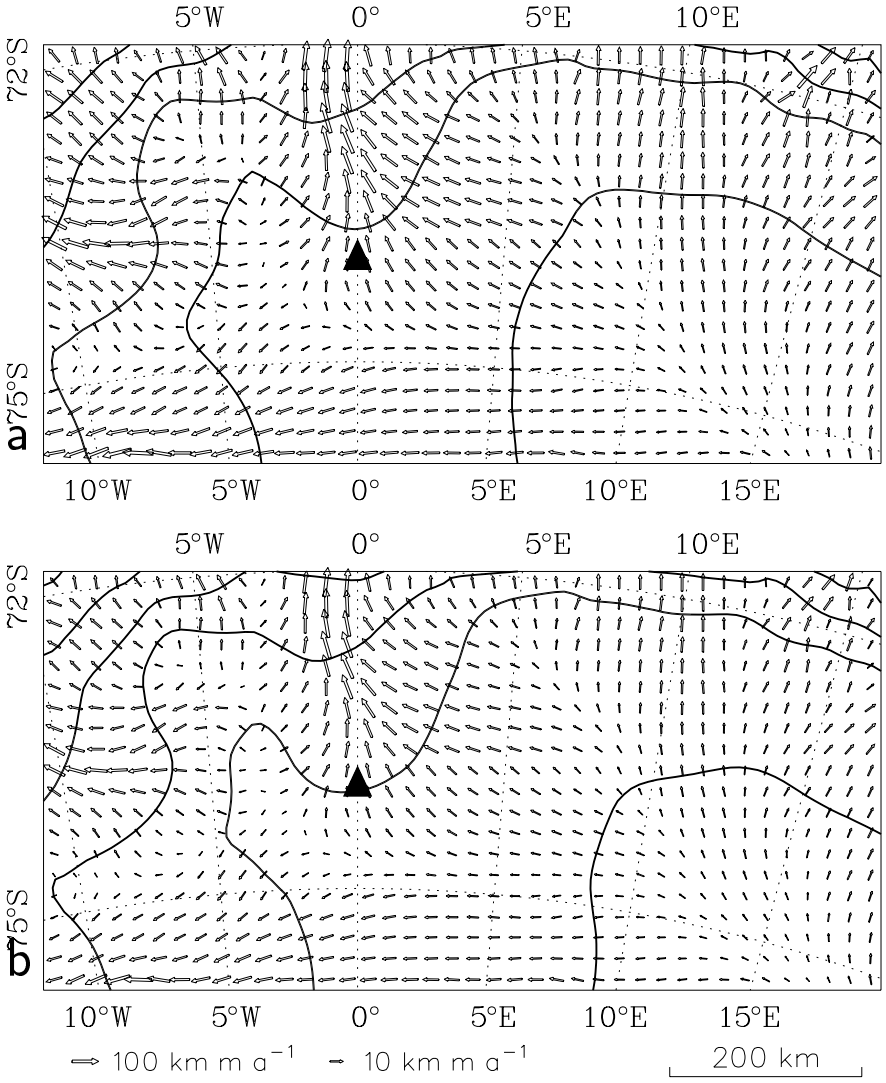

Figure 5: Simulation awi18, mass flux (vertically integrated horizontal velocity) in DML: (a) for modern conditions, (b) at 17.7 kyr BP (Last Glacial Maximum). The proposed drill-site is marked by the full triangle.

inclined layers and overturned folds in the Greenland GRIP and GISP2 cores (Alley et al., 1995; Greve et al., 1999). However, the simulated preservation of the flow-field shape is strongly linked to the assumed spatial constancy of the accumulation pattern through time (section 2.5) which is not guaranteed in reality, so that this result is rather uncertain.

The distribution of the age at 85% depth, which is given in Fig. 7, equally shows a mean gradient toward the north-west, and the older deep ice appears naturally in the inland. Whereas in the south-east the simulated ages at 85% depth are generally larger than 300 ka and thus at least three climatic cycles are covered, close to the coast they are less than 100 ka, so that ice columns in this part of the region do not necessarily reach back to the late Eemian.

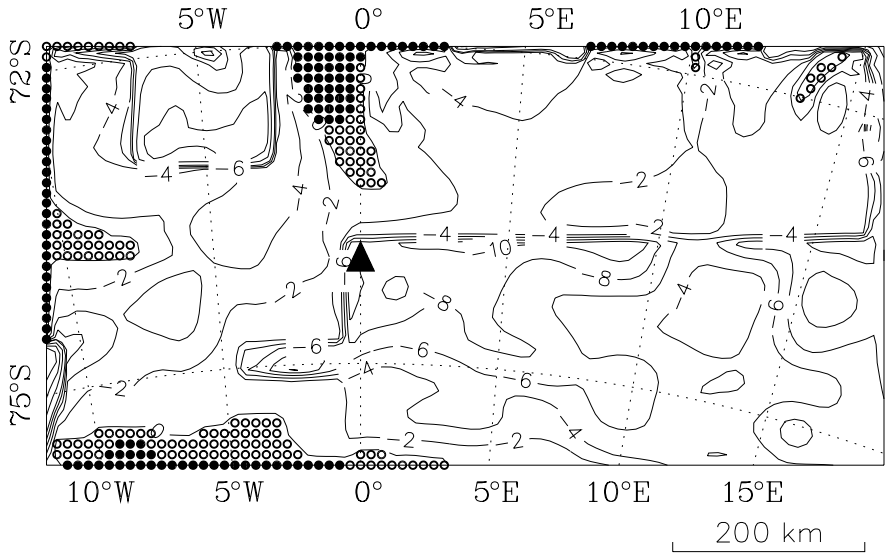

Figure 6: Simulation awi18: Modern basal temperature relative to pressure melting (in °C, contour spacing 2°C) in DML. Open circles (full circles) indicate grid points where the basal ice is at pressure melting without (with) an overlain layer of temperate ice. The proposed drill-site is marked by the full triangle.

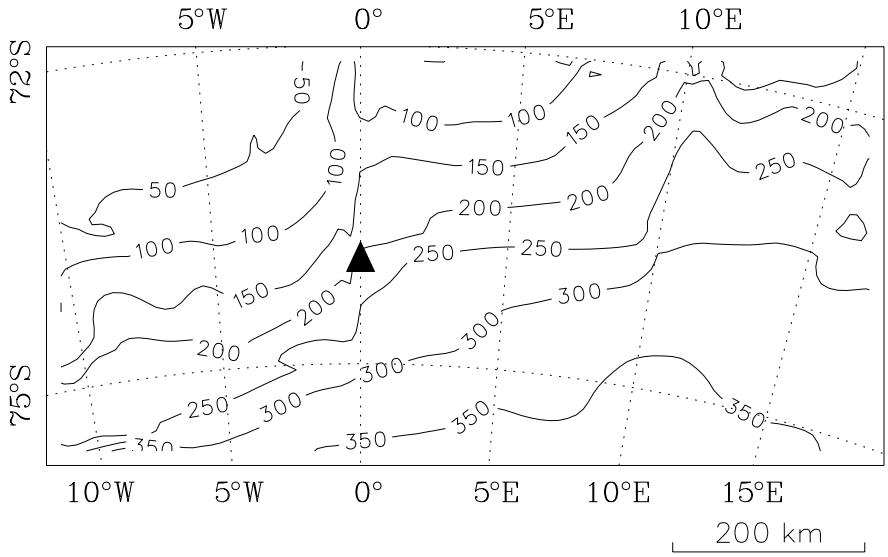

Figure 7: Simulation awi18: Modern age at 85% depth (in ka, contour spacing 50 ka) in DML. The proposed drill-site is marked by the full triangle.

Together with the mass flux, the horizontal shear deformation S_h at the base, defined by

$$S_\mathrm{h} = \left\{ \left(\frac{\partial v_x}{\partial z} \right)^2 + \left(\frac{\partial v_y}{\partial z} \right)^2 \right\}^{1/2} \tag{3.1}$$

(where v_x and v_y are the velocities in x- and y-direction, respectively), increases mainly from the south-east to the north-west, with variations of two orders of magnitude (Fig. 8). However, the fine structure of the ice velocity leads to distinct local variations of the basal shear deformation, so that it can vary by an order of magnitude within some ten kilometers.

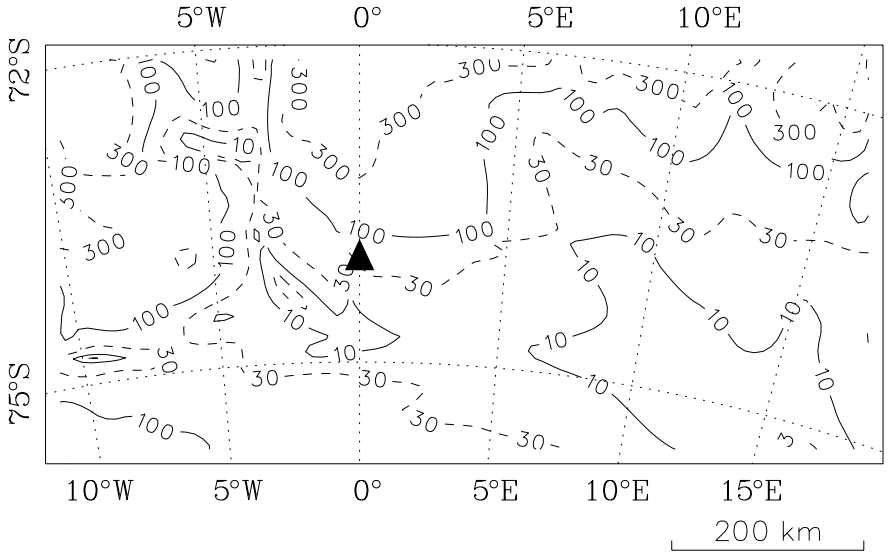

Figure 8: Simulation awi18: Modern basal shear deformation (in $10^{-3}\,\mathrm{a}^{-1}$) in DML. The proposed drill-site is marked by the full triangle.

In agreement with the aims of the EPICA DML core, the accumulation field (Fig. 3) makes it desirable to drill as close to the coast in the north-west as possible [criterion (iii) of the introduction]. However, this is limited by criterion (ii) which requires coverage of an entire glacial/interglacial cycle. According to Fig. 7, this can not be guaranteed in the north-westernmost part of the considered region.

A reasonable compromise for this tradeoff may be the location 73° 59′ S, 00° 00′ E. This position is marked in all of the DML plots, and its main properties are shown in Fig. 9 and Table 2. The accumulation rate is still rather large for Antarctic conditions (12.6 cm ice equiv. a^{-1}), and the age at 85% depth (215.3 ka) is by far large enough to contain the last glacial/interglacial cycle. Further, the basal temperature (−10.9°C) is more than 9°C below pressure melting, which leaves sufficient tolerance to fulfill criterion (i) in the whole ice column even if the local geothermal heat flux is somewhat larger than the 54.6 mW m^{-2} we apply here (Table 1). Also, the shear deformation is

relatively small ($0.047\,\mathrm{a}^{-1}$ at the base, less above) compared to the maximum values within the DML region, so that criterion (iv) is equally met.

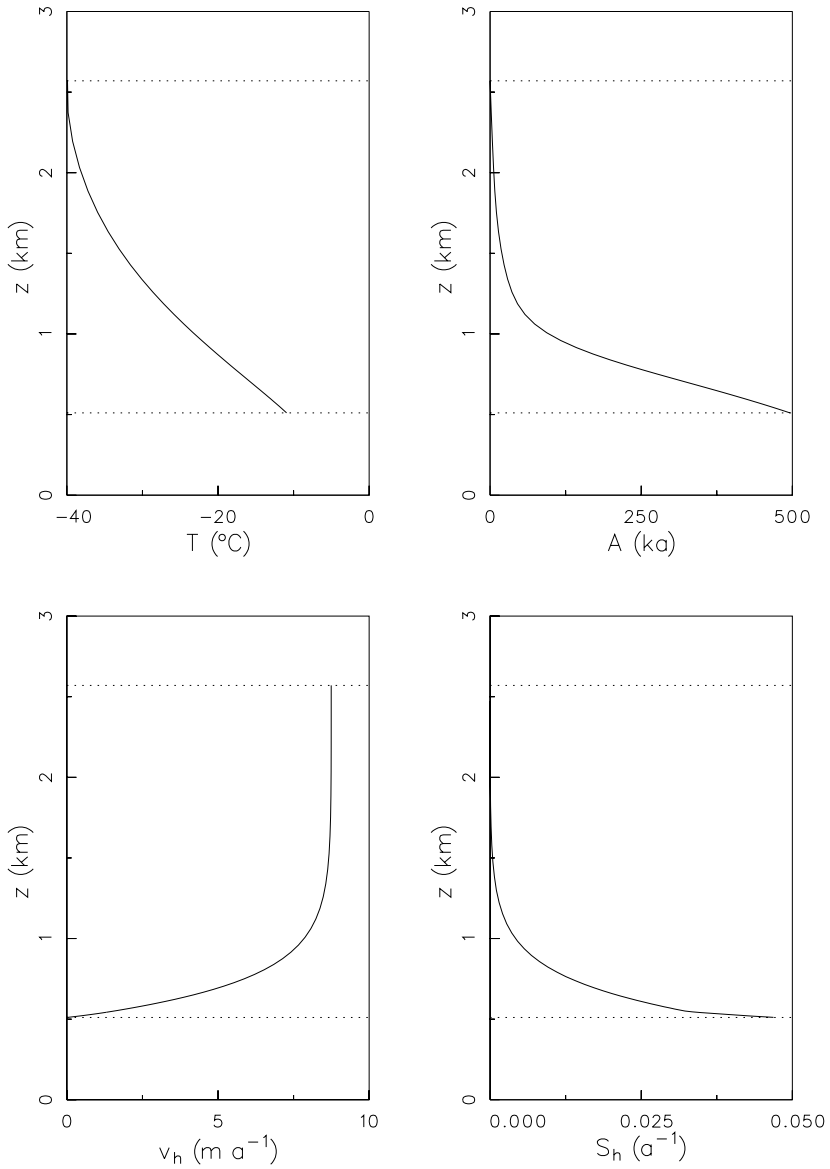

Figure 9: Proposed drill-site in DML at 73° 59′ S, 00° 00′ E. Simulated modern depth profiles of temperature T, age A, horizontal velocity v_h [absolute value $(v_x^2 + v_y^2)^{1/2}$] and shear deformation S_h.

Fig. 4a shows also the geographic origin of the ice in the column at 73° 59′ S, 00° 00′ E. It is computed by tracing the ice particles of the 51 vertical grid points back along the three-dimensional velocity field until they cross the ice surface (Mügge, 1998). To this end, the particle-tracing algorithm is run diagnostically with the SICOPOLIS output for the *present* time slice only, which implies that the evolution of the velocity and topography is neglected. Full coupling between SICOPOLIS and the particle-tracing algorithm with consideration of the time-dependent velocity field has

not yet been implemented, this will be done in the near future. Evidently, the so-calculated ice-origin line extends approximately 320 km upstream, so that the entire 2060 m thick column stems from within the DML domain.

	Simulation	Data
Surface elevation	2570 m a.s.l.	2580 m a.s.l.
Ice thickness	2060 m	2076 m
Accumulation rate	—	12.6 cm ice equiv. a^{-1}
Surface velocity	8.74 m a^{-1}	—
Direction of surface velocity	−8.2° (NNW)	—
Basal temperature	−10.9°C	—
Age at 85% depth	215.3 ka	—
Basal shear deformation	0.047 a^{-1}	—

Table 2: Characteristics of the proposed EPICA DML drill-site at 73° 59′ S, 00° 00′ E.

Compared to the previous drill-site proposal of Calov et al. (1998) (73° 57′ S, 03° 35′ W), the drill-site position we consider here (73° 59′ S, 00° 00′ E) is 109 km further east. The old position still satisfies the four criteria; however, its basal temperature is only −5.7°C (4.8°C below pressure melting), whereas Calov et al. (1998) reported −24.7°C. As the changes of the accumulation input are small, this huge shift is clearly a consequence of the drastically improved knowledge of the basal topography in DML in terms of the gross shape as well as the fine structure, and, directly linked with this, the high numerical resolution which makes efficient use of the fine-structure information. For that reason, the reliability of our new results is distinctly improved.

4 Conclusion and outlook

The present dynamic and thermodynamic state of a 872 × 436 km region in western Dronning Maud Land (DML) was computed as the result of a paleoclimatic simulation through two glacial/interglacial cycles with the 3-d polythermal ice-sheet model SICOPOLIS. For DML, recent high-resolution radio-echo sounding ice-thickness data were implemented, and a nested model was applied with a grid spacing of 10.9 km. The computed maps of basal temperature, age and shear deformation together with the accumulation distribution from interpolated field data contain important information for the process of determining a suitable drill-site for the EPICA DML ice core, the major objective of which is to obtain a high-resolution climate archive for the last glacial/interglacial cycle. Main results are:

- The accumulation rate increases from south-east to north-west (toward the coast), which supports a near-coastal location for the EPICA DML core.
- The near-basal age decreases in the same direction, so that locations too close to the coast do not cover the entire last glacial/interglacial cycle.
- Except for a temperate tongue in the north and some minor scattered temperate patches, the basal ice in DML is below pressure melting.
- The shear deformation varies by two orders of magnitude in DML with a general coastward increase.

Based on these results, a drill-site location at 73° 59′ S, 00° 00′ E seems favorable. However, the optimum position for the EPICA DML core cannot be determined by ice-sheet modelling alone; considerations on the atmospheric circulation (Atlantic origin) and the chemistry (interpretability of ice-core parameters) must equally be included (Jouzel et al., 1994). Ongoing studies of the accumulation distribution in the area and the inclusion of an improved surface-topography dataset (Bamber, 1994; Bamber and Huybrechts, 1996) which shows more fine structure than the classical Drewry (1983) data used here will also result in more refined boundary values. Nevertheless, the results of this study represent a sound basis for further discussion.

Acknowledgements

We thank M. B. Giovinetto (University of Calgary) for providing the accumulation dataset of the Antarctic ice sheet, and H. Miller and D. Steinhage (Alfred-Wegener-Institut für Polar- und Meeresforschung, Bremerhaven) for providing the radio-echo-sounding ice-thickness data of Dronning Maud Land. The comments of A. J. Payne and an anonymous referee have helped to improve the quality of this paper.

This work is a contribution to the "European Project for Ice Coring in Antarctica" (EPICA), a joint ESF/EC scientific programme, funded by the European Commission under the Environment and Climte Programme (1994-1998) contract ENV4-CT95-0074 and by national contributions from Belgium, Denmark, France, Germany, Italy, the Netherlands, Norway, Sweden, Switzerland and the United Kingdom. The support of this work by the Deutsche Forschungsgemeinschaft under project no. Hu 412/19-3 is gratefully acknowledged.

Waxing and waning of the perennial north polar H_2O ice cap of Mars over obliquity cycles

Ralf Greve

Institut für Mechanik, Technische Universität Darmstadt, D-64289 Darmstadt, Germany

Abstract

The perennial north polar H_2O ice cap of Mars is investigated with the dynamic/thermodynamic ice-sheet model SICOPOLIS. Computational results for flow velocities, ice temperatures and surface accumulation/ablation rates are presented for the steady state with present conditions as well as for transient scenarios over idealized obliquity cycles with periods of 1.3 Myr and 125 kyr. The transient simulations lead to a stop-and-go-type dynamics with a cold and almost stagnant modern ice cap and a warmer flowing ice cap for past large-obliquity periods. The most likely scenario for the present ice cap comprises an ice volume of 1.2 million km^3, a maximum thickness of 3 km, the absence of pronounced local isostasy, H_2O-ice accumulation rates of the order of tenth mm water equivalent (w.e.) per earth year (yr), flow velocities of the order of mm/yr and an ice base far below pressure melting.

1 Introduction

In each winter season, the northern and southern polar regions of Mars become frosted equator-wards until beyond the 55th parallel. This seasonal cover consists of frozen CO_2 (dry ice), which forms from atmospheric CO_2 in the low polar winter temperatures of about 145 K (Forget, 1998). This process, which therefore has two maxima during the Martian year, absorbs up to one third of the entire atmosphere, leading to distinct seasonal variations of the air pressure. However, the southern winter pressure minimum is more pronounced than the northern winter counterpart. This is so because the eccentricity of the Martian orbit around the sun is relatively large ($e_{\mathrm{Mars}} = 0.093$, compared to $e_{\mathrm{Earth}} = 0.017$), the perihelion being reached during the southern summer (like on Earth), and as a consequence the contrast between summer and winter is larger in the southern hemisphere than in the northern hemisphere.

During the respective summer, the largest part of the dry ice sublimates back into the atmosphere; however, a certain residual cap always survives. In the north polar

region, this perennial ice consists of a H_2O ice cap within approximately 80°N (Kieffer et al., 1976), whereas in the south at least the cover of the smaller residual ice within 85°S is CO_2 (Kieffer, 1979; Paige et al., 1990). It is not clear whether this CO_2 cover is underlain by a H_2O ice cap like in the north.

Elevation data from the Mars Orbiter Laser Altimeter (MOLA) of the Mars Global Surveyor (MGS) space probe suggest that the present volume of the perennial north polar H_2O ice cap, the objective of this study, is approximately $1.2 \cdot 10^6\,\mathrm{km}^3$ (Zuber et al., 1998), which corresponds to a 7.5 m thick planetwide water layer. It therefore represents an important reservoir for the water cycle of the Martian atmosphere. Large amounts of water may further occur as permafrost layers in the regolith as a remnant of former liquid surface water (Fanale et al., 1992); however, a direct proof for their existence is still due.

Previous simulations by Greve (1998), still based on the topography by Dzurisin and Blasius (1975), have shown that the time the north polar cap requires to reach the dynamic and thermodynamic steady state is larger than the main obliquity cycles of approximately 125 kyr and 1.3 Myr (Kieffer and Zent, 1992). As changes in obliquity likely force climatic changes, the ice cap is quite probably not close to a steady state with the present conditions. MacAyeal (pers. comm., 1998) has forwarded the idea that the ice cap shows a stop-and-go-type dynamics, that is, essentially stagnant in cold periods with little accumulation (like now) and flowing in warmer periods with increased accumulation. Provided the obliquity cycles are the main reason for these variations, the ice cap may consequently suffer quasi-periodic oscillations with the above periods. This study pursues this idea by modelling the evolution of an idealized axisymmetric ice cap subjected to periodically varying accumulation, surface temperature, extent and thickness.

2 Model description

The present perennial north polar H_2O ice cap of Mars is investigated with the dynamic/thermodynamic ice-sheet model SICOPOLIS (SImulation COde for POLythermal Ice Sheets), which was originally developed for and applied to terrestrial ice sheets like Greenland, Antarctica and the glacial northern hemisphere (Greve, 1997b,c; Calov et al., 1998; Greve et al., 1998, 1999). The model is based on the continuum-mechanical theory of polythermal ice masses (Hutter, 1982, 1993; Greve, 1997a), which describes the material ice as a density-preserving, heat-conducting, power-law fluid with thermo-mechanical coupling due to the strong temperature dependence of the ice viscosity:

$$\boldsymbol{D} = EA(T')\sigma^{n-1}\,\boldsymbol{t}^{\mathrm{D}}, \tag{2.1}$$

where $\boldsymbol{D} = \mathrm{sym\,grad}\,\boldsymbol{v}$ (velocity $\boldsymbol{v}$) is the strain-rate tensor, $\boldsymbol{t}^{\mathrm{D}}$ the stress deviator, $\sigma = [\mathrm{tr}\,(\boldsymbol{t}^{\mathrm{D}})^2/2]^{1/2}$ the effective shear stress, n the power-law exponent, $A(T')$ the flow-rate factor [which depends exponentially on the temperature T' relative to pressure melting, see Greve et al. (1998)], and E the flow-enhancement factor which is equal to one for pure ice and can deviate from one due to the softening or stiffening effect of impurities in the ice. It is further distinguished between *cold ice* with a temperature below the pressure melting point and *temperate ice* with a temperature at the pressure melting point, the latter being considered as a binary mixture of ice and small amounts of water. The interface that separates cold and temperate ice is monitored through the use of Stefan-type energy flux and mass flux matching conditions (Greve, 1997a).

The model computes three-dimensionally the temporal evolution of ice extent, thickness, velocity, temperature, water content and age as a response to external forcing. The last must be specified by (i) the mean annual air temperature above the ice, (ii) the surface mass balance, which is ice accumulation (snowfall, condensation) minus ablation (melting, evaporation, erosion), (iii) the global sea level (not relevant for Martian applications) and (iv) the mantle (geothermal) heat flux from below, imposed 5 km below the ice-bedrock interface in order to account for thermal inertia effects of the lithosphere. For the simulations discussed in this study, however, instead of specifying the surface mass balance and computing the resulting topography evolution, the topography evolution is prescribed, and the surface mass balance is computed such that it is consistent with the changing topography and the ice velocity field. This inverse approach is chosen because the MOLA data already mentioned above have provided a very precise present topography of the north polar cap and an indication of its former extent (Zuber et al., 1998), whereas for present and past accumulation/ablation rates no direct measurements are available. Isostatic depression and rebound of the lithosphere due to changing ice loads is either ignored, or it is described by a local balance between ice weight and buoyancy force on the lithosphere, the viscosity of the asthenosphere being then included by a delayed (time lag τ_{V}) adjustment of the system (LeMeur and Huybrechts, 1996).

3 Simulation set-up

3.1 Present topography and climate

The surface topography, h, of the north polar region of Mars, which consists of the perennial H_2O ice cap surrounded by the lowlands of Vastitas Borealis, is now known very precisely from laser altimetry (MOLA) measurements of the MGS spacecraft (Zuber et al., 1998). These data show that earlier stereogrammetric reconstructions based on Mariner 9 images (Dzurisin and Blasius, 1975) overestimated the extent

and thickness of the ice cap distinctly. The region consists of a broad, 5-km-deep topographic depression with a 3-km-thick ice cap at the north pole, the total ice volume, V_{tot}, and the ice-covered basal area, $A_{\mathrm{i,b}}$ being estimated as $1.2 \times 10^6\,\mathrm{km}^3$ and $10^6\,\mathrm{km}^2$, respectively. The volume estimate assumes the absence of local lithospheric isostasy. In the presence of Earth-like local isostasy and therefore downward flexure of the subglacial bedrock, b, with respect to the relaxed bedrock, b_0, a more appropriate value is $V_{\mathrm{tot}} = 1.7 \times 10^6\,\mathrm{km}^3$ (Zuber et al., 1998).

For this study, a simplified surface and bedrock topography is constructed based on the MOLA data. The relaxed bedrock is described as a parabolic bowl with elevation $b_0^{90\mathrm{N}} = -5\,\mathrm{km}$ at the north pole (90°N) and $b_0^{30\mathrm{N}} = -2\,\mathrm{km}$ at 30°N:

$$b_0(r) = b_0^{90\mathrm{N}} + (b_0^{30\mathrm{N}} - b_0^{90\mathrm{N}}) \frac{r^2}{R_{\mathrm{b}}^2}, \tag{3.1}$$

where r is the distance from the pole, and $R_{\mathrm{b}} = 3556.28\,\mathrm{km}$ is the distance from 90°N to 30°N, based on the mean equatorial Martian radius $R_{\mathrm{M}} = 3396\,\mathrm{km}$.

For the ice thickness above the relaxed bedrock, $H^\star$, a similar paraboloid-like representation is used:

$$H^\star(r) = H_{\mathrm{i}}^0 \left(1 - \left(\frac{r}{R_{\mathrm{i}}^0} \right)^m \right), \quad \text{for } r < R_{\mathrm{i}}^0, \tag{3.2}$$

with the maximum ice thickness $H_{\mathrm{i}}^0 = 3\,\mathrm{km}$, the ice extent $R_{\mathrm{i}}^0 = 564.19\,\mathrm{km}$ and the exponent $m = 4/3$. These parameters yield an ice volume of $1.2 \times 10^6\,\mathrm{km}^3$ and an ice-covered area of $10^6\,\mathrm{km}^2$, which coincides exactly to the above MOLA estimates. The surface topography of the ice cap follows from eqs. (3.1), (3.2) and $h = b_0 + H^\star$, and is depicted in Fig. 1 as a contour plot and in Fig. 2 as a transect. Fig. 2 shows also that the deviation of the bedrock representation (3.1) from a flat bed is very small compared to the ice-cap thickness, so that the influence of the bowl-shaped bedrock on computed results will be essentially negligible.

In the absence of isostasy, the actual bedrock below the ice, b, is identical to the relaxed bedrock, b_0, and $H^\star$ is consequently equal to the total ice thickness $H = h - b$. However, for the case of local isostasy (balance between ice load and lithosphere buoyancy), the actual bedrock below the ice, b, is related to the relaxed bedrock by

$$b = b_0 - \frac{\rho}{\rho_{\mathrm{a}}} H, \quad \text{or} \quad b = \frac{\rho_{\mathrm{a}} b_0 - \rho h}{\rho_{\mathrm{a}} - \rho}, \tag{3.3}$$

with the ice density $\rho = 910\,\mathrm{kg/m}^3$ and the mantle density $\rho_{\mathrm{a}} = 3300\,\mathrm{kg/m}^3$.

The mean annual air temperature above the ice, T_{ma}, is described by a parameterization depending on elevation, h, and co-latitude, $\tilde{\phi}$ ($\tilde{\phi} = 90°\mathrm{N} - \phi$, where ϕ is the latitude),

$$T_{\mathrm{ma}} = T_{\mathrm{ma}}^0 + \gamma_{\mathrm{ma}}\, h + c_{\mathrm{ma}}\, \tilde{\phi}, \tag{3.4}$$

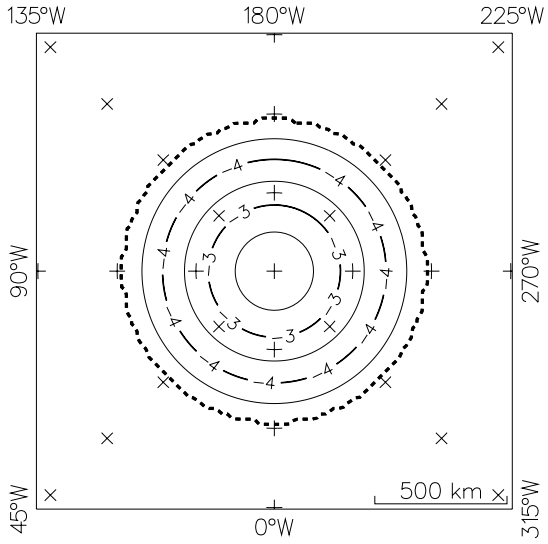

Figure 1: Surface topography (elevation contours, in km above reference surface) of the north polar region of Mars as defined by eqs. (3.1), (3.2) and $h = b_0 + H^\star$. The dashed heavy line indicates the ice margin, latitude marks are spaced by 5°.

with $T^0_{\rm ma} = -105$°C, the mean lapse rate $\gamma_{\rm ma} = -2.5$°C/km, and $c_{\rm ma} = 1.5$°C/°lat. This is a modification of the purely elevation-dependent parameterization derived by Budd et al. (1986) from Viking surface-temperature measurements of a part of the ice cap (Kieffer et al., 1977), separated for the true elevation dependence with the mean lapse rate in the free lower troposphere (value −2.5°C/km by Kondratyev and Hunt, 1982), and the remaining latitudinal dependence. In analogy to well-established parameterizations for the terrestrial ice sheets of Greenland and Antarctica (Reeh, 1991; Huybrechts, 1993), the latter is taken linear in $\tilde{\phi}$. The parameters $T^0_{\rm ma}$ and $c_{\rm ma}$ are chosen such that the parameterized temperatures of Budd et al. (1986) at the pole (−100°C) and at 80°N (zonal average of −77.5°C) fall together with the temperatures of parameterization (3.4).

3.2 Past topography and climate

In order to conduct transient simulations starting at some point in the past it is required to complement the specifications of section 3.1 with information about the past topography and climatic conditions. Following the idea of a stop-and-go behaviour (cf. section 1), we assume that the ice extent, thickness and surface temperature vary sinusoidally over the obliquity cycles, with periods $t_{\rm obl}$ of either 125 kyr (main obliquity variation) or 1.3 Myr (first modulation), and minimum values in the present. This is justified as a first approximation by the fact that the obliquity variations themselves are essentially harmonic in time at least during the last few million years (Ward, 1979); however, due to the impact of nonlinearities also different response pat-

terns of the Martian climate system to this astronomic forcing, up to discontinuous behaviour, are possible. In order to investigate this in a physically adequate fashion, coupled dynamic atmosphere/ice-cap simulations would be required.

For the ice thickness above the relaxed bedrock, the harmonic approach yields

$$H^\star(r,t) = H_\mathrm{i}(t)\left(1 - \left(\frac{r}{R_\mathrm{i}(t)}\right)^m\right), \quad \text{for } r < R_\mathrm{i}(t), \tag{3.5}$$

with the ice extent

$$R_\mathrm{i}(t) = \frac{R_\mathrm{i}^0 + R_\mathrm{i}^\mathrm{max}}{2} - \frac{R_\mathrm{i}^\mathrm{max} - R_\mathrm{i}^0}{2}\cos\left(\frac{2\pi t}{t_\mathrm{obl}}\right) \tag{3.6}$$

and, analogously, the maximum thickness

$$H_\mathrm{i}(t) = \frac{H_\mathrm{i}^0 + H_\mathrm{i}^\mathrm{max}}{2} - \frac{H_\mathrm{i}^\mathrm{max} - H_\mathrm{i}^0}{2}\cos\left(\frac{2\pi t}{t_\mathrm{obl}}\right), \tag{3.7}$$

where $R_\mathrm{i}^\mathrm{max} = 889.07\,\mathrm{km}$ and $H_\mathrm{i}^\mathrm{max} = 4.728\,\mathrm{km}$. These values satisfy the condition $R_\mathrm{i}^\mathrm{max}/R_\mathrm{i}^0 = H_\mathrm{i}^\mathrm{max}/H_\mathrm{i}^0$, so that the shape and aspect ratio of the ice cap are the same at all times. The choice of $R_\mathrm{i}^\mathrm{max}$ corresponds to a maximum southward extent to 75°N. This is motivated by the existence of a ring of outliers of the present ice cap approximately at this latitude, interpreted by Zuber et al. (1998) as a remnant of the former ice extent.

Similarly, the surface temperature (3.4) is modified by an additional sinosoidal variation ΔT_ma,

$$\Delta T_\mathrm{ma}(t) = \frac{\Delta T_\mathrm{ma}^\mathrm{max}}{2}\left(1 - \cos\left(\frac{2\pi t}{t_\mathrm{obl}}\right)\right), \tag{3.8}$$

with an assumed maximum of $\Delta T_\mathrm{ma}^\mathrm{max} = 30°\mathrm{C}$ for periods of large obliquity. This value represents the temperature variation of the surface regolith at 90° latitude modelled by Fanale et al. (1982) for an obliquity variation of 25°. Following Ward (1979), obliquity variations of this magnitude characterize the last ten million years. However, more recent simulations of the orbital elements of Mars indicate the possibility of variations of as large as 50° during that period (Bills, 1990), so that $\Delta T_\mathrm{ma}^\mathrm{max} = 30°\mathrm{C}$ can be regarded as a lower limit for the associated temperature variations.

3.3 Simulation series

Three types of simulations will be discussed in the following: (i) a steady-state simulation for present conditions *(mf001)* integrated for 1 Myr in order to reach the thermal equilibrium, (ii) transient paleo-simulations until the present over five obliquity cycles with the long period $t_\mathrm{obl} = 1.3\,\mathrm{Myr}$ *(mt006, mt007)*, and (iii) transient paleo-simulations until the present over ten obliquity cycles with the short period $t_\mathrm{obl} = 125\,\mathrm{kyr}$ *(mt008, mt009)*. For simulations mf001, mt006 and mt008 isostasy is

ignored (rigid lithosphere, $b = b_0$), for simulations mt007 and mt009 local isostasy with a time lag $\tau_V = 3\,\mathrm{kyr}$ due to the asthenosphere viscosity is applied (LeMeur and Huybrechts, 1996). Discussion of the transient runs is focussed on the respective last simulated cycle, for which the influence of the initial condition has faded. This is so because the previous simulation time exceeds the time scale $[t]$ for the ice-cap response to changing climate conditions,

$$[t] = \frac{[H]^2}{\kappa/(\rho c)} \approx 130\,\mathrm{kyr} \tag{3.9}$$

(where $[H] = 3\,\mathrm{km}$ is the scale for the ice thickness, κ and c are the heat conductivity and the specific heat of ice, respectively, computed according to Table 1 with a typical ice temperature of $-75°\mathrm{C}$, and $\kappa/(\rho c)$ is the thermal diffusivity of ice), by far.

For all cases, the present topography serves as initial condition. The model domain consists of a $1800\,\mathrm{km} \times 1800\,\mathrm{km}$ square in polar stereographic projection, centered at the pole (Fig. 1). Horizontal resolution is 20 km, vertical resolution is 51 grid points in the cold-ice column, 11 grid points in the temperate-ice column (if existing) and 11 grid points in the lithosphere column. Two different time steps Δt and $\widetilde{\Delta t}$ apply for the integration of the mechanic and thermodynamic evolution equations, respectively (Greve, 1997b). For type (i), $\Delta t = 1\,\mathrm{kyr}$ and $\widetilde{\Delta t} = 10\,\mathrm{kyr}$, for types (ii) and (iii), $\Delta t = 100\,\mathrm{yr}$ and $\widetilde{\Delta t} = 1\,\mathrm{kyr}$.

The ice mechanics, eq. (2.1), is described by standard values for the terrestrial Greenland ice sheet, $n = 3$ and $E = 3$. This includes the influence of small amounts of fine dust, ca. 1 mg/kg with particle sizes of 0.1 to 2 μm as it was measured in the Wisconsin-ice-age part of the ice core Dye 3 in south Greenland (Hammer et al., 1985); this makes the ice more readily deformable than ideally pure ice with $E = 1$ (Paterson, 1991). However, if major parts of the ice volume were contaminated significantly with dust, the mixture of deformable ice and essentially rigid dust would be even stiffer than pure ice. Durham (1998) reports that a dust content of 10% reduces the strain rate by 20%, which would correspond to $E = 1/1.2 = 0.833$ and therefore reduce the flow velocities computed in this study by a factor $3/0.833 = 3.6$.

At the ice-bedrock interface, no-slip conditions are adopted independent of the basal temperature. For the geothermal heat flux, the value $q_{\mathrm{geo}} = 35\ \mathrm{mW/m^2}$ is applied as standard (Budd et al., 1986; Schubert et al., 1992), this is about 2/3 of the average geothermal heat flux on Earth. Simulations *mt010, mt011, mt012, mt013* are re-runs of mt006 with strongly increased heat fluxes of 70, 80, 90 and 100 $\mathrm{mW/m^2}$ in order to investigate under which conditions basal melting can be reached. However, as these heat fluxes are outside the range estimated by Schubert et al. (1992), these scenarios are probably unrealistic.

A complete list of the physical parameters used for the simulations is given in Table 1.

Quantity	Value
Gravity acceleration, g	$3.72\,\mathrm{m\,s^{-2}}$
Density of ice, ρ	$910\,\mathrm{kg\,m^{-3}}$
Power-law exponent, n	3
Flow-enhancement factor, E	3
Heat conductivity of ice, κ	$9.828\,e^{-0.0057\,T[\mathrm{K}]}\,\mathrm{W\,m^{-1}K^{-1}}$
Specific heat of ice, c	$(146.3 + 7.253\,T[\mathrm{K}])\,\mathrm{J\,kg^{-1}K^{-1}}$
Latent heat of ice, L	$335\,\mathrm{kJ\,kg^{-1}}$
Clausius-Clapeyron gradient, β	$3.3 \cdot 10^{-4}\,\mathrm{K\,m^{-1}}$
Geothermal heat flux, q_{areo}	$35\,\mathrm{mW\,m^{-2}}$
Time lag for lithosphere adjustment, τ_{V}	3000 yr
Mantle density, ρ_{a}	$3300\,\mathrm{kg\,m^{-3}}$
Density $\times$ specific heat of the lithosphere, $\rho_{\mathrm{r}} c_{\mathrm{r}}$	$2000\,\mathrm{kJ\,m^{-3}K^{-1}}$
Heat conductivity of the lithosphere, κ_{r}	$3\,\mathrm{W\,m^{-1}K^{-1}}$

Table 1: Physical parameters used in the simulations.

4 Results and discussion

4.1 Steady-state simulation

The result of the present steady state computed in simulation mf001 is depicted in Figs. 2, 3. The flow field shows the downward and outward pattern which is typical for land-based ice sheets, with very small maximum velocities of 0.5 mm/yr. As a consequence of the relatively flat near-margin parts which follow from eq. (3.2), these regions are almost stagnant. The temperature field is controlled entirely by heat conduction, which leads to the very regular temperature increase with depth. This is in sharp contrast with the behaviour of terrestrial ice sheets where the temperature field is mainly controlled by advection, so that the isotherms are densified near the bedrock and even have inversions in the upper regions [e.g., Greve (1997b)]. Nowhere in the ice body are temperatures significantly higher than $-70°\mathrm{C}$ relative to pressure melting reached. The accumulation rate required to maintain the prescribed shape in the steady state is of the order of merely 0.01 mm w.e./yr (w.e.: water equivalent) in the central accumulation region. Further downstream the surface mass balance becomes slightly negative, so that ablation prevails.

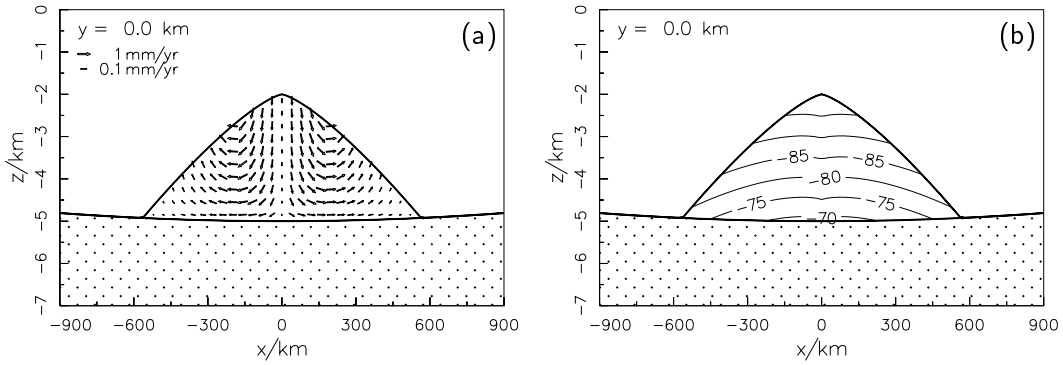

Figure 2: Simulation mf001 (present steady state, no isostasy): Transect across the north pole. (a) Velocity. (b) Temperature (relative to pressure melting, in °C).

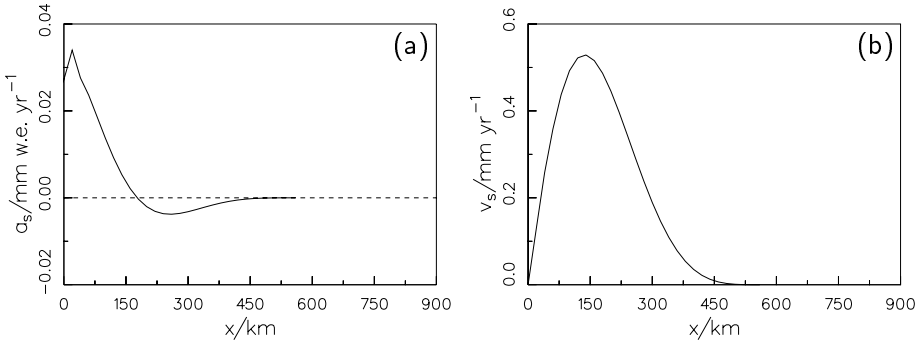

Figure 3: Simulation mf001 (present steady state, no isostasy): (a) Accumulation/ablation rate a_s, (b) surface velocity v_s along the flowline 270°W from the pole ($x = 0$) to the ice margin.

4.2 Transient simulations

Figs. 4-6 show results for the transient simulation mt006 (1.3 Myr obliquity cycle, no isostasy). In Fig. 4 the flow and temperature fields are compared for $t = -650$ kyr (650 kyr before present, 1/2 of the cycle, maximum ice volume and surface temperature) and $t = 0$ (modern, end of the cycle, minimum ice volume and surface temperature). The modern ice cap still remembers the higher temperatures of the past (basal temperatures reach −55°C), and the flow velocities are consequently an order of magnitude larger than in the steady state (up to 3 mm/yr). The simulated ancient ice cap at $t = -650$ kyr is distinctly warmer with maximum basal temperatures of −38°C, and the flow velocities now exceed 300 mm/yr, two orders of magnitude more than for the modern ice cap. Therefore, the scenario of simulation mt006 provides indeed a significant stop-and-go-type dynamics of the ice cap.

The accumulation/ablation rates at 1/4, 1/2, 3/4 and the end (present) of the cycle are depicted in Fig. 5. The maximum volume increase at 1/4 of the cycle is characterized by an overall positive mass balance with accumulation rates around

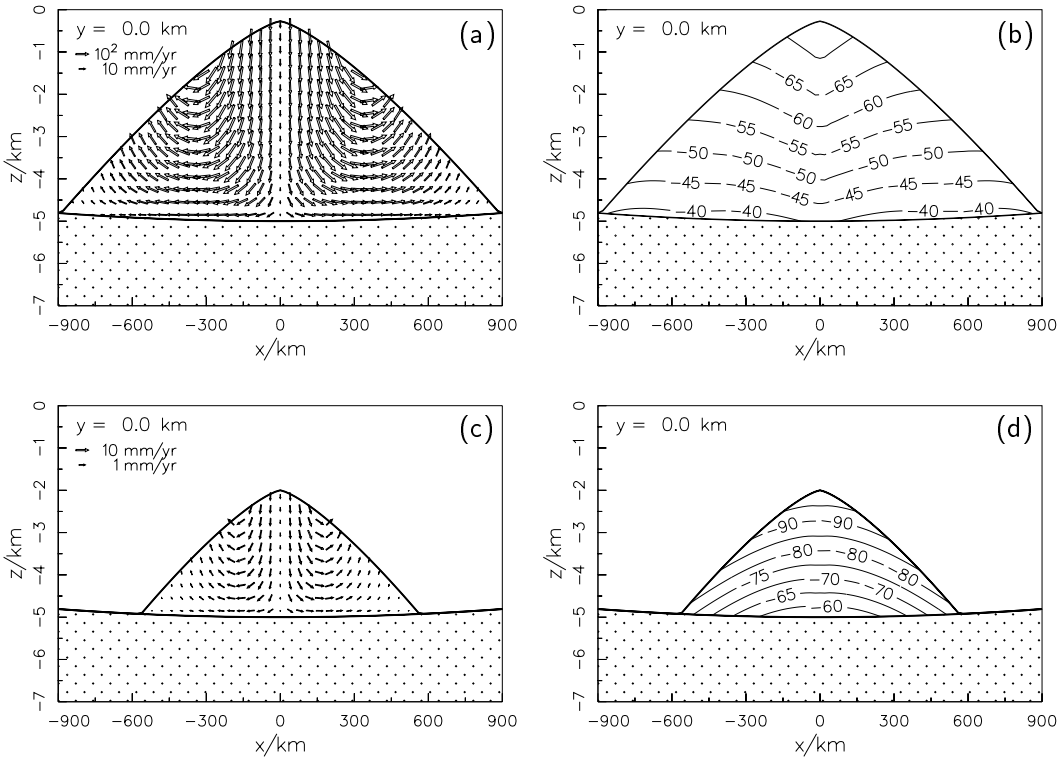

Figure 4: Simulation mt006 (1.3 Myr obliquity cycle, no isostasy): Transect across the north pole. (a, b) Velocity and temperature (relative to pressure melting, in °C) at $t = -650$ kyr (after 1/2 of the cycle). (c, d) Same, at $t = 0$ (today, at the end of the cycle).

5 mm w.e./yr. At 1/2 of the cycle, the volume maximum is reached, for which accumulation rates of up to 15 mm w.e./yr are required in the interior, whereas in the outer regions of the ice cap the mass balance is slightly negative. At 3/4 of the cycle, the time of maximum volume decrease, naturally ablation is predominant except for the very interior, and typical ablation rates are 5 mm w.e./yr, to which evaporation, melting and erosional processes can contribute. The modern, almost stagnant ice cap consists of an inner accumulation zone with maximum values of 0.2 mm w.e./yr and an outer zone with ablation rates of up to 0.05 mm w.e./yr. Although very small, this is an order of magnitude larger than for the present steady state of simulation mf001.

The surface velocities for these four times are plotted in Fig. 6. The shape is similar in all cases: the zero velocity at the ice dome (north pole) increases to a maximum at approximately 1/3 of the distance to the ice margin, from where it begins to decrease again toward the margin. As a consequence of the low exponent $m = 4/3$ in the thickness function (3.5), surface gradients are moderate and the ice flow therefore very small close to the margin. The evolution of surface velocity with time reveals again the pronounced stop-and-go behaviour, with velocities between the above mentioned extremes at the transitional times of 1/4 and 3/4 of the cycle.

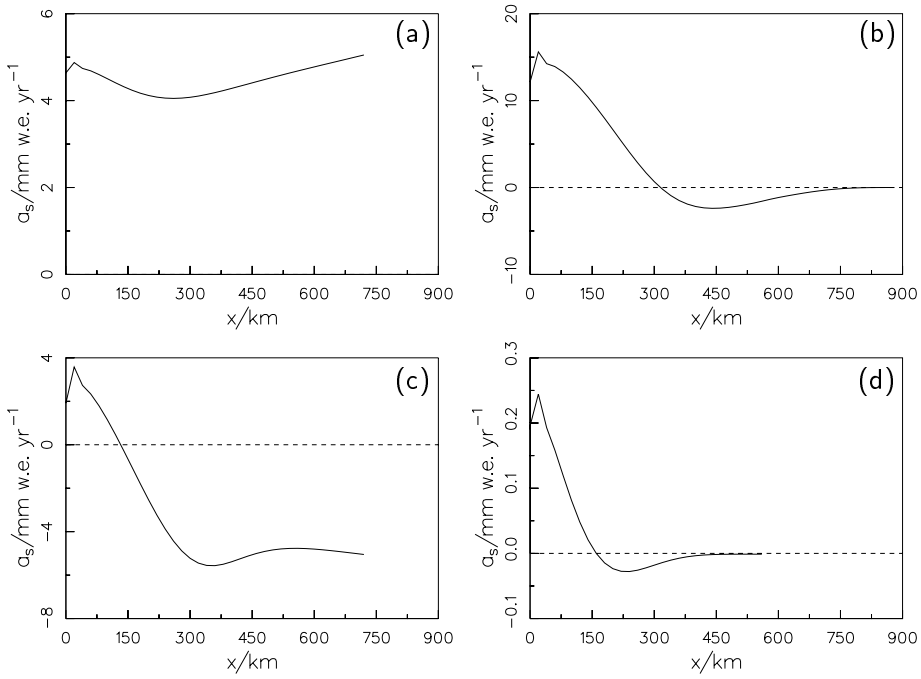

Figure 5: Simulation mt006 (1.3 Myr obliquity cycle, no isostasy): Accumulation/ablation rate a_s along the flowline 270°W from the pole ($x = 0$) to the ice margin. (a) $t = -975$ kyr (after 1/4 of the cycle). (b) $t = -650$ kyr (after 1/2 of the cycle). (c) $t = -325$ kyr (after 3/4 of the cycle). (d) $t = 0$ (today, at the end of the cycle). Note the different scales of the ordinate axes.

The corresponding results of simulation mt007 (1.3 Myr obliquity cycle, local isostasy) are presented in Figs. 7-9. The effect of isostasy is to increase the ice thickness by approximately one third [eq. (3.3)], which results in larger driving stresses and increased temperatures. Due to the nonlinearity of the flow law (2.1), this has a pronounced effect on the flow velocities and the required accumulation/ablation rates, which are an order of magnitude larger than for simulation mt006. Ice temperatures are still well below pressure melting; even in the large ancient ice cap of Fig. 7b the basal temperatures do not exceed −30°C.

In Figs. 10, 11 the accumulation/ablation profiles for simulations mt008 (125 kyr obliquity cycle, no isostasy) and mt009 (125 kyr obliquity cycle, local isostasy) are shown. Evidently, the accumulation is extremely large (at least for Martian conditions) for the time $t = -93.8$ kyr (1/4 of the cycle), the ablation for $t = -31.2$ kyr (3/4 of the cycle). This is easy to understand as these are the times with maximum ice volume increase and decrease, respectively, and the rate of volume change is ten times larger than for simulations mt006, mt007 because of the ten times shorter periodicity. For both simulations mt008 and mt009, the accumulation rate after 1/4 and the ablation rate after 3/4 of the cycle reach values of 50 mm w.e./yr; the former value exceeds modern terrestrial accumulation rates in central east Antarctica (Giovinetto

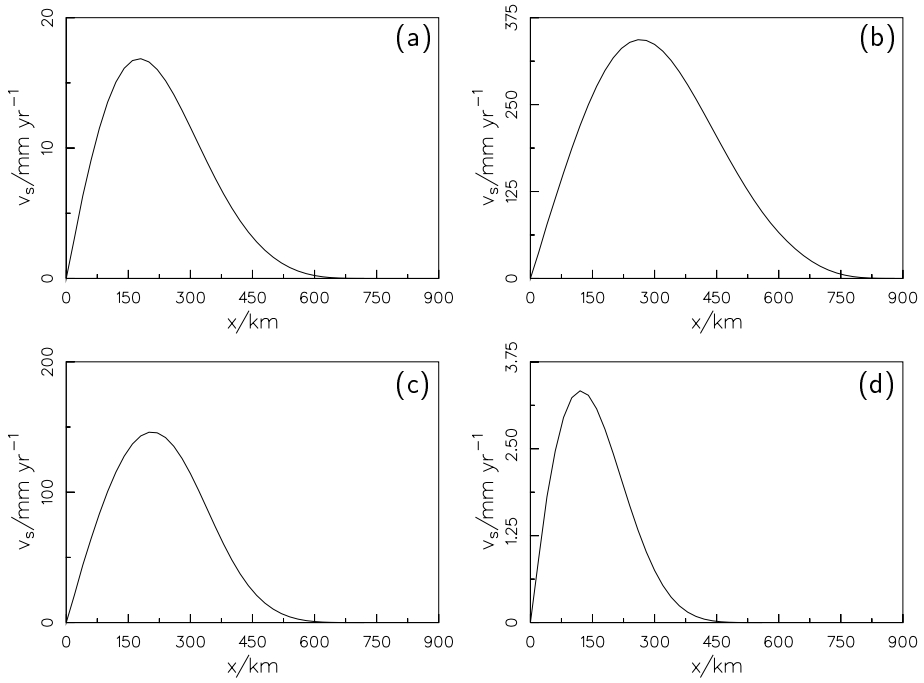

Figure 6: Simulation mt006 (1.3 Myr obliquity cycle, no isostasy): Surface velocity v_s along the flowline 270°W from the pole ($x = 0$) to the ice margin. (a) $t = -975$ kyr (after 1/4 of the cycle). (b) $t = -650$ kyr (after 1/2 of the cycle). (c) $t = -325$ kyr (after 3/4 of the cycle). (d) $t = 0$ (today, at the end of the cycle). Note the different scales of the ordinate axes.

and Bentley, 1985), and it may be doubted whether even a somewhat warmer and moistier Martian climate then today's can sustain so much accumulation over 10's of kyears. Apparently, the 125 kyr cycle is too short to provide major ice volume changes as they are considered here.

An independent simple estimate of modern Martian H_2O accumulation rates can be obtained as follows: The mean water-vapour abundance in the Martian atmosphere is of the order of 10 precipitable micrometers as compared to some precipitable centimeters on Earth (Jakosky and Haberle, 1992), hence three to four orders of magnitude less. Compared to the mean accumulation rate of 300 mm w.e./yr for the terrestrial Greenland ice sheet (Ohmura and Reeh, 1991), this yields the order of 0.1 mm w.e./yr under present Martian conditions. Evidently, simulation mt006 provides the best agreement with this value (Fig. 5), and it is therefore regarded as the most realistic scenario.

However, this conclusion must be taken with great care. Based on the shortage of craters in the north polar layered terrain (which is essentially identical to the ice cap), Cutts et al. (1976) estimated an accumulation rate of 1 mm/yr. On the other hand, Kieffer (1990) pointed out that its value should be limited by 3.7×10^{-2} mm/yr as a consequence of the mean water-vapour abundance in the atmosphere

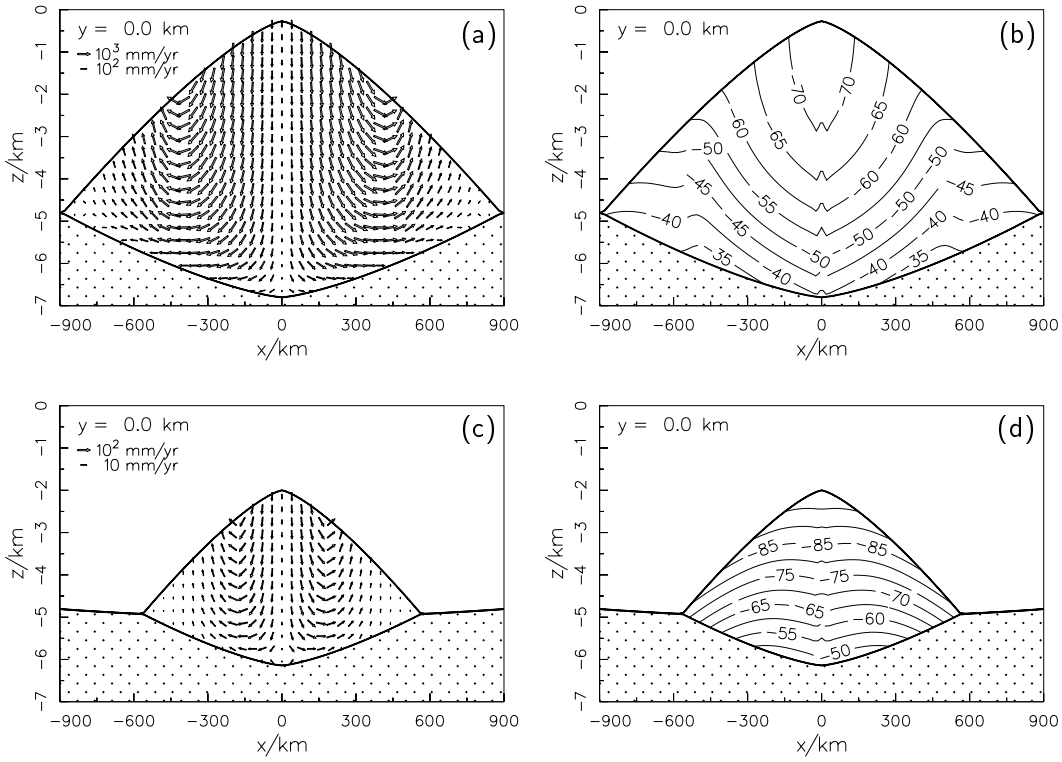

Figure 7: Simulation mt007 (1.3 Myr obliquity cycle, local isostasy): Transect across the north pole. (a, b) Velocity and temperature (relative to pressure melting, in °C) at $t = -650$ kyr (after 1/2 of the cycle). (c, d) Same, at $t = 0$ (today, at the end of the cycle).

and the amount of CO_2 frost deposited in the ice cap. By using Viking surface-temperature measurements, Haberle and Jakosky (1990) computed the amount of water sublimed from the north polar cap into the atmosphere during the summer season as 0.1 to 0.8 mm/yr, and they stated further that due to uncertain atmospheric transport processes even the sign of the annual budget is uncertain [see also the review articles by Jakosky and Haberle (1992), Kieffer and Zent (1992), Thomas et al. (1992)]. Therefore, Thomas et al. (1992) concluded that "The present water ice and dust budgets at either pole are not known in either sign or magnitude. Reasonable estimates vary by nearly 2 orders of magnitude", and a final decision which simulation is in best agreement with atmospheric conditions cannot be made.

In a more recent study by Jakosky et al. (1993), the Martian water cycle was investigated for the last ten million years of climatic history. The authors pointed out that the amount of water sublimed from the north polar cap into the atmosphere during the summer season (essentially equal to the annual ablation rate) is mainly controlled by obliquity, whereas the other orbital parameters, eccentricity and L_s of perihelion, are of less, but still significant, importance. Over the whole range of obliquities during the past ten million years, the calculated annual ablation rates

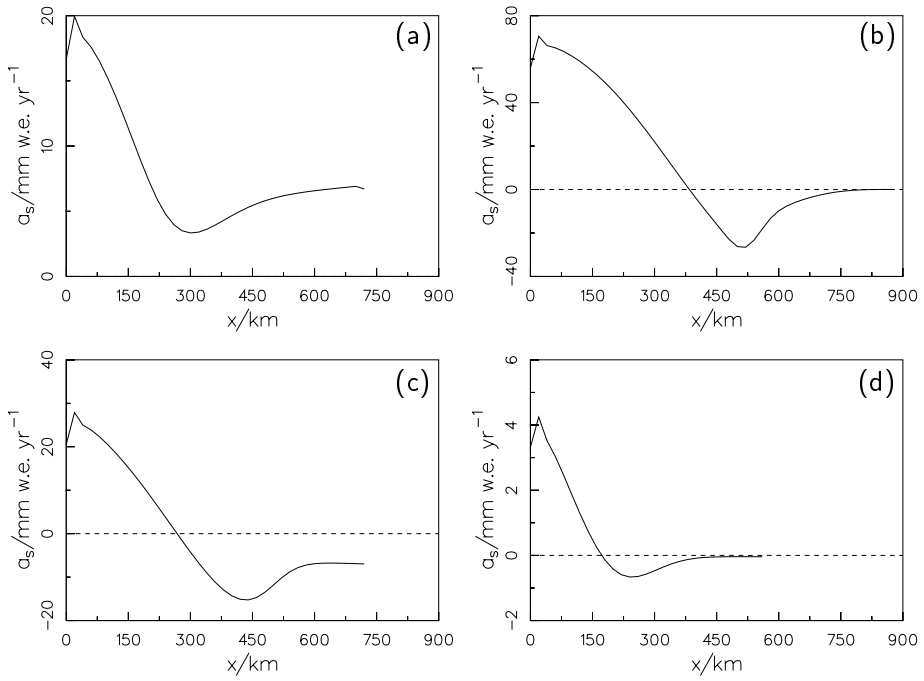

Figure 8: Simulation mt007 (1.3 Myr obliquity cycle, local isostasy): Accumulation/ablation rate a_s along the flowline 270°W from the pole ($x = 0$) to the ice margin. (a) $t = -975$ kyr (after 1/4 of the cycle). (b) $t = -650$ kyr (after 1/2 of the cycle). (c) $t = -325$ kyr (after 3/4 of the cycle). (d) $t = 0$ (today, at the end of the cycle). Note the different scales of the ordinate axes.

vary by four orders of magnitude, from some 10^{-3} mm/yr to some 10 mm/yr. It is difficult to compare these values with the findings of the present study as here only net accumulation/ablation rates are obtained, but at least it can be stated that the absolute values of the accumulation/ablation rates of simulations mf001 and mt006 are well within this range, whereas those of simulations mt007, mt008 and mt009 require some 10 mm/yr of positive as well as of negative net accumulation/ablation rates at some time during the respective obliquity cycle, and are thus at the upper limit (Figs. 3, 5, 8, 10, 11).

However, this comparison is only reasonable under the assumption that annual accumulation and ablation rates are of the same order of magnitude. This requires that the Martian atmospheric circulation is capable of transporting the required amounts of water into the north polar region in order to resupply the summertime loss, which is largely unclear due to uncertainties in the understanding of present and, even more pronounced, past atmospheric circulation processes (Jakosky et al., 1993). Therefore, a conclusive statement on how far the results of this study are consistent with atmospheric physics is not possible, even though no obvious inconsistencies occur.

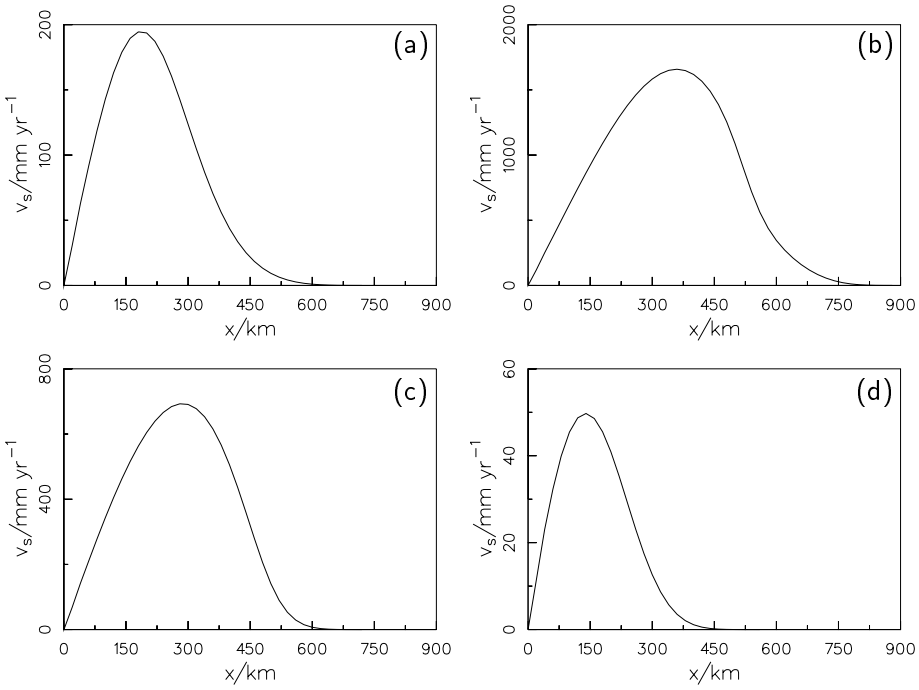

Figure 9: Simulation mt007 (1.3 Myr obliquity cycle, local isostasy): Surface velocity v_s along the flowline 270°W from the pole ($x = 0$) to the ice margin. (a) $t = -975$ kyr (after 1/4 of the cycle). (b) $t = -650$ kyr (after 1/2 of the cycle). (c) $t = -325$ kyr (after 3/4 of the cycle). (d) $t = 0$ (today, at the end of the cycle). Note the different scales of the ordinate axes.

4.3 Variation of the geothermal heat flux

In none of the simulations discussed above does the basal temperature reach or come close to the pressure melting point. However, these results are strongly dependent on the applied geothermal heat flux, $q_{\mathrm{geo}} = 35\,\mathrm{mW/m^2}$, which is not well-constrained (Schubert et al., 1992). In order to investigate under which circumstances pressure melting can be reached at the ice base, simulation mt006 is re-run with increased q_{geo}'s of 70, 80, 90, 100 $\mathrm{mW/m^2}$ (simulations mt010, mt011, mt012, mt013). The first simulation in which pressure melting at the ice base is reached at some time in the 1.3 Myr cycle is mt012 ($90\,\mathrm{mW/m^2}$), namely from $t = -644$ kyr to $t = -376$ kyr, with a maximum basal area at pressure melting of $A_{\mathrm{t,b}} = 0.463 \cdot 10^6\,\mathrm{km^2}$ at $t = -542$ kyr. For simulation mt013 ($100\,\mathrm{mW/m^2}$), basal areas at pressure melting occur from $t = -742$ kyr to $t = -302$ kyr, the maximum, $A_{\mathrm{t,b}} = 0.505 \cdot 10^6\,\mathrm{km^2}$, is reached at $t = -550$ kyr. Evidently, the maxima are phase-shifted by 100 kyr with respect to the surface temperature, which reaches its maximum at $t = -650$ kyr [eq. (3.8)].

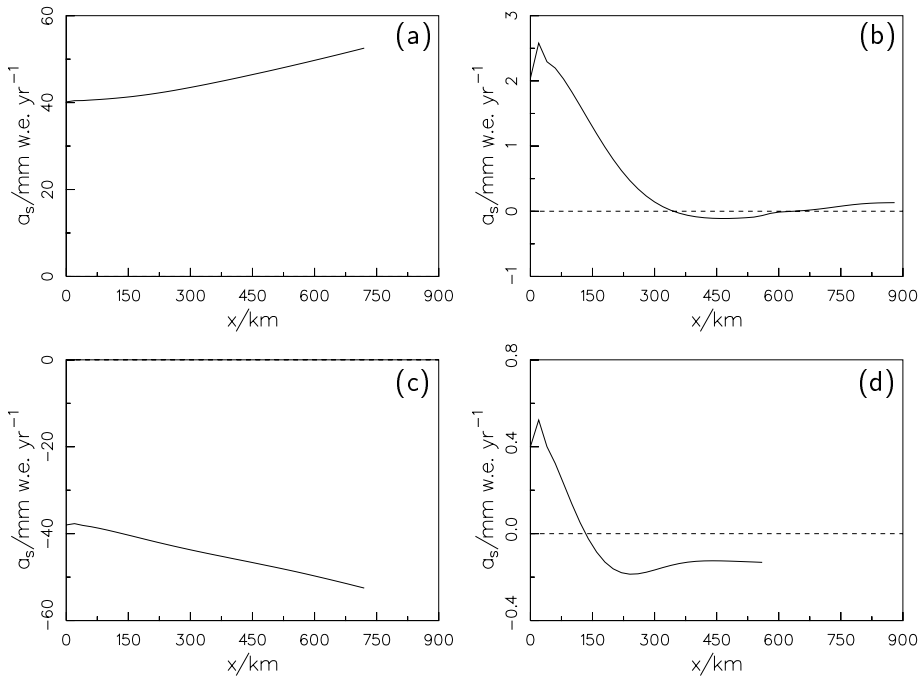

Figure 10: Simulation mt008 (125 kyr obliquity cycle, no isostasy): Accumulation/ablation rate a_s along the flowline 270°W from the pole ($x = 0$) to the ice margin. (a) $t = -93.8$ kyr (after 1/4 of the cycle). (b) $t = -62.5$ kyr (after 1/2 of the cycle). (c) $t = -31.2$ kyr (after 3/4 of the cycle). (d) $t = 0$ (today, at the end of the cycle). Note the different scales of the ordinate axes.

Fig. 12 shows the basal temperature from the pole to the ice margin for simulation mt013 (100 mW/m^2) and four different times during the 1.3 Myr cycle. The regions of pressure melting after 1/2 (maximum surface temperature and ice volume) and 3/4 (maximum decrease rate of surface temperature and ice volume) of the cycle are situated between approximately 2/3 and 3/4 of the distance from the pole to the respective ice margin, followed by almost stagnant and very cold marginal regions. However, even for this extreme scenario with un unrealistically large value for q_{geo} the simulated present ice cap does not reach pressure melting at any point, the maximum basal temperature is still more than 10°C below. It is therefore very unlikely that at the base of the present north polar ice cap pressure-melting conditions occur because of the too small ice volume.

4.4 Sources of uncertainty

The ice velocities and accumulation/ablation rates computed in this study are subject to some uncertainty due to the poorly-constrained physical parameters of the ice mechanics and thermodynamics (Table 1) in the Martian north polar cap mainly associated with the unknown dust content. As it was already discussed in section 3.3,

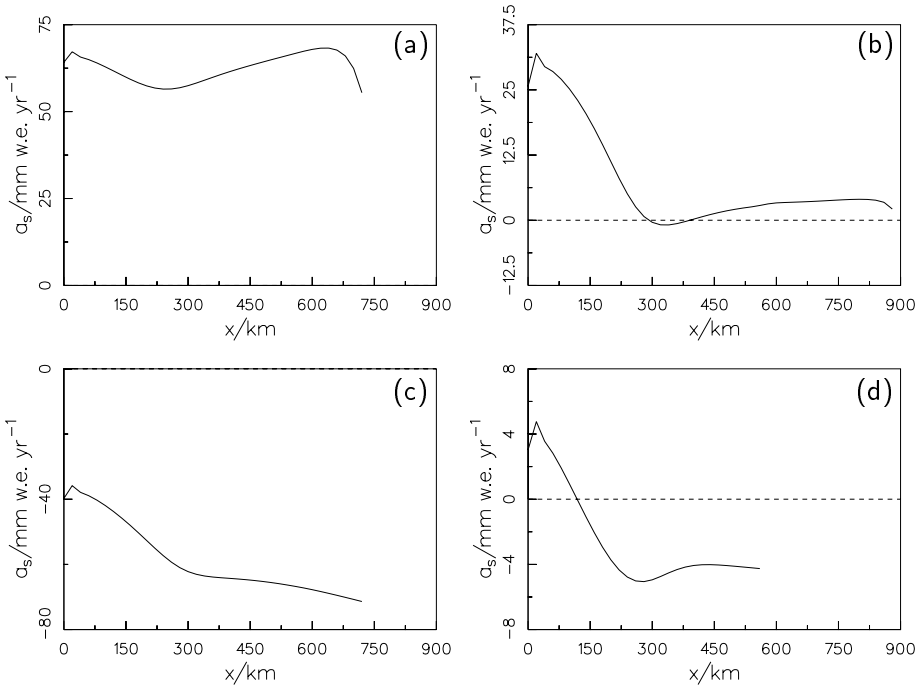

Figure 11: Simulation mt009 (125 kyr obliquity cycle, local isostasy): Accumulation/ablation rate a_s along the flowline 270°W from the pole ($x = 0$) to the ice margin. (a) $t = -93.8$ kyr (after 1/4 of the cycle). (b) $t = -62.5$ kyr (after 1/2 of the cycle). (c) $t = -31.2$ kyr (after 3/4 of the cycle). (d) $t = 0$ (today, at the end of the cycle). Note the different scales of the ordinate axes.

the flow-enhancement factor E may be even smaller than one if major parts of the ice body contain significant amounts of dust; a mean dust content of, for instance, 10% would reduce the computed ice velocities and accumulation/ablation rates by 3.6 according to Durham (1998). However, the effect of increased density counteracts this reduction: 10% of dust with a true density of three times the density of pure ice yields a 20% density increase of the ice-dust mixture, and therefore a 20% increase of the driving stresses. Due to the flow law (2.1), the strain rates, velocities and accumulation/ablation rates rise by $1.2^n \approx 1.73$ for $n = 3$, so that the combined reduction resulting from the reduced enhancement factor and the increased density is $3.6/1.73 \approx 2.1$. As this study targets at providing orders of magnitude rather than exact values for the ice flow, this uncertainty is not severe.

The evidence for the power-law exponent $n = 3$ stems from numerous laboratory tests and ice-deformation measurements in the field, and this value is therefore widely used in terrestrial glacier and ice-sheet modelling (Paterson, 1994). However, there is no direct proof for its validity at the very low temperatures of the Martian ice caps. A larger (smaller) value of n would increase (decrease) the difference between the "stop" phase and the "go" phase of the north polar cap because the non-linearity in the flow law (2.1) would be more (less) pronounced than for $n = 3$; however, this is secondary

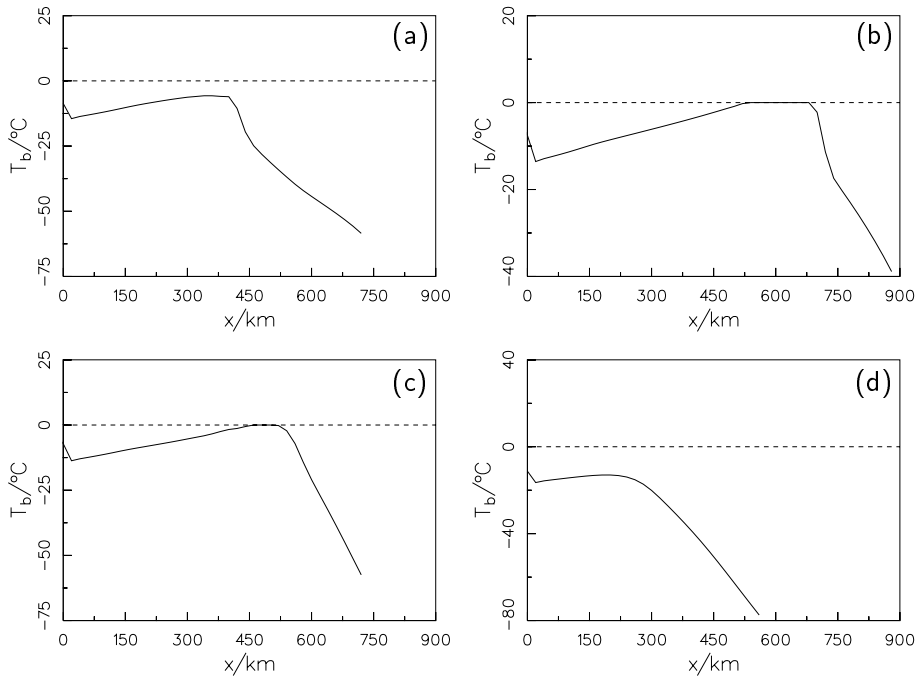

Figure 12: Simulation mt013 ($q_{\mathrm{geo}} = 100\,\mathrm{mW/m^2}$, 1.3 Myr obliquity cycle, no isostasy): Basal temperature T_{b} (relative to pressure melting) along a flowline from the pole ($x = 0$) to the ice margin. (a) $t = -975\,\mathrm{kyr}$ (after 1/4 of the cycle). (b) $t = -650\,\mathrm{kyr}$ (after 1/2 of the cycle). (c) $t = -325\,\mathrm{kyr}$ (after 3/4 of the cycle). (d) $t = 0$ (today, at the end of the cycle). Note the different scales of the ordinate axes.

compared to the overriding importance of temperature variations for the ice flow due to the climatic cycles (Durham, 1998).

Finally, the question of isostasy is still open. The MOLA data by Zuber et al. (1998) show no evidence, such as moats and forebulges of the surrounding terrain, for the occurence of local isostasy due to the ice load. This agrees with the above finding that the scenario without isostasy provides apparently the most realistic ice flow and associated accumulation/ablation rates. For the results of the simulations with local isostasy (mt007, mt009), the exact value of the assumed time lag τ_{V} (here 3000 yr) is unimportant as long as it remains much smaller than $t_{\mathrm{obl}}/2$, which is the time scale for significant changes of the ice load. This is sufficiently fulfilled for the 1.3 Myr cycle if $\tau_{\mathrm{V}} < 100\,\mathrm{kyr}$ and for the 125 kyr cycle if $\tau_{\mathrm{V}} < 10\,\mathrm{kyr}$, in this case an essentially instantaneous isostatic response results for the simulated ice/lithosphere/asthenosphere system.

5 Conclusion

The findings of this study suggest that the large-scale dynamics and thermodynamics of the north polar H_2O ice cap of Mars can be described in a similar way to that of

terrestrial ice sheets, which are mainly controlled by the surface mass balance and the temperature-dependent glacier flow. By imposing sinusoidal variations in ice volume and surface temperature due to periodic obliquity variations, one obtains a stop-and-go-type behaviour through time, the present ice cap being in the "stop" phase characterized by low temperatures, flow velocities and accumulation rates. It is very unlikely that the temperature of any part of the present ice cap reaches the pressure melting point.

Due to the conceptional paraboloid-like topography used here and the lack of precise data for the ice composition, bedrock topography, accumulation rate, surface temperature and mantle heat flux, however, the presented results are merely of a semi-quantitative nature. Further, smaller-scale effects like the occurrence of distinct troughs in the ice surface and the spatially varying dust content (layers) are not yet treated.

A promising direction for future work which avoids prescribing the surface temperature and either the topography or the mass balance at the ice/atmosphere interface is coupling the ice-sheet model with a general circulation model (GCM) of the Martian atmosphere (Pollack et al., 1990; Hourdin et al., 1993, 1995). This might entail transient simulations of the dynamics and thermodynamics of the Martian atmosphere and ice caps directly driven by the changes in the orbital elements.

Acknowledgements

The author wishes to thank K. Herkenhoff and B. M. Jakosky whose reviews helped considerably to improve the quality of this paper.

Common list of references

Abe-Ouchi, A. 1993. Ice sheet response to climatic changes: a modelling approach. *Zürcher Geogr. Schr.*, **54**, 134 pp.

Albrecht, O. 1999. Dynamics of glaciers and ice sheets: a numerical model study. Ph. D. thesis in preparation, Geographisches Institut, Eidgenössische Technische Hochschule Zürich, Switzerland.

Alley, R. B., A. J. Gow, S. J. Johnsen, J. Kipfstuhl, D. A. Meese and T. Thorsteinsson. 1995. Comparison of deep ice cores. *Nature*, **373**, 393-394.

Baral, D. R. 1999. Asymptotic theories of large-scale motion, temperature and moisture distributions in land-based polythermal ice shields and in floating ice shelves – A critical review and new developments. Ph. D. thesis, Institut für Mechanik, Technische Universität Darmstadt, Germany.

Barenblatt, G. I. 1987. *Dimensional analysis*. Gordon and Breach Science Publ., New York etc.

Bauer, G. 1997. Thermodynamische Betrachtung einer gesättigten Mischung. Ph. D. thesis, Institut für Mechanik, Technische Hochschule Darmstadt, Germany, 126 pp.

Becker, E. and W. Bürger. 1975. *Kontinuumsmechanik*. B. G. Teubner, Stuttgart.

Bills, B. G. 1990. The rigid body obliquity history of Mars. *J. Geophys. Res.*, **95**, 14137-14153.

Blatter, H. 1991. Effect of climate on the cryosphere. *Zürcher Geogr. Schr.*, **41**, 98 pp.

Blatter, H. 1995. Velocity and stress fields in grounded glaciers: a simple algorithm for including deviatoric stress gradients. *J. Glaciol.*, **41** (138), 333-344.

Blatter, H. and K. Hutter. 1991. Polythermal conditions in arctic glaciers. *J. Glaciol.*, **37** (126), 261-269.

Bloom, A. L., W. S. Broecker, J. M. A. Chappell, R. K. Mathews and K. J. Mesolella. 1974. Quaternary sea level fluctuations on a tectonic coast: new ^{230}Th/^{234}U dates from the Huon Peninsula, New Guinea. *Quaternary Research*, **4**, 185-205.

Bolzan, J. F. and M. Strobel. 1994. Accumulation-rate variations around Summit, Greenland. *J. Glaciol.*, **40** (134), 56-66.

Braithwaite, R. J. 1995. Positive degree-day factors for ablation on the Greenland ice sheet studied by energy-balance modelling. *J. Glaciol.*, **41** (137), 153-160.

Braithwaite, R. J. and O. B. Olesen. 1989. Calculation of glacier ablation from air temperature, West Greenland. In: *Glacier fluctuations and climatic change*, J. Oerlemans (ed.), Kluwer, 219-233.

British Antarctic Survey. 1993. Antarctica – a topographic database. *Sheet BAS (Misc)*, **7**, edition 1.

Budd, W. F., B. Coutts and R. C. Warner. 1998. Modelling the Antarctic and Northern Hemisphere ice sheet changes with global climate through the glacial cycle. *Ann. Glaciol.*, **27**, 153-160.

Budd, W. F., D. Jenssen, J. H. I. Leach, I. N. Smith and U. Radok. 1986. The north polar ice cap of Mars as a steady-state system. *Polarforschung*, **56** (1/2), 43-46.

Budd, W. F. and I. N. Smith. 1979. The growth and retreat of ice sheets in response to orbital radiation changes. *Sea level, ice, and climatic change* (Proceedings of the Canberra Symposium, December 1979), IAHS Publ. **131**.

Budd, W. F. and I. N. Smith. 1982. Large-scale numerical modelling of the Antarctic ice sheet. *Ann. Glaciol.*, **3**, 42-49.

Calov, R. 1994. Das thermomechanische Verhalten des grönländischen Eisschildes unter der Wirkung verschiedener Klimaszenarien – Antworten eines theoretisch-numerischen Modells. Ph. D. thesis, Institut für Mechanik, Technische Hochschule Darmstadt, Germany, 171 pp.

Calov, R. and K. Hutter. 1996. The thermomechanical response of the Greenland ice sheet to various climate scenarios. *Climate Dynamics*, **12**, 243-260.

Calov, R. and K. Hutter. 1997. Large scale motion and temperature distributions in land based ice shields – the Greenland Ice Sheet in response to various climatic scenarios. *Arch. Mech.*, **49**, 919-962.

Calov, R. and I. Marsiat. 1998. Simulations of the northern hemisphere through the last glacial-interglacial cycle with a vertically integrated and a 3-d thermomechanical ice sheet model coupled to a climate model. *Ann. Glaciol.*, **27**, 169-176.

Calov, R., A. Savvin, R. Greve, I. Hansen and K. Hutter. 1998. Simulation of the Antarctic ice sheet with a three-dimensional polythermal ice-sheet model, in support of the EPICA project. *Ann. Glaciol.*, **27**, 201-206.

Chappell, J. and N. J. Shackleton. 1986. Oxygen isotopes and sea level. *Nature*, **324** (6093), 137-140.

Chen, J. H., H. A. Curran, B. White and G. J. Wasserburg. 1991. Precise chronology of the last interglacial period: ^{234}U-^{230}Th data from fossil coral reefs in the Bahamas. *Geological Society of America Bulletin*, **103**, 82-97.

Clarke, G. K. C., U. Nitsan and W. S. B. Paterson. 1977. Strain heating and creep instability in glaciers and ice sheets. *Rev. Geophys. Space Phys.*, **15** (2), 235-247.

Clausen, H. B., W. Dansgaard and J. O. Nielsen. 1979. Surface accumulation on Ross Ice Shelf. *Antarctic Journal U.S.*, **14** (5), 68-72.

Crowley, T. J. 1994. Potential reconciliation of Devil's Hole and deep-sea Pleistocene chronologies. *Palaeoceanography*, **91**, 1-5.

Crowley, T. J. and K. Y. Kim. 1994. Milankovitch forcing of the Last Interglacial sea level. *Science*, **265**, 1566-1567.

Cuffey, K. M., G. D. Clow, R. B. Alley, M. Stuiver, E. D. Waddington and R. W. Saltus. 1995. Large Arctic temperature change at the Wisconsin-Holocene glacial transition. *Science*, **270**, 455-458.

Cutler, N. N., C. F. Raymond, E. D. Waddington, D. A. Meese and R. B. Alley. 1995. The effect of ice-sheet thickness change on the accumulation history inferred from GISP2 layer thicknesses. *Ann. Glaciol.*, **21**, 26-32.

Cutts, J. A., K. R. Blasius, G. A. Briggs, M. H. Carr, R. Greeley and H. Masursky. 1976. North polar region of Mars: Imaging results from Viking 2. *Science*, **194**, 1329-1337.

Dahl-Jensen, D., S. J. Johnsen, C. U. Hammer, H. B. Clausen and J. Jouzel. 1993. Past accumulation rates derived from observed annual layers in the GRIP ice core from Summit, Central Greenland. *Ice in the Climate System*, W. R. Peltier (ed.), Springer-Verlag Berlin etc., 517-532.

Dansgaard, W. and S. J. Johnsen. 1969. A flow model and a time scale for the ice core from Camp Century, Greenland. *J. Glaciol.*, **8** (53), 215-223.

Dansgaard, W., S. J. Johnsen, H. B. Clausen, D. Dahl-Jensen, N. S. Gundestrup, C. U. Hammer, C. S. Hvidberg, J. P. Steffensen, A. E. Sveinbjörnsdottir, J. Jouzel and G. Bond. 1993. Evidence for general instability of past climate from a 250-kyr ice-core record. *Nature*, **364**, 218-220.

Denton, G. H. and T. J. Hughes, eds. 1981. *The last great ice sheets.* New York etc., Wiley and Sons.

Determann, J. 1991. Das Fließen von Schelfeisen – numerische Simulation mit der Methode der finiten Differenzen. *Ber. Polarforschung*, **83**.

De Wolde, J. R., P. Huybrechts, J. Oerlemans and R. S. W. van de Wal. 1997. Projections of global mean sea level rise calculated with a 2D energy-balance climate model and dynamic ice sheet models. *Tellus*, **49A**, 486-502.

Drewry, D. J. 1983. Antarctica: Glaciological and geophysical folio. Scott Polar Research Institute, University of Cambridge.

Durham, W. B. 1998. Factors affecting the rheologic properties of Martian polar ice. *First International Conference on Mars Polar Science and Exploration*, LPI Contribution No. 953, Lunar and Planetary Institute, Houston, 8-9.

Dzurisin, D. and K. R. Blasius. 1975. Topography of the polar layered deposits of Mars. *J. Geophys. Res.*, **80** (23), 3286-3306.

Edwards, R. L., J. H. Chen and G. J. Wasserburg. 1987a. ^{238}U-^{234}U-^{230}Th-^{232}Th systematics and the precise measurement of time over the past 500000 years. *Earth and Planetary Science Letters*, **81**, 175-192.

Edwards, R. L., J. H. Chen and G. J. Wasserburg. 1987b: Precise timing of the last interglacial from mass spectrometric determinations of thorium-230 in corals. *Science*, **236**, 1547-1553.

Edwards, R. L., H. Cheng, M. T. Murrell and S. J. Goldstein. 1997. Protactinium-231 dating of carbonates by thermal ionization mass spectrometry: implications for Quaternary climate change. *Science*, **276**, 782-786.

Eisenhauer, A., G. J. Wasserburg, J. H. Chen, G. Bonani, L. B. Collins, Z. R. Zhu and K.-H. Wyrwoll. 1993. Holocene sea-level determinations relative to the Australian continent: U/Th (TIMS) and ^{14}C (AMS) dating of coral cores from the Abrolhos. *Earth and Planetary Science Letters*, **114**, 529-547.

Eisenhauer, A., Z. R. Zhu, L. B. Collins, K.-H. Wyrwoll and R. Eichstaetter. 1996. The Last Interglacial sea level change: new evidence from the Abrolhos Islands, West Australia. *Geologische Rundschau*, **85**, 606-614.

ETOPO5. 1988. Data announcement 88-MGG-02, digital relief of the surface of the earth. NOAA, National Geophysical Data Center, Boulder, Colorado, USA.

Fabré, A., A. Letréguilly, C. Ritz and A. Mangeney. 1995. Greenland under changing climates: sensitivity experiments with a new three-dimensional ice sheet model. *Ann. Glaciol.*, **21**, 1-7.

Fanale, F. P., J. R. Salvail, W. B. Banerdt and R. S. Saunders. 1982. Mars: The regolith-atmosphere-cap system and climate change. *Icarus*, **50**, 381-407.

Fanale, F. P., S. E. Postawko, J. B. Pollack, M. H. Carr and R. O. Pepin. 1992. Mars: Epochal climate change and volatile history. In: *Mars*, ed. H. H. Kieffer *et al.*, The University of Arizona Press, 1135-1179.

Fastook, J. L. and J. E. Chapman. 1989. A map-plane finite-element model: three modeling experiments. *J. Glaciol.*, **35** (119), 48-52.

Forget, F. 1998. Mars CO_2 polar caps. In: *Solar System Ices*, ed. B. Schmitt *et al.*, Kluwer Academic Publishers, 477-507.

Fowler, A. C. 1984. On the transport of moisture in polythermal glaciers. *J. Geophys. Astrophys. Fluid Dyn.*, **28**, 99-140.

Fowler, A. C. 1992. Modelling ice sheet dynamics. *J. Geophys. Astrophys. Fluid Dyn.*, **63**, 29-65.

Fowler, A. C. and D. A. Larson. 1978. On the flow of polythermal glaciers. I. Model and preliminary analysis. *Proc. R. Soc. Lond.*, A **363**, 217-242.

Funk, M., K. Echelmeyer and A. Iken. 1994. Mechanisms of fast flow in Jacobshavns Isbræ, West Greenland: Part II. Modeling of englacial temperatures. *J. Glaciol.*, **40** (136), 569-585.

Funk, M. and H. Roethlisberger. 1989. Forceasting the effects of a planned reservoir which will partially flood the tongue of Unteraargletscher in Switzerland. *Ann. Glaciol.*, **13**, 76-81.

Gallup, D. C., R. L. Edwards and R. G. Johnson. 1994. The timing of high sea levels over the past 200000 years. *Science*, **263**, 769-800.

Gammelsrød, T. and N. Slotsvik. 1981. Hydrographic and Current Measurements in the Southern Weddell Sea 1979/80. *Polarforschung*, **51** (1), 101-111.

Glen, J. W. 1955. The creep of polycrystalline ice. *Proc. R. Soc. Lond.*, A **228** (1175), 519-538.

Giovinetto, M. B. and C. R. Bentley. 1985. Surface balance in ice drainage systems of Antarctica. *Antarct. J. U.S.*, **20** (4), 6-13.

Greve, R. 1995. Thermomechanisches Verhalten polythermer Eisschilde – Theorie, Analytik, Numerik. Ph. D. thesis, Institut für Mechanik, Technische Hochschule Darmstadt, Germany, 226 pp. [Available from Shaker Verlag (Series *Berichte aus der Geowissenschaft*), Aachen, Germany.]

Greve, R. 1997a. A continuum-mechanical formulation for shallow polythermal ice sheets. *Phil. Trans. R. Soc. Lond.*, A **355**, 921-974.

Greve, R. 1997b. Application of a polythermal three-dimensional ice sheet model to the Greenland Ice Sheet: Response to steady-state and transient climate scenarios. *J. Climate*, **10** (5), 901-918.

Greve, R. 1997c. Large-scale ice-sheet modelling as a means of dating deep ice cores in Greenland *J. Glaciol.*, **43** (144), 307-310; Erratum **43** (145), 597-600.

Greve, R. 1998. Dynamic/thermodynamic simulations of the north polar ice cap of Mars. *First International Conference on Mars Polar Science and Exploration*, LPI Contribution No. 953, Lunar and Planetary Institute, Houston, 13-15.

Greve, R. 2000a. On the response of the Greenland ice sheet to greenhouse climate change. *Climatic Change*, Special Issue on Climate Impact Response Functions (in press).

Greve, R. 2000b. Waxing and waning of the perennial north polar H_2O ice cap of Mars over obliquity cycles. *Icarus*, Mars Polar Science Special Issue (in press).

Greve, R. and K. Hutter. 1995. Polythermal three-dimensional modelling of the Greenland ice sheet with varied geothermal heat flux. *Ann. Glaciol.*, **21**, 8-12.

Greve, R. and D. R. MacAyeal. 1996. Dynamic/thermodynamic simulations of Laurentide ice sheet instability. *Ann. Glaciol.*, **23**, 328-335.

Greve, R., M. Weis and K. Hutter. 1998. Palaeoclimatic evolution and present conditions of the Greenland Ice Sheet in the vicinity of Summit: An approach by large-scale modelling. *Paleoclimates*, **2** (2-3), 133-161.

Greve, R., B. Mügge, D. Baral, O. Albrecht and A. Savvin. 1999a. Nested high-resolution modelling of the Greenland Summit region. *Advances in Cold-Region Thermal Engineering and Sciences* (ed. K. Hutter, Y. Wang and H. Beer), Springer, 285-306.

Greve, R., K.-H. Wyrwoll and A. Eisenhauer. 1999b. Deglaciation of the Northern Hemisphere at the onset of the Eemian and Holocene. *Ann. Glaciol.*, **28**, 1-8.

Grigoryan, S. S., M. S. Krass and P. A. Shumskiy. 1976. Mathematical model of a three-dimensional non-isothermal glacier. *J. Glaciol.*, **17** (77), 401-417.

Grosfeld, K. 1993. Untersuchungen zu Temperaturregime und Massenhaushalt des Filchner-Rønne-Schelfeises, Antarktis, unter besonderer Berücksichtigung von Anfrier- und Abschmelzprozessen. *Ber. Polarforschung*, **130**.

Haberle, R. M. and B. M. Jakosky 1990. Sublimation and transport of water from the north residual polar cap on Mars. *J. Geophys. Res.*, **95**, 1423-1437.

Hamelin, B., E. Bard, A. Zindler and R. G. Fairbanks. 1991. $^{234}U/^{238}U$ mass spectrometry of corals: How accurate is the U-Th age of the last interglacial period? *Earth and Planetary Science Letters*, **106**, 169-180.

Hammer, C. U., H. B. Clausen, W. Dansgaard, A. Neftel, P. Kristinsdottir and E. Johnson. 1985. Continuous impurity analysis along the Dye 3 deep core. In: C. C. Langway, H. Oeschger and W. Dansgaard (eds.), *Greenland Ice Core: Geophysics, Geochemistry and the Environment*, Geophysical Monographs No. 33, American Geophysical Union, Washington DC, 90-94.

Hansen, I. and R. Greve. 1996. Polythermal modelling of steady states of the Antarctic Ice Sheet in comparison with the real world. *Ann. Glaciol.*, **23**, 382-387.

Hansen, I., R. Greve and K. Hutter. 1996. Application of a polythermal ice sheet model to the Antarctic Ice Sheet: Steady-state solution and response to Milanković cycles. *Proceedings of the 5th International Symposium on Thermal Engineering and Science for Cold Regions*, 89-96.

Heinrich, H. 1988. Origin and consequences of cyclic ice rafting in the northeast Atlantic Ocean during the past 130000 years. *Quat. Res.*, **29**, 142-152.

Henderson, G. M., A. S. Cohen and R. K. O'Nions. 1993. $^{234}U/^{238}U$ ratios and ^{230}Th ages for the Haterum Atoll corals: Implications for coral diagenesis and seawater $^{234}U/^{238}U$ ratios. *Earth and Planetary Science Letters*, **115**, 65-73.

Herterich, K. 1987. On the flow within the transition zone between ice sheet and ice shelf. In: *Dynamics of the West Antarctic Ice Sheet*, ed. J. Oerlemans, D. Reidel Publishing Company, Terra Scientific Publishing Company; Dordrecht, Holland, 185-202.

Herterich, K. 1988. A three-dimensional model of the Antarctic ice sheet. *Ann. Glaciol.*, **11**, 32-35.

Herterich, K. 1990. Modellierung eiszeitlicher Klimaschwankungen. Habilitation thesis, Fachbereich Geowissenschaften, Universität Hamburg, Germany, 209 pp.

Hodge, S. M., D. L. Wright, J. A. Bradley, R. W. Jacobel, N. Skou and B. Vaughan. 1990. Determination of the surface and bed topography in Central Greenland. *J. Glaciol.*, **36** (122), 17-30.

Hofmann, W. 1974. Die Internationale Glaziologische Grönland-Expedition EGIG. *Z. Gletscherkd. Glazialgeol.*, **5**, 217-224.

Hooke, R. L. 1981. Flow law for polycrystalline ice in glaciers: comparison of theoretical predictions, laboratory data, and field measurements. *Rev. Geophys. Space Phys.*, **19** (4), 664-672.

Hourdin, F., P. Le Van, F. Forget and O. Talagrand. 1993. Meteorological variability and the annual surface pressure cycle on Mars. *J. Atmos. Sci.*, **50**, 3625-3640.

Hourdin, F., F. Forget and O. Talagrand. 1995. The sensitivity of the Martian surface pressure to various parameters: A comparison between numerical simulations and Viking observations. *J. Geophys. Res.*, **100**, 5501-5523.

Hutter, K. 1982. A mathematical model of polythermal glaciers and ice sheets. *J. Geophys. Astrophys. Fluid Dyn.*, **21**, 201-224.

Hutter, K. 1983. *Theoretical glaciology; material science of ice and the mechanics of glaciers and ice sheets.* D. Reidel Publishing Company, Dordrecht, Holland, 510 pp.

Hutter, K. 1993. Thermo-mechanically coupled ice sheet response. Cold, polythermal, temperate. *J. Glaciol.*, **39** (131), 65-86.

Hutter, K., H. Blatter and M. Funk. 1988. A model computation of moisture content in polythermal glaciers. *J. Geophys. Res.*, **93** (B10), 12205-12214.

Hutter, J. and F. M. Williams. 1980. Theory of floating ice sheets. In: *Physics and mechanics of ice*, ed. P. Tryde, IUTAM Symposium Copenhagen 1979, Springer-Verlag Berlin-Heidelberg-New York, 145-162.

Hutter, K., S. Yakowitz and F. Szidarovszky. 1986. A numerical study of plane ice sheet flow. *J. Glaciol.*, **32** (111), 139-164.

Huybrechts, P. 1992. The Antarctic ice sheet and environmental change: a three-dimensional modelling study. *Ber. Polarforschung*, **99**, 241 pp.

Huybrechts, P. 1993. Glaciological modelling of the Late Cenozoic East Antarctic ice sheet: stability or dynamism? *Geografiska Annaler*, **75 A** (4), 221-238.

Huybrechts, P. 1994. The present evolution of the Greenland ice sheet: an assessment by modelling. *Global Planet. Change*, **9**, 39-51.

Huybrechts, P. 1996. Basal temperature conditions of the Greenland ice sheet during the glacial cycles. *Ann. Glaciol.*, **23**, 226-236.

Huybrechts, P., A. Letréguilly and N. Reeh. 1991. The Greenland Ice Sheet and greenhouse warming. *Palaeogeogr., Palaeoclimatol., Palaeoecol. (Global Planet. Change Sect.)*, **89**, 399-412.

Huybrechts, P. and J. Oerlemans. 1988. Evolution of the East Antarctic ice sheet: A numerical study of thermo-mechanically response patterns with changing climate. *Ann. Glaciol.*, **11**, 52-59.

Huybrechts, P. and J. Oerlemans. 1990. Response of the Antarctic ice sheet to future greenhouse warming. *Climate Dynamics*, **5**, 79-92.

Huybrechts, P. and S. T'siobbel. 1995. Thermomechanical modelling of Northern Hemisphere ice sheets with a two-level mass-balance parameterization. *Ann. Glaciol.*, **21**, 111-116.

Imbrie, J., J. D. Hays, D. G. Martinson, A. McIntyre, A. C. Mix, J. J. Morley, N. G. Pisias, W. L. Prell and N. J. Shackleton. 1984. The orbital theory of Pleistocene climate: Support from a revised chronology of the marine δ^{18}O record. *Milankovitch and climate, part I*, A. Berger et. al. (eds.), D. Reidel Publishing Company, Dordrecht, Holland, 269-305 (NATO ASI Series C: Mathematical and Physical Sciences 126).

IPCC, 1996. *Climate Change 1995: The Science of Climate Change.* Cambridge University Press, Cambridge, UK, 572 pp.

Isaksson, E. and W. Karlén. 1994. Spatial and temporal patterns in snow accumulation, western Dronning Maud Land, Antarctica. *J. Glaciol.*, **40** (135), 399-409.

Isaksson, E., W. Karlén, N. Gundestrup, P. Mayewski, S. Whitlow and M. Twickler. 1996. A century of accumulation and temperature changes in Dronning Maud Land, Antarctica. *J. Geophys. Res.*, **101** (D3), 7085-7094.

Jaeger, L. 1976. Monatskarten des Niederschlags für die ganze Erde. *Ber. Deutsch. Wetterdienstes*, **139**, 38 pp.

Jakosky, B. M. and R. M. Haberle. 1992. The seasonal behavior of water on Mars. In: *Mars*, ed. H. H. Kieffer *et al.*, The University of Arizona Press, 969-1016.

Jakosky, B. M., B. G. Henderson and M. T. Mellon. 1993. The Mars water cycle at other epochs: Recent history of the polar caps and layered terrain. *Icarus*, **102**, 286-297.

Jenssen, D. 1977. A three-dimensional polar ice-sheet model. *J. Glaciol.*, **18** (80), 373-389.

Johnsen, S. J., H. B. Clausen, W. Dansgaard, K. Fuhrer, N. Gundestrup, C. U. Hammer, P. Iversen, J. Jouzel, B. Stauffer and J. P. Steffensen. 1992. Irregular glacial interstadials recorded in a new Greenland ice core. *Nature*, **359**, 311-313.

Johnsen, S. J., D. Dahl-Jensen, W. Dansgaard and N. Gundestrup. 1995. Greenland palaeotemperatures derived from GRIP borehole temperature and ice core isotope profiles. *Tellus*, **47B**, 624-629.

Jouzel, J. and 16 others. 1993. Extending the Vostok ice-core record of palaeoclimate to the penultimate glacial period. *Nature*, **364** (6436), 407-412.

Jouzel, J., K. Hammer, H. Miller, G. Orombelli, D. Peel and B. Stauffer. 1994. European project for ice coring in Antarctica. Science Plan. [Available from Laboratoire de Modélisation du Climat et de l'Environnement, CEA/DSM SE Saclay, F-91191 Gif sur Yvette Cedex, France.]

Jouzel, J. and 14 others. 1996. Climatic interpretation of the recently extended Vostok ice records. *Climate Dynamics*, **12**, 513-521.

Kapsner, W. R., R. B. Alley, C. A. Shuman, S. Anandakrishnan and P. M. Grootes. 1995. Dominant influence of atmospheric circulation on snow accumulation in Greenland over the past 18000 years. *Nature*, **373**, 52-54.

Kaufman, A. 1986. The distribution of $^{230}Th/^{234}U$ ages in corals and the number of Last Interglacial high sea stands. *Quarternary Research*, **25**, 55-62.

Kieffer, H. H. 1979. Mars south polar spring and summer temperatures: a residual CO_2 frost. *J. Geophys. Res.*, **84**, 8263-8288.

Kieffer, H. H. 1990. H_2O grain size and the amount of dust in Mars' residual north polar cap. *J. Geophys. Res.*, **95**, 1481-1493.

Kieffer, H. H. and A. P. Zent. 1992. Quasi-periodic climate change on Mars. In: *Mars*, ed. H. H. Kieffer *et al.*, The University of Arizona Press, 1180-1218.

Kieffer, H. H., S. C. Chase, T. Z. Martin, E. D. Miner and F. D. Palluconi. 1976. Martian north pole summer temperatures: Dirty water ice. *Science*, **194**, 1341-1344.

Kieffer, H. H., T. Z. Martin, A. R. Peterfreun, B. M. Jakosky, E. D. Miner and F. D. Palluconi. 1977. Thermal and albedo mapping during the Viking primary mission. *J. Geophys. Res.*, **78**, 4291-4312.

Kondratyev, K. Y. and G. E. Hunt. 1982. *Weather and climate on planets.* Pergamon Press.

Lee, W. H. K. 1970. On the global variations of terrestrial heat flow. *Phys. Earth Planet. Inter.*, **2** (5), 332-341.

LeMeur, E. and P. Huybrechts. 1996. A comparison of different ways of dealing with isostasy: examples from modelling the Antarctic ice sheet during the last glacial cycle. *Ann. Glaciol.*, **23**, 309-317.

Letréguilly, A., P. Huybrechts and N. Reeh. 1991a. Steady-state characteristics of the Greenland ice sheet under different climates. *J. Glaciol.* **37** (125), 149-157.

Letréguilly, A., N. Reeh and P. Huybrechts. 1991b. The Greenland ice sheet through the last glacial-interglacial cycle. *Palaeogeogr., Palaeoclimatol., Palaeoecol. (Global Planet. Change Sect.)*, **90**, 385-394.

Lliboutry, L. and P. Duval. 1985. Various isotropic and anisotropic ices found in glaciers and polar ice caps and their corresponding rheologies. *Ann. Geophys.*, **3** (2), 207-224.

MacAyeal, D. R. 1989. Large-scale ice flow over a viscous basal sediment: Theory and application to Ice Stream B, Antarctica. *J. Geophys. Res.*, **94** (B4), 4071-4087.

MacAyeal, D. R. 1992. Irregular oscillations of the West Antarctic ice sheet. *Nature*, **359**, 29-32.

MacAyeal, D. R. and R. H. Thomas. 1982. Numerical modeling of ice-shelf motion. *Ann. Glaciol.*, **3**, 189-194.

Mahaffy, M. W. 1976. A three-dimensional numerical model of ice sheets: Test on the Barnes ice cap, Northwest Territories. *J. Geophys. Res.*, **81** (6), 1059-1066.

Marsiat, I. 1994. Simulation of the northern hemisphere continental ice sheets over the last glacial-interglacial cycle: Experiments with a latitude-longitude vertically integrated ice sheet model coupled to a zonally averaged climate model. *Palaeoclimates*, **1**, 59-98.

Mayer, C. and P. Huybrechts. 1999. Ice-dynamic conditions across the grounding zone, Ekströmisen, East Antarctica. *J. Glaciol.*, **45** (150), 384-393.

Meese, D., R. Alley, T. Gow, P. M. Grootes, P. Mayewski, M. Ram, K. Taylor, E. Waddington and G. Zielinski. 1994. Preliminary depth-age scale of the GISP2 ice core. CRREL Special Report 94-1.

Morland, L. W. 1984. Thermo-mechanical balances of ice sheet flows. *J. Geophys. Astrophys. Fluid Dyn.*, **29**, 237-266.

Morland, L. W. 1987. Unconfined ice-shelf flow. In: *Dynamics of the West Antarctic Ice Sheet*, ed. J. Oerlemans, D. Reidel Publishing Company, Terra Scientific Publishing Company; Dordrecht, Holland, 99-116.

Morland, L. W. 1993. The flow of ice sheets and ice shelves. *Continuum mechanics in environmental sciences and geophysics*, K. Hutter (ed.), CISM courses and lectures, **337**, Springer Verlag, Wien etc., 403-466.

Morland, L. W. and I. R. Johnsen. 1980. Steady motion of ice sheets. *J. Glaciology*, **25**, 229-246.

Mügge, B. 1998. Eisalterbeerchnung im antarktischen Eisschild mit einem Algorithmus zur Teilchenverfolgung. Diploma thesis, Institut für Mechanik, Technische Universität Darmstadt, Germany.

Müller, I. 1973. *Thermodynamik*. Bertelsmann Universitätsverlag, Germany.

Müller, I. 1985. *Thermodynamics*. Pitman Advanced Publishing Program, Boston etc., 521 pp.

Mulvaney, R. and E. W. Wolff. 1994. Spatial variability of the major chemistry of the Antarctic ice sheet. *Ann. Glaciol.*, **20**, 440-447.

Neethling, D. C. 1970. Snow accumulation on the Fimbul Ice Shelf, western Dronning Maud Land, Antarctica. In: *International Symposium on Antarctic Glaciological Exploration*, A. J. Gow et al. (eds.), IASH Publ. **86**, 390-404.

Nye, J. F. 1957. The distribution of stress and velocity in glaciers and ice-sheets. *Proc. R. Soc. Lond.*, A **239**, 113-133.

Oerlemans, J. 1982. Response of the Antarctic Ice Sheet to a climatic warming: a model study. *J. Climatol.*, **2**, 1-11.

Ohmura, A. 1987. New temperature distribution maps for Greenland. *Z. Gletscherkd. Glazialgeol.*, **23**, 1-45.

Ohmura, A. and N. Reeh. 1991. New precipitation and accumulation maps for Greenland. *J. Glaciol.*, **37**, 140-148.

Ohmura, A., M. Wild and L. Bengtsson. 1996. Present and future mass balance of the ice sheets simulated with GCM. *Ann. Glaciol.*, **23**, 187-193.

Owen, T. 1992. The composition and early history of the atmosphere of Mars. In: *Mars*, ed. H. H. Kieffer *et al.*, The University of Arizona Press, 818-834.

Paige, D. A., K. E. Herkenhoff and B. C. Murray. 1990. Mariner 9 observations of the south polar cap of Mars: evidence for residual CO_2 frost. *J. Geophys. Res.*, **95**, 1319-1335.

Paterson, W. S. B. 1991. Why ice-age ice is sometimes "soft". *Cold Reg. Sci. Technol.*, **20**, 75-98.

Paterson, W. S. B. 1994. *The physics of glaciers*. Third edition. Oxford, etc., Pergamon Press, 480 pp.

Peltier, W. R. 1994. Ice age paleotopography. *Science*, **265**, 195-201.

Pelto, M. S. 1991. Relationship between tidewater glacier calving velocity and water depth at the calving front. *Ann. Glaciol.*, **15**, 115-118.

Picciotto, E., W. de Breuck and G. Crozaz. 1970. Snow accumulation along the South Pole – Dronning Maud Land traverse. In: *International Symposium on Antarctic Glaciological Exploration*, A. J. Gow et al. (eds.), IASH Publ. **86**, 18-22.

Pollack, J. B., R. M. Haberle, J. Schaeffer and H. Lee. 1990. Simulations of the general circulation of the Martian atmosphere. I. Polar processes. *J. Geophys. Res.*, **95**, 1447-1473.

Reeh, N. 1991. Parameterization of melt rate and surface temperature on the Greenland Ice Sheet. *Polarforschung*, **59** (3), 113-128.

Ritz, C. 1987. Time dependent boundary conditions for calculation of temperature fields in ice sheets. *The physical basis of ice sheet modelling*, E. D. Waddington and J. S. Walder (eds.), IAHS Publication **170**, 207-216.

Ritz, C. 1997. EISMINT intercomparison experiment. Comparison of existing Greenland models. Unpublished manuscript, Laboratoire de Glaciologie et de Géophysique de l'Environnement, Saint Martin d'Hères, France. [Available online from ftp anonymous glaciog.ujf-grenoble.fr, directory /pub/EISMINT-INTERCOMP/GREENLAND.]

Ritz, C., A. Fabré and A. Letréguilly. 1996. Can an ice sheet model simulate the present Greenland ice sheet? Consequences on the evolution through the last

climatic cycle. Preprint, Laboratoire de Glaciologie et Géophysique de l'Environnement, CNRS, Saint Martin d'Hères Cedex, France.

Robin, G. de Q. 1975. Ice shelves and ice flow. *Nature*, **253**, 168-173.

Savvin, A. 1999. Grenzschichttheorie nichtlinearer Kriechströmungen und ihre Anwendung auf das EPICA-Vorhaben. Ph. D. thesis, Institut für Mechanik, Technische Universität Darmstadt, Germany.

Savvin, A., R. Greve, R. Calov, B. Mügge and K. Hutter. 2000. Simulation of the Antarctic ice sheet with a 3-d polythermal ice-sheet model, in support of the EPICA project. Part II: Nested high-resolution treatment of Dronning Maud Land. *Ann. Glaciol.*, **30** (in press).

Schönwiese, C.-D. 1992. *Klima im Wandel. Tatsachen, Irrtümer, Risiken.* Deutsche Verlags-Anstalt, Stuttgart, Germany, 223 pp.

Schubert, G., S. C. Solomon, D. L. Turcotte, M. J. Drake and N. H. Sleep. 1992. Origin and thermal evolution of Mars. In: *Mars*, ed. H. H. Kieffer *et al.*, The University of Arizona Press, 147-183.

Shumskiy, P. A. and M. S. Krass. 1976. Mathematical models of ice shelves. *J. Glaciol.*, **17** (77), 419-432.

Sowers, T., M. Bender, L. Labeyrie, D. Martinson, J. Jouzel, D. Raynaud, J. J. Pichon and Y. Korotkevich. 1993. 135,000 year Vostok-SPECMAP common temporal framework. *Paleoceanography*, **8**, 737-766.

Stirling, C. H., T. M. Esat, M. T. McCulloch and K. Lambeck. 1995. High-precision U-series dating of corals from western Australia and implications for the timing and duration of the Last Interglacial. *Earth and Planetary Science Letters*, **135**, 115-130.

Svendsen, B. and K. Hutter. 1996. A continuum approach for modelling induced anisotropy in glaciers and ice sheets. *Ann. Glaciol.*, **23**, 262-269.

Szabo, B., K. R. Ludwig D. R. Muhs and K. R. Simmons. 1994. Thorium-230 ages of corals and duration of the last interglacial sea-level high stand on Oahu. *Science*, **266**, 93-96.

Thomas, P., S. Squyres, K. Herkenhoff, A. Howard and B. Murray. 1992. Polar deposits of Mars. In: *Mars*, ed. H. H. Kieffer *et al.*, The University of Arizona Press, 767-795.

Thomas, R. H. 1973. The creep of ice shelves. *J. Glaciol.*, **12**, 167-178.

Thomas, R. H. 1979. The dynamics of marine ice sheets. *J. Glaciol.*, **24** (90), 167-177.

Thorsteinsson, T. 1996. Textures and fabrics in the GRIP ice core, in relation to climate history and ice deformation. *Ber. Polarforschung*, **205**, 146 pp.

Van der Veen, C. J. 1996. Tidewater calving. *J. Glaciol.*, **42** (141), 375-385.

Van der Veen, C. J. (ed.) 1997. Calving glaciers – Report of a workshop, February 28 – March 2, 1997, Byrd Polar Research Center, The Ohio State University, Columbus, Ohio. *BRPC Report*, **15**.

Van de Wal, R. S. W. and J. Oerlemans. 1997. Modelling the short-term response of the Greenland ice sheet to global warming. *Climate Dynamics*, **13**, 733-744.

Ward, W. R. 1979. Present obliquity oscillations of Mars: Fourth-order accuracy in orbital e and I. *J. Geophys. Res.*, **84**, 237-241.

Weertman, J. 1957. Deformation of floating ice shelves. *J. Glaciol.*, **24** (21), 38-42.

Weis, M., R. Greve and K. Hutter. 1999. Theory of shallow ice shelves. *Cont. Mech. Thermodyn.*, **11**, 15-50.

Weis, M., K. Hutter and R. Calov. 1996. 250.000 years in history of the Greenland Ice Sheet. *Ann. Glaciol.*, **23**, 359-363.

Wilhelms, F. 1996. Leitfähigkeits- und Dichtemessung an Eisbohrkernen. *Ber. Polarforschung*, **191**, 224 pp.

Williams, F. M. and K. Hutter. 1983. Thermal response of unconfined ice shelves to climatic conditions. *Acta Mechanica*, **48**, 131-146.

Winograd, I. J., B. Coplen, J. M. Landwehr, A. C. Riggs, K. R. Ludwig, B. J. Szabo, P. T. Kolesar and K. M. Revesz. 1992. Continuous 500000 year climate record from vein calcite in Devil's Hole, Nevada. *Science*, **258**, 255-260.

Wu, T. 1996. Schwerkraftgetriebene Scherströmungen in gesättigten Binärmischungen nicht-Newtonscher Fluide mit Anwendungen auf das Fließen von sedimentverschmutztem Eis. Ph. D. thesis, Institut für Mechanik, Technische Hochschule Darmstadt, Germany, 142 pp. [Available from Shaker Verlag (Series *Berichte aus der Geowissenschaft*), Aachen, Germany.]

Wyrwoll K.-H., Z. R. Zhu, G. Kendrick, L. Collins and A. Eisenhauer. 1995. Holocene sea-level events in Western Australia: revisiting old questions. *Journal of Coastal Research*, Special Issue No. 17: *Holocene Cycles, Climate, Sea Levels and Sedimentation*, 321-326.

Zhu, Z. R., K.-H. Wyrwoll, L. B. Collins, J. H. Chen, G. J. Wasserburg and A. Eisenhauer. 1993. High-precision U-series dating of Last Interglacial events by mass spectrometry: Houtman Abrolhos, western Australia. *Earth and Planetary Science Letters*, **118**, 281-293.

Zuber, M. T., D. E. Smith, S. C. Solomon, J. B. Abshire, R. S. Afzal, O. Aharonson, K. Fishbaugh, P. G. Ford, H. V. Frey, J. B. Garvin, J. W. Head, A. B. Ivanov, C. L. Johnson, D. O. Muhleman, G. A. Neumann, G. H. Pettengill, R. J. Phillips, X. Sun, H. J. Zwally, W. B. Banerdt and T. C. Duxbury. 1998. Observations of the north polar region of Mars from the Mars Orbiter Laser Altimeter. *Science*, **282**, 2053-2060.